The SAXS Guide

Getting acquainted with the principles

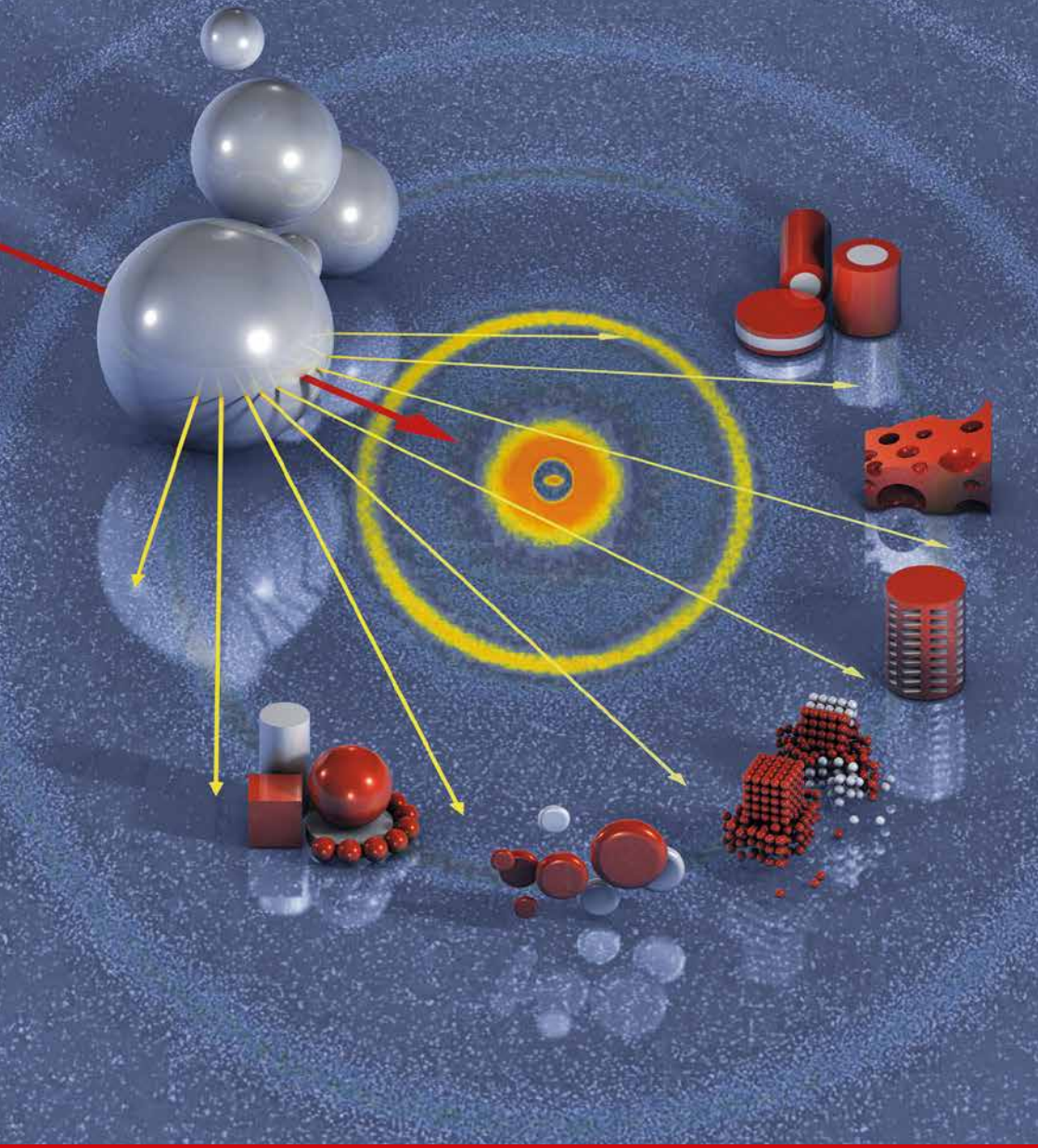

5th Edition

The SAXS Guide

Getting acquainted with the principles

5th edition

by
Heimo Schnablegger
Yashveer Singh

Special contributions on

"SAXS Structural Biology" by Jill Trewhella, The University of Sydney, and Tobias Madl, Medical University of Graz

and

"GISAXS – Grazing-Incidence Small-Angle Scattering" by Detlef-M. Smilgies, Cornell High Energy Synchrotron Source (CHESS)

and

"USAXS – Ultra-Small-Angle X-Ray Scattering" by Jan Ilavsky, Argonne National Laboratory, and Fan Zhang, National Institute of Standards and Technology

➤ Published by Anton Paar GmbH. Printed in Austria.

Anton Paar GmbH
Anton-Paar-Straße 20
A-8054 Graz
Austria - Europe
Tel.: +43 316 257-0
Fax: +43 316 257-257
E-Mail: info@anton-paar.com
Web: www.anton-paar.com

Date: March 2023

Specifications subject to change without notice. | 03/22 D21IP004EN-C

Contents

1. Introduction

This document gives a general introduction to Small-Angle X-Ray Scattering (SAXS) and SAXS analysis. It explains how a SAXS instrument works and how SAXS analysis is done. It is intended to help people new to the field of SAXS analysis. Difficult mathematical equations are avoided, and the document requires only basic knowledge of mathematics, physics and colloid chemistry. The advanced reader is also encouraged to look for details in the original literature,[1]-[7] which can be found in the references section (see „Literature“ on page 164).

This document is not dedicated to one specific scattering instrument or one particular application area but aims to give a global overview of the main instrumentation and applications.

2. What is SAXS

SAXS is an analytical method to determine the structure of particle systems in terms of averaged particle sizes or shapes. The materials can be solid or liquid and they can contain solid, liquid or gaseous domains (so-called particles) of the same or another material in any combination. Normally, X-rays are sent through the sample (transmission mode) and every particle that happens to be inside the beam will send out its signal. Thus, the average structure of all illuminated particles in the bulk material is measured.

But also surface-near particles can be measured selectively, when the X-rays hit a flat sample almost parallel to its surface and the scattering signal is measured in reflection mode. This discipline of SAXS is called GISAXS (GI = grazing incidence) and it measures the average structure of all illuminated particles and their relative positional order on the surface or within the surface layer.

The SAXS method is accurate, non-destructive and usually requires only a minimum of sample preparation. Application areas are very broad and include biological materials, polymers, colloids, chemicals, nanocomposites, metals, minerals, food and parmaceuticals and can be found in research as well as in quality control.

The samples that can be analyzed and the time requirements of the experiments mainly depend on the used instrumentation, which can be classified into two main groups: (1) the line collimation instruments and (2) the point collimation instruments, which are explained in more detail later. The particle or structure sizes that can be resolved range from approximately 1 nm to 300 nm in a typical setup but can be extended on both sides by measuring at smaller (Ultra-Small-Angle X-Ray Scattering, USAXS) or larger angles (Wide-Angle X-Ray Scattering, WAXS also called X-Ray Diffraction, XRD) than the typical 0.1° to 10° of SAXS. The concentration ranges between 0.1 wt.% and 99.9 wt.%. Generally speaking, particles made of materials with high atomic numbers show higher contrast and have lower detection limits when measured in matrix

materials of lighter elements. Matrix materials of heavy elements should be avoided due to their high absorption of X-rays.

Standards are required in SAXS only when the **sample-to-detector distance** is not known. Then a reference sample of known structure is measured in order to calibrate the scattering angles. This is required only for instruments that employ unreliable mechanical movements and have poorly documented detector or sample positions.

Fig. 1 shows a typical pair of scattering profiles of a dispersion of particles and of the solvent alone. The difference between these two profiles is the actual signal and is put into calculations in order to obtain the information of size, shape, inner structure or the specific surface of the particles.

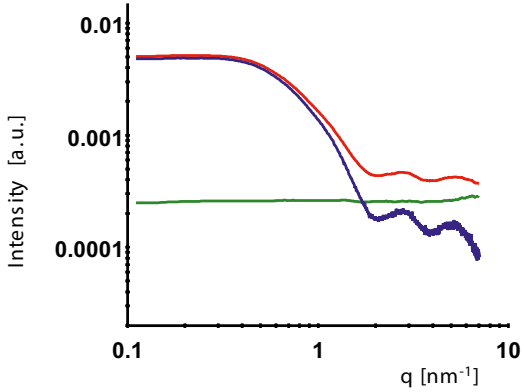

Fig. 1
Typical SAXS profiles of (red) a particle dispersion, (green) of the solvent and (blue) the difference profile therefrom.

➤ 2.1. Scattering and microscopy

Scattering and absorption are the first processes in any technique that uses radiation, such as an optical microscope (see Fig. 2). This means that interaction between matter and the incoming radiation must take place. Otherwise no picture of the investigated object (= particle) will be available. Neither with microscopy nor with scattering can an object be investigated when there is no contrast. In order to establish contrast in SAXS, the particles must have an electron density different than that of the surrounding matrix material (e.g., the solvent).

Although the operation of a scattering instrument is identical to the first process that takes place in a microscope, its result is complementary to that of a microscope, as will be outlined below.

The second process in an optical microscope is the reconstruction of the object (particle) from the scattering pattern (see Fig. 2). This is done with the help of a lens system. If a lens system is not readily available for the used radiation (such as X-rays), then a reconstruction is not directly possible. Instead, the scattering pattern must be recorded and the reconstruction must be attempted in a mathematical way rather than in an optical way.

In the recording process the phases of the detected waves are lost. This constitutes the main difference between microscopy and X-ray scattering. Because of the lost phases, it is not possible to achieve a 3D (holographic) representation of the object in a direct way, as it would be possible with a lens system.

In microscopy one object or a small part of a sample is magnified and investigated. With scattering techniques the whole illuminated sample volume is investigated. As a consequence, average values of the structure parameters are obtained by SAXS. The average is taken over all objects and over all orientations of the objects. Therefore, structure details of the object will not become visible unless they are pronounced enough in the whole sample and are therefore representative.

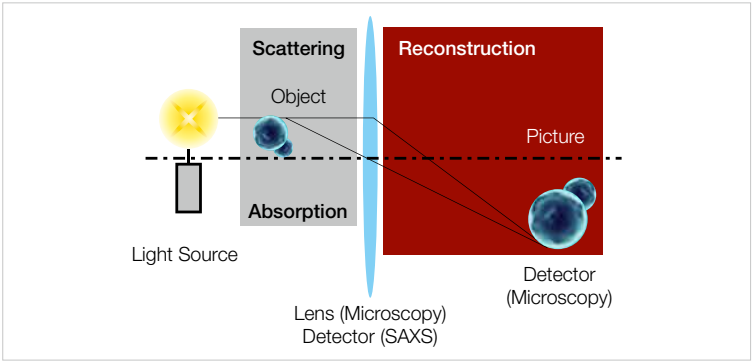

Fig. 2
The first processes of a microscopic investigation are scattering and absorption. Microscopy: The scattered waves are processed into a picture (reconstructed) by a lens. SAXS: The scattered intensity is recorded by a detector and is processed mathematically, as a replacement for the actions of a lens.

The signal strength in SAXS scales with the squared volume of the particle. This means that small particles are hardly visible in the presence of big particles. On the other hand, SAXS is very sensitive to the formation or growth of large particles.

The resolution criteria in SAXS are the same as those in microscopy. The closer the lens to the object (the larger the aperture or the scattering angle), the smaller is the detail that can be resolved. The farther away the object is from the lens (the smaller the aperture or the scattering angle), the bigger is the largest object that can be brought into the picture.

The following table summarizes a typical comparison of the two techniques.

Table 1
Comparison of microscopy and scattering.

Feature	Microscopy	Scattering
Small details are	visible	not visible
Results are	unique but not representative	representative but ambiguous
Local structure details	can be extracted	cannot be extracted
Average structures are	hard to obtain	always obtained
Preparation artifacts are	inherent	scarce (in vitro experiments)

In order to get the complete picture of an unknown sample one needs to make use of both methods because **their results are complementary.**

3. Basics of SAXS

When X-rays irradiate a sample, then

1. The atoms inside the sample will scatter the incident radiation into all directions, which gives a background radiation that is almost constant at small angles.

2. The particles (i.e., clusters of atoms) inside the sample will produce additional scattering (so-called excess scattering) which is due to the fact that the particles are made of a different material or density (to give contrast) and are in the size-range of the X-ray wavelength.

By measuring the angle-dependent distribution of the scattered radiation (intensity) it is possible to draw conclusions about the average particle structure.

➤ 3.1. What are X-rays

X-rays are electro-magnetic waves just like “ordinary” visible light. But the wavelength is much shorter (<0.3 nm) than that of visible light (~500 nm). The waves propagate because an alternating electric field ($\vec{E}$) causes an alternating magnetic field ($\vec{H}$) and vice versa (see Fig. 3). The electric field, the magnetic field and the direction of propagation are always at right angles with respect to each other.

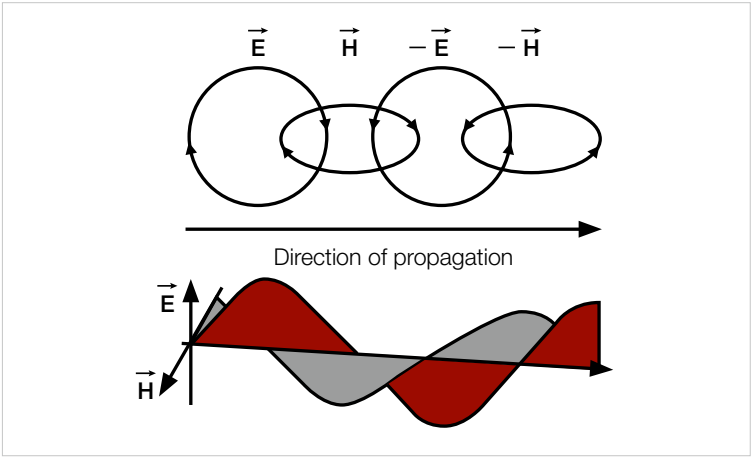

Fig. 3
Electro-magnetic waves propagate due to induction processes. Close to the light source, the electric and the magnetic fields are phase shifted as shown here. Far away from the source, however, the two fields oscillate in phase.

Sometimes X-rays are described by particles called photons. Therefore, every interaction between light and matter can be described by two models, the oscillator model (wave) and the impulse-transfer model (photon).

➤ 3.2. Interaction of X-rays with matter

There are two main interactions of X-rays with matter: absorption and scattering. If X-rays hit a material, a fraction will pass through the sample, a fraction will be absorbed and transformed into other forms of energy (heat, fluorescence radiation, etc.) and a fraction will be scattered into other directions of propagation.

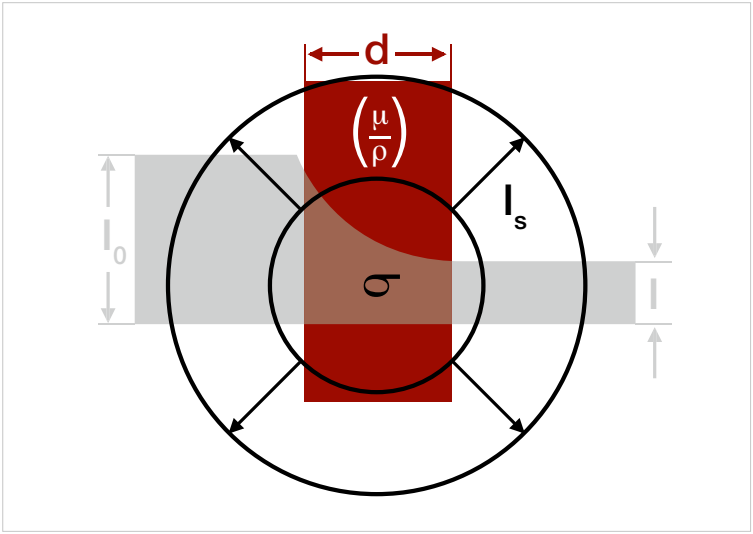

Fig. 4
Incoming X-rays of intensity I_0 are attenuated to an intensity I and partly converted into scattered X-rays of intensity IS by a material of thickness d, density (ρ), mass-absorption coefficient $(\frac{\mu}{\rho})$ and scattering cross-section (σ).

3.2.1 Absorption

Irradiation of an atom with X-ray photons can expel an electron from the atom. By doing so the X-ray energy is used up and the photon is absorbed. This leaves the atom in an unstable situation with a hole where there was an electron before. The atom wants to restore the original configuration, and this is done by rearranging the remaining electrons in order to fill up the hole. As a result of this, the atom emits fluorescence radiation, i.e., X-rays with other wavelengths than the incident radiation.

The absorption of an X-ray photon is most efficient at the so-called absorption edges, where the electrons of the material have the highest probability to be expelled. Absorption basically occurs at all wavelengths with various efficiencies. Depending on the atomic species of the material and on the wavelength, these absorption efficiencies are tabulated[8] as so-called mass-absorption

coefficients $(\frac{\mu}{\rho})$, where μ is the linear absorption coefficient and ρ is the density of the material.

In order to obtain high-quality SAXS data the absorption must be kept small. The optimum sample thickness d_{opt} depends on the linear absorption coefficient,

Equation 1

$$d_{opt} = \frac{1}{\mu}$$

Typical values for d_{opt} at commonly used wavelengths are summarized in Table 2:

Table 2
The optimum sample thickness d_{opt} in [µm] of various matrix materials at commonly used X-ray wavelengths.

Radiation Wavelength	Cr-K_α 0.2291 nm	Cu-K_α 0.1542 nm	Mo-K_α 0.07107 nm	Density [g/mL]
Water, 4 °C	301.6	980.8	9886	1.0
Quartz glass	41.0	126.6	1351	2.203
Chloroform, 15 °C	23.9	70.5	718	1.498
Iron metal	11.4	4.22	36.8	7.86
Tungsten metal	1.15	3.08	5.70	19.3

3.2.2 Scattering

Scattering can occur with or without loss of energy. This means that the scattered radiation can have a different wavelength than the incident radiation, such as in Compton scattering[9] (inelastic scattering), or it can have the same wavelength, such as in Rayleigh or Thomson scattering[10] (elastic scattering).

Compton scattering is produced when a photon hits an electron and is bounced away. The photon loses a fraction of its energy, which is taken over by the electron. The process can be compared with one billiard ball colliding with another. The scattered radiation has a different wavelength and has no particular phase relationship (incoherent scattering) with the incident radiation. It cannot produce interference phenomena and therefore does not carry structure information. It is part of the featureless background radiation.

Rayleigh and Thomson scattering* happens when photons collide with strongly bound electrons without energy transfer. The electrons start oscillating at the same frequency as the incoming radiation. Due to this oscillation, the electrons emit radiation with the same frequency. Because the emitted waves of neighboring atoms oscillate strictly synchronous to each other, they produce "coherent waves" (coherent scattering) which have the capability to interfere at the detector. These interference patterns carry the information about the particle structure (see „Interaction of X-rays with structure" on page 18).

The efficiency by which X-rays are scattered depends on the amount of electrons per illuminated material volume. Every illuminated electron contributes the same amount of scattered radiation, which is expressed by the so-called "scattering cross-section," $\sigma = 7.93977 \cdot 10^{-26}$ cm^2 or the Thomson factor. It is the scattered energy produced by an incident beam of unit energy per unit area. Atomic scattering cross sections can be found in tables.[11]

➤ 3.3. Detection of X-rays

X-rays are detected by methods using an absorption process in the first step. Solid-state detectors, gas-filled detectors and scintillation detectors all use the fact that free electrons are produced due to the impact of an X-ray photon, which will be absorbed in this impact. Acceleration, multiplication and amplification processes then lead to electric pulses that are counted and put out as "the intensity" or as "the count rate." Also, imaging plates absorb X-rays and accumulate their energy by excited electrons, the number of which is proportional to the number of photons that hit the imaging plate. Illumination by visible light then makes the excited electrons relax and emit visible fluorescence radiation which is measured with photo-multiplier tubes that are sensitive to visible light.

* **Rayleigh scattering** is used when the incident radiation is visible light, and **Thomson scattering** is used in the case of X-rays and neutrons.

Whatever the type of detector, only the intensity is accessible, i.e., only the squared amplitude of the wave, $I_s = |\vec{E}_s|^2$, and not the amplitude by itself, can be measured. Therefore, valuable information about the sign (or the phase) of the electric field is lost. A holographic reconstruction of a three-dimensional structure from recorded intensities becomes practically impossible. Thus, the result of a structure analysis by scattering will always be ambiguous and the data must be interpreted with some knowledge about the sample (e.g., from microscopy or from an understanding of the sample's chemistry).

➤ 3.4. Interaction of X-rays with structure

When X-rays are scattered at atoms, every atom emits spherical waves emanating from the position of the respective atom. Because the outgoing light waves from Thomson-scattering processes are synchronized with the incoming plane waves, they produce interference patterns at the detector's position. The interferences can be constructive (in phase), destructive (out of phase) or somewhere in-between depending on the observation angle 2θ, the orientation and the distance r of the light-emitting atoms from each other.

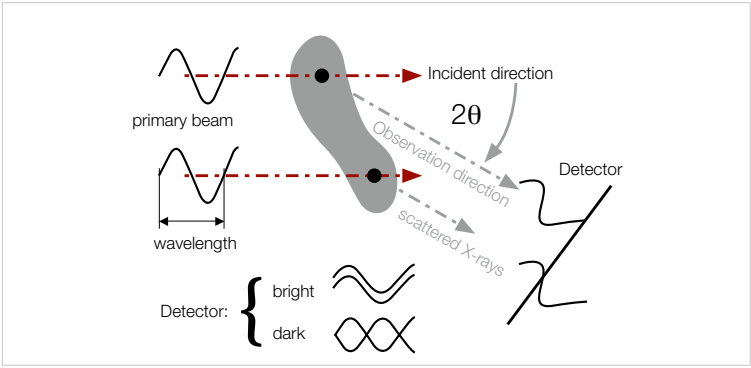

Fig. 5
The intensity of interfering waves depends on the distance of the emitting atoms and on their orientations with respect to the directions of incidence and observation. When the waves arrive in phase, the detector receives brightness and when the waves arrive out of phase, then the detector receives darkness.

In a constructive constellation the interference causes a bright spot at the detector and in a destructive constellation the waves extinguish each other, thus producing a dark spot at the detector. The result is a 2D interference pattern, where the intensity varies from position to position in the detection plane (usually measured in terms of scattering angle 2θ and azimuth angle ϕ). The interference pattern is characteristic to the internal structure of the material, i.e., to the orientation and distances of the atoms relative to each other.

Every distance is measured relative to the wavelength λ of the applied radiation. An identical interference pattern is therefore produced whenever the ratio r/λ is identical. In an attempt to become independent from the wavelength, scattering patterns are usually presented[2] as functions of q,

$$q = \frac{4\pi}{\lambda} \cdot \sin\left(\frac{2\theta}{2}\right)$$

Equation 2

Names for q, which can be found in literature, are “length of the scattering vector” or “momentum transfer.”* Whatever the name, fact is that the dimension of q is one over length (e.g., [1/nm]) and this explains that a scattering pattern is usually called “the structure in reciprocal space,” whereas the particles are said to have a “structure in real space” because they can be measured in units of length (e.g., [nm]).

* Some authors prefer to use $s = \frac{q}{2\pi}$ instead of q because of its convenient application in crystallography. Its reciprocal value directly gives the distance between crystalline lattice planes.

➤ 3.5. The form factor

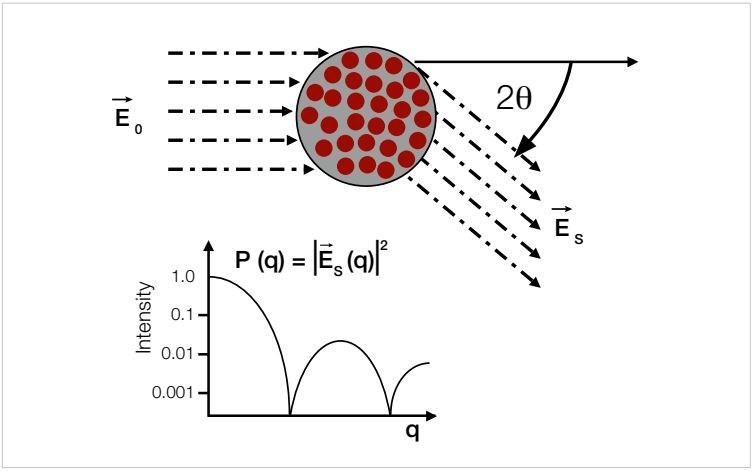

Fig. 6
The form factor, P(q), of a particle is an interference pattern, the oscillations of which are typical of the particle's shape.

The scattering of one particle, which is made of many atoms, can be explained as the interference pattern produced by all the waves that are sent to the detector from every electron/atom inside the particle (see Fig. 6). Summing up all the wave amplitudes at the detector position and making the square of this sum results in an interference (scattering) pattern. This pattern oscillates in a fashion that is characteristic for the shape (or the form) of the particle. It is therefore called the form factor *P(q)*. It is a "factor" because it must be scaled with a constant in order to match the experimental intensity units. For structure determination the scaling factor is not required.

In practical applications many particles are illuminated at the same time and the observed scattering pattern corresponds to the form factor of one particle only

1. if the particles are all identical in shape and size (i.e., monodisperse sample) and

2. if the particles are far away from each other (i.e., dilute sample).

If the sample is dilute, then the form factors of all illuminated particles can be summed up. In a dilute sample the experimental scattering pattern is the form factor multiplied by the number of particles that are in the X-ray beam.

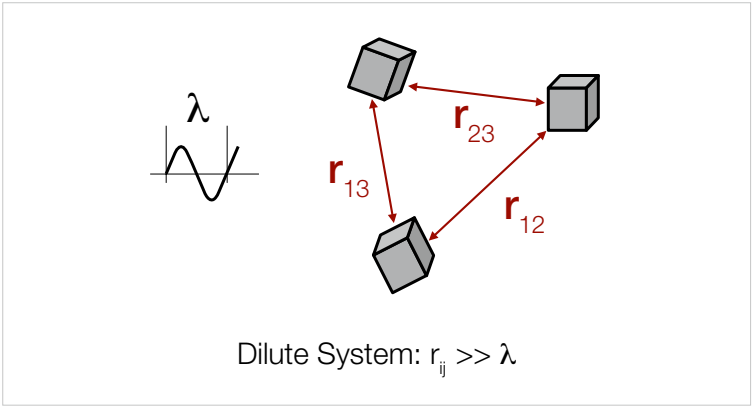

Fig. 7
A dilute system of particles is defined for SAXS when the distances between the particles are large in comparison to the wavelength λ.

If the particles have different sizes (e.g., polydisperse samples), then the form factors of all particle sizes are summed up to obtain the average scattering pattern of the whole sample. Because every size produces form factors with their minima at different angles, the sum of all form factors will no longer contain well-determined minima. We discuss this in more detail in 3.9 “Polydispersity” below.

➤ 3.6. The structure factor

When particle systems are densely packed (i.e., concentrated samples), the distances relative to each other come into the same order of magnitude as the distances inside the particles. The interference pattern will therefore contain contributions from neighboring particles as well.

This additional interference pattern multiplies with the form factor of the single particle and is called the structure factor *S(q)*. In crystallography it is known as “the lattice factor” because it contains the information about the positions of the particles with respect to each other. Concentration effects become visible at small angles

by the formation of an additional wave (see Fig. 8). The descent in intensity at small q-values is typical for repulsive interaction potentials. An intensity increase indicates attractive interaction, which is very similar to aggregation.

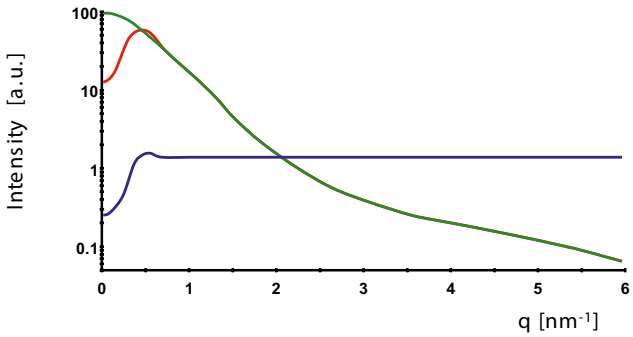

Fig. 8
The SAXS profile of (red) a concentrated particle dispersion is the product of (green) the form factor of the single particle with (blue) the structure factor of the particle positions.

Eventually this wave can develop into a pronounced peak when the particles align themselves into a highly ordered and periodic (i.e., crystalline) arrangement. It is then called a Bragg peak and the position of its maximum (q_{Peak}) indicates the distance (d_{Bragg}) between the aligned particles by using Bragg's law:

Equation 3

$$d_{Bragg} = \frac{2\pi}{q_{Peak}}$$

➤ 3.7. Orientation and order

In a densely packed particle system the positions and orientations of its particles can align themselves with respect to each other. This is usually summarized by the expression “interaction.” For example, the molecules of a liquid cannot move freely because they cannot penetrate each other. The particle-particle repulsion (among other inter-particle forces) leads to a so-called short-range order. This means that there is an increased probability to find a next-neighbor particle at a specific distance. At larger distances, however, the relative positions become more and more random to each other. The result of this short-range order is the build-up of a structure factor in the SAXS pattern.

The peaks in the structure factor become more and more pronounced when the particle positions become increasingly ordered. When the domain size of ordered particles increases (i.e., formation of long-range order), the system is said to crystallize. The structure factor of a crystalline substance is normally called lattice factor. It is a set of narrow and intensive peaks at well-defined angles indicative for the crystal symmetry. It can be shown that the ratios of the peak positions on the q-scale have typical values, which reveal the crystal symmetry. For example:

1. Lamellar symmetry: 1, 2, 3, 4, 5, ...
2. Cubic symmetry: 1, $\sqrt{2}$, $\sqrt{3}$, 2, $\sqrt{5}$, ...
3. Hexagonal symmetry: 1, $\sqrt{3}$, 2, $\sqrt{7}$, 3, ...

In addition to this positional order, the particles can also develop a preferential orientation with respect to each other, especially when the particle shapes are not spherical. The alignment of particle orientations is only partial in sheared or stretched samples, but it is perfect in crystalline samples.

Orientation and its degree can be observed in a 2D scattering pattern by the amplitude of intensity modulation, when measured in a circle around the primary beam. When the sample is randomly

oriented (isotropic), such as dilute dispersions or crystal powders, the scattering pattern has equal intensities along concentric circles around the incident beam (see Fig. 9). It shows intensity modulations when the sample is partially oriented, such as in sheared liquids or spun fibers. When the sample is a single crystal in a specific orientation with respect to the incident beam, then this is signalized by intensive spots (reflections).

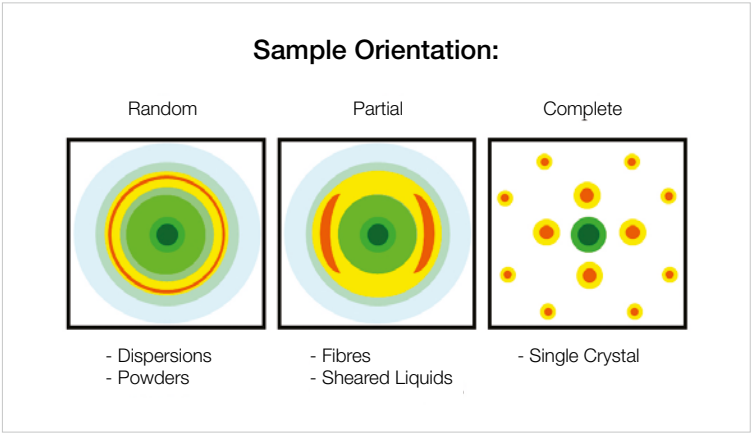

Fig. 9
The 2D scattering patterns of randomly oriented (isotropic), partially oriented and perfectly oriented (single crystal) samples.

➤ 3.8. Intensity and contrast

In order to compare theoretical with experimental scattering curves, one can scale the theoretical ones (form factor and structure factor) by arbitrary constant numbers. These scaling factors contain no information about the shape of the particles and, thus, can be chosen arbitrarily. Occasionally, however, they gain a certain interest, when particle number densities or molecular weights of particles have to be determined, as discussed later (see „Molecular weight“ on page 68).

X-rays are scattered by electrons. The scattered intensity of one electron (the “scattering cross-section”) is a constant,
$\sigma = 7.93977 \cdot 10^{-26}$ cm^2 . It is the scattered energy that is produced by an incident beam of unit energy per cm^2. If it is illuminated by a beam

of energy density I_0 [a.u. / cm^2], then the resulting scattered intensity is $I_0 = I_0 \cdot \sigma$ [a.u.], where "a.u." means arbitrary detector units. It can be "counts per second," Joule or even Watt, depending on the read-out capabilities of the detection device. The intensity arriving at the detector is modified, however, by the sample transmittance T, the sample-detector distance R, the size of the detection area (pixel size) A and by the polarization angle φ of the incident waves relative to the plane of observation (see Fig. 10).

$$I = I_0 \cdot \sigma \cdot \frac{A}{R^2} \cdot T \cdot [(\sin\varphi)^2 + (\cos\varphi)^2 \cdot \cos(2\theta)^2] \qquad \textit{Equation 4}$$

X-rays of standard laboratory sources are randomly polarized, which amounts to $\varphi = 45°$ (averaged polarization). At synchrotrons the polarization angle can have any value between $\varphi = 0°$ (horizontal polarization) and $\varphi = 90°$ (vertical polarization). In SAXS experiments, i.e., for ($2\theta < 10°$), the polarization term is usually ignored but not in XRD experiments.

The more electrons are placed in a sample volume (i.e., the higher the electron density), the more waves are scattered. If the sample is just one particle of volume V_1 with an electron density of ρ_1, then $V_1\rho_1$ wave amplitudes are scattered. The detector read-out (i.e., the intensity) is the square of all wave amplitudes that come from this volume. The total scattered intensity of this particle $I_{1\,(q)}$ then amounts to

$$I_1(q) = I_0 \cdot \rho_1^2 \cdot V_1^2 \cdot P(q) \qquad \textit{Equation 5}$$

where *P(q)* is the form factor of the particle.

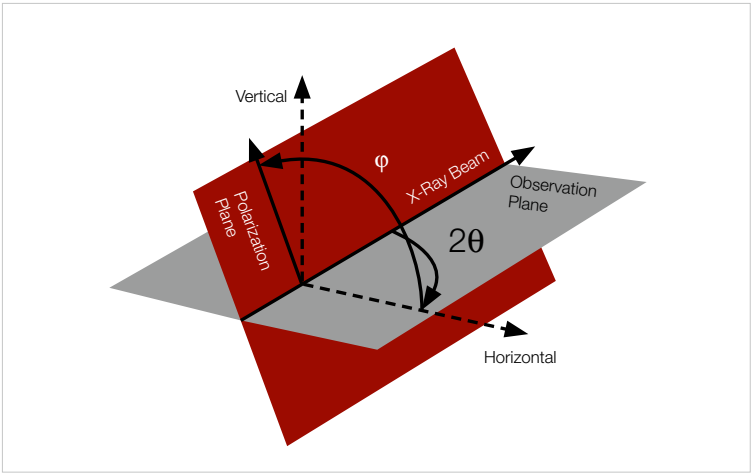

Fig. 10
The polarization angle φ defines the angle between the plane in which the radiation wave oscillates (i.e., the polarization plane) and the plane in which the scattering angle 2θ is measured.

Only the interfering photons carry information on the structure. The scattering of the matrix material also carries information but on a much smaller (atomic) length scale. It just causes a flat radiation level (background) in the SAXS region. In practice, one subtracts the blank scattering (of sample holder and matrix) from the sample scattering.

Particles embedded in a matrix must have an electron density different to the matrix in order to become visible in SAXS. The visibility increases with the difference in electron density between the two materials. This is called contrast. If the particles' electron density were the same as the one of the matrix (see Fig. 11), then the particles could not be distinguished from their environment and the SAXS signal would be just the same as that of the background.
Measures to exploit the effects of contrast are called "contrast variation." By changing the solvent's electron density, some particle components can be made invisible. By incorporating heavy-metal ions into formerly invisible particle components, they can be made visible. In some cases contrast variation is not possible without destroying the sample structure because changing the solvent composition or staining with heavy-metal ions is an invasive process. In such a situation, SAXS will not be of great use. Instead one

could use small-angle neutron scattering[5] (SANS) instead. SANS is a paragon of contrast variation owing to the enormous contrast difference between hydrogen and deuterium. Another method to help out from low-contrast situations would be anomalous small-angle X-ray scattering[12] (ASAXS), which measures the scattering pattern at two different wavelengths. One of them close by the absorption edge of a particular atom, which then gains in contrast considerably. Both methods, however, are only possible at large-scale facilities, such as atomic reactors or spallation sources (neutrons) or synchrotrons (tuneable wavelength).

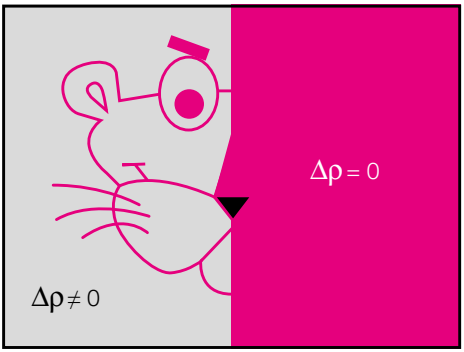

Fig. 11
The contrast in SAXS is the difference of electron densities (shown as pink color) between particle and environment. A pink panther in a pink room is invisible with the exception of the nose which remains visible due to its non-zero contrast.

When a particle with electron density of ρ_1 is embedded into a matrix of electron density ρ_2, then the scattered intensity of the particle is

$$I_1(q) = I_0 \cdot \rho_1^2 \cdot V_1^2 \cdot P(q)$$

Equation 6

where $\Delta\rho = \rho_1 - \rho_2$ because the intensity of the matrix is already subtracted.

Hence, an ensemble of identical particles causes an intensity of

Equation 7

$$\Delta I(q) = N \cdot \Delta I_1(q) \cdot S(q)$$

where *S(q)* is the structure factor considering the particle positions relative to each other. In the case of a dilute system, the approximation *S(q)* = 1 holds.

One consequence of Equation 6 is that the SAXS signal increases strongly with the particle volume. Because the volume of a spherical particle increases with the third power of the radius, the SAXS signal increases with the sixth power of the particle radius. Consider a dispersion that contains one million particles of 1 nm radius and just one particle of 10 nm radius (i.e., 1 ppm of the bigger particles). This sample will produce a scattering pattern with equal amounts of intensities from both sizes. You will have to record many electron-microscopic pictures in order to find this one big particle!

The other consequence of Equation 6 is that the squared contrast is responsible for the SAXS signal. This means that the sign of the contrast has no effect at all. Voids in a matrix material give the same intensity as material particles in a void matrix. It is solely the judgment of the experimenter, which parts of the sample are considered "particles."

➤ 3.9. Polydispersity

The assumption that all N particles in a sample are identical is rarely true. Protein solutions are one of the few exceptions of a so-called "monodisperse" sample, where all particles have the same size and the same shape. Usually the sample particles have all different sizes, which is called "polydisperse" or have different shapes, which is called "polymorphous."

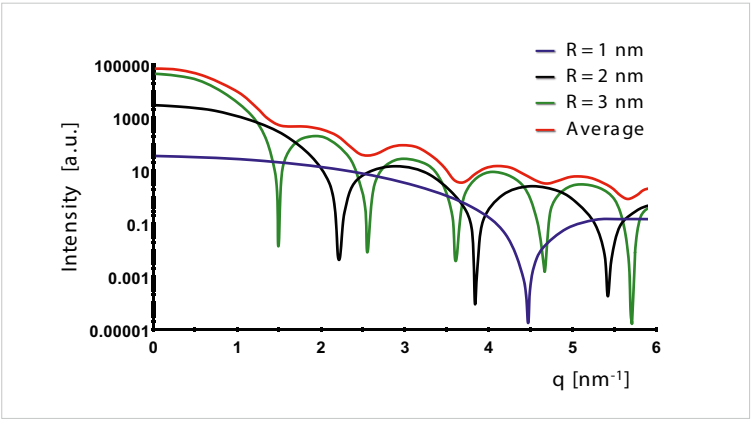

Fig. 12
The sum (red) of the form factors of different particle sizes makes the minima vanish gradually.

The scattering curves of polydisperse or polymorphous samples can be regarded as the sum of all N form factors $P_i(q)$, weighted with the respective contrast $\Delta\rho_i$ and volume V_i of the i-th particle. If we assume a dilute particle dispersion (i.e., $S(q) = 1$), then

$$\Delta I(q) = I_0 \cdot \sum_{i=1}^{N} (\Delta\rho)_i^2 \cdot V_i^2 \cdot P_i(q)$$

Equation 8

The result of this summation is an averaged form factor, which no longer exhibits sharp minima (see Fig. 12). On the other hand, an experimental scattering profile with well-developed minima indicates a monodisperse sample.

➤ 3.10. Surface scattering

The principles stated in the previous sections are also valid when the sample is distributed over the surface of a flat substrate and is measured in reflection geometry. Particularly, when the angle of incidence (θ_i) is large compared to the critical angle (θ_c) of the sample (or substrate). The critical angle is the angle below which the sample becomes totally reflecting and the X-rays can

no longer penetrate the sample surface. If the angle of incidence is kept close-to-critical (i.e., $\theta_i < 3\theta_c$), then the scattering theory needs additions because the reflected and the refracted beams (see Fig. 13) lead to additional scattering processes, which interfere with particle scattering produced by the direct beam. Scattering curves (GISAXS) and reflectivity curves (XRR) in this regime are preferentially modeled with the so-called Distorted-Wave Born Approximation.[15]

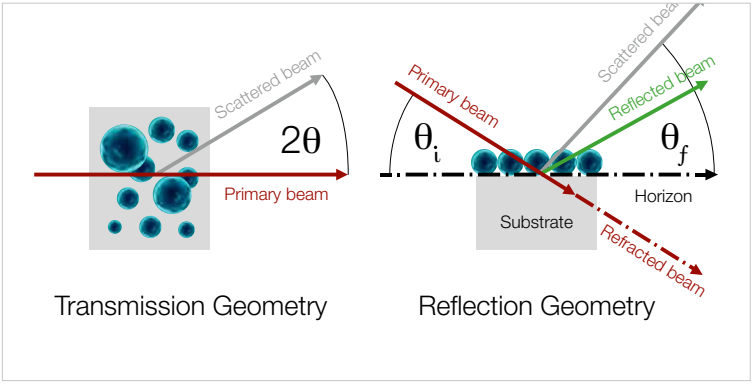

Fig. 13
Transmission (left) and the reflection geometry (right) of SAXS experiments. In reflection geometry the detection plane is split up into a refracted (below the horizon) and a reflected scattering pattern (above the horizon). The refracted pattern is rarely observed due to the high absorption of the substrate. The directly-reflected primary beam is the so-called specular beam.

By choosing the incident angle (below or above the critical angle) you can select the depth at which to measure the particles. You can selectively measure surface particles or you can include embedded particles of buried sample layers. All you need to know is the critical angle of each layer. The critical angle is a material constant, because it is established by the refractive index of the material, $n = 1 - \theta_c^2/2$. It can be calculated[13][14] from the electron density (chemical composition and density) and the absorbance of the sample material. Typical critical angles are between 0.2° to 0.5°.

Reflection experiments always give rise to two superimposed signals. The directly reflected (specular) beam ΔI_{spec} and the diffuse

scattering ΔI_{diff}. The specular beam is due to total reflection. As in the case of light being reflected by a mirror, it can be observed in one direction only ($\theta_f = \theta_i$), (see Fig. 14, red curve). The diffuse scattering is due to surface roughness (or particles) and can be observed at all angles (see Fig. 14, blue curve).

$$\Delta I_{total}(q) = \Delta I_{spec}(\theta_i) + \Delta I_{diff}(q)$$

Equation 9

In reflection geometry the definition of q has a slightly different appearance,

$$q = \frac{2\pi}{\lambda} \cdot \left[\sin\theta_i + \sin\theta_f\right]$$

Equation 10

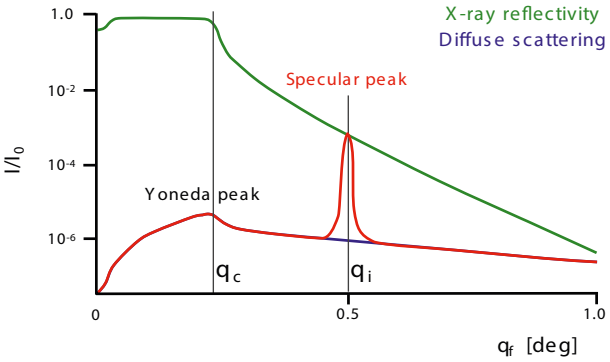

Fig. 14
Profiles of a plain surface as obtained (green) by XRR in reflectivity mode (θf = θi) and (blue+red) by GISAXS in diffuse scattering mode (θi = const).

Depending on the way of how the angles θ_i and θ_f are chosen, we find three methods commonly used to characterize surface-near structures.

1. **X-Ray Reflectivity (XRR):** In this experiment the detection angle is always the same as the incident angle, $\theta_f = \theta_i$. Both angles are scanned simultaneously. Only the directly reflected beam is recorded. The quantity of interest is the density profile along the surface normal. So, layer thickness is the main topic addressed by XRR. Surface roughness reduces the reflected beam intensity by increasing the diffusely scattered intensity. Strong roughness can make XRR experiments impossible.

2. **Grazing-Incidence SAXS (GISAXS) and Diffraction (GID):** In these experiments the angle of incidence is kept constant and close to the critical angle, $\theta_i = \text{const} \approx \theta_c$, and the detection angle is arbitrary in one or two dimensions. The magnitude of the detection angle determines whether it is a small or a wide-angle (i.e., diffraction) technique. The specular direction is sometimes avoided due to the overlap with the intense specular reflection (when $\theta_i \approx \theta_c$). This method scans for lateral structures/particles/roughnesses, which are spread over the surface or are embedded in the surface layer of the sample. It is complementary to XRR because its intensity increases with surface roughness. If the surface roughnesses of neighboring layers are correlated, then even the surface thicknesses can be determined as is preferentially determined by XRR.

3. **Constant-q Experiment (Rocking-Curve Scan):** This is a variant of the GISAXS method by which the sum of incidence and detection angle is kept constant, $\theta_f + \theta_i = \text{const}$, i.e., only the sample rotates, while detection and source direction remain constant. It is used for the same purpose as GISAXS, but the accessible particle sizes are much larger (due to the small x-component of the scattering vector, see „Data interpretation in reflection mode“ on page 82) and the surface structures are sampled along the beam direction rather than in the lateral direction.

The advantages of these methods lie in their intrinsic property of sampling large surface areas simultaneously due to the small incident angles.

Scattered and reflected waves interfere at the detector and give additional features, which are not observed with ordinary SAXS.

1. The most prominent feature is the so-called Yoneda peak (see Fig. 14). It is produced by surface waves (which are induced by the refracted beam) and it appears always at the critical angle away from the surface horizon, i.e., $\theta_{Yoneda} = \theta_i + \theta_c$ as measured from the direction of the primary beam. Every layer in the sample with a different electron density gives its own Yoneda peak, provided that the layers above can be penetrated at the chosen angle of incidence.

2. In contrast to the Yoneda peak, the directly reflected beam (i.e., the specular peak) appears in a GISAXS profile always at twice the incident angle $\theta_{spec} = 2\theta_i$ (see Fig. 14).

Both (peak) intensities depend on the Fresnel reflectivity coefficients of the sample as described by S.K. Sinha[15] for a single surface. The intensities of multiple rough layers were calculated by V. Holy et al.[16], [17] The diffuse scattering of many particle systems on surfaces were implemented by R. Lazzari[18] in a simulation and fitting program called IsGISAXS. A good overview and details about surface scattering with X-rays is given in the book of M.Tolan[19] and shall not be repeated here.

4. The SAXS instrument

The basic components of all SAXS instruments are an X-ray source, a collimation system, a sample holder, an optional beamstop and a detection system. The source irradiates the sample, and the detector measures the scattered radiation from the sample in a certain range of angles. The collimation system makes the beam narrow and defines the zero-angle position. The beamstop prevents the intense primary X-ray beam from hitting the detector. Without a beamstop, the resulting scattering from the detector's protective window would overlay the relatively weak scattering from the sample.

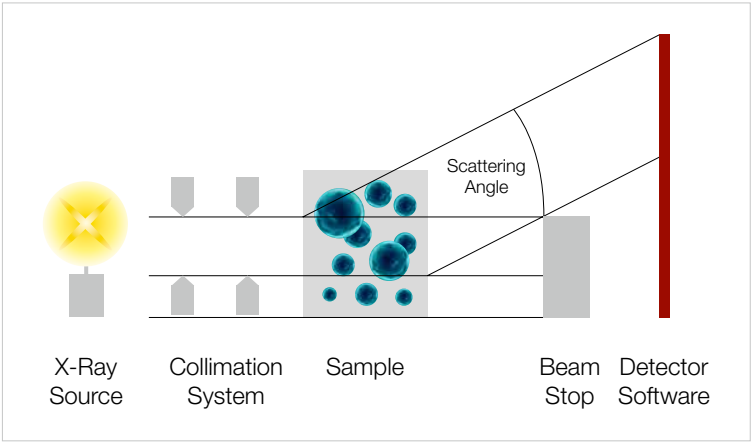

Fig. 15
The components of a SAXS instrument.

Modern solid-state photon-counting detectors can be operated also in a beamstop-less mode as these detectors can reliably detect very high intensities. This is the case especially in laboratory environments: the extremely high flux at synchrotrons might still harm the detector and make the use of a necessary. In case of older detection systems (e.g., image plates, CCD detectors) the use of a beamstop is indispensable because the direct beam will saturate or even harm these types of detectors.

Today, SAXS measurements are performed both in the laboratory and at synchrotron radiation facilities. Laboratory instrumentation includes dedicated SAXS systems (point or line collimation) as well as X-ray diffraction (XRD) systems, which can also be used for SAXS measurements to a certain extent – in particular with special setups enabling evacuation of the X-ray beam path.

➤ 4.1. The X-ray source

In laboratory SAXS systems, the source is typically a microfocus X-ray tube, a sealed X-ray tube, a rotating anode or a liquid-metal anode. Above all, synchrotron radiation facilities provide the highest photon flux and they also allow the use of different wavelenghts.

4.1.1 Microsources

In recent years, microfocus X-ray sources have become the de-facto standard X-ray sources for laboratory SAXS instrumentation. In these sources the electrons are focused into a small spot on the anode. The X-rays therefore are emitted from a small area of about 20 µm to 50 µm in diameter. This facilitates the production of narrow beam profiles with high brilliance (photon-flux density) for point-collimation experiments. Because of these small beam dimensions, unnecessary photons are spared, which would not go through a narrow slit or pinhole system anyway.

In laboratory SAXS experiments microsources are usually powered with 30 to 50 watts so that an ordinary water circulator or even air cooling is sufficient to operate them. Also, they are basically free of maintenance during the X-ray tube lifetime. Microsources are therefore a very cost-effective solution for laboratory SAXS instrumentation.

4.1.2 Sealed X-ray tubes

The basic design of an X-ray tube is shown in Fig. 16. It contains a filament (wire) and an anode (target) placed in an evacuated

housing. An electrical current heats up the filament so that electrons are emitted. Some high voltage (around 30 kV to 60 kV) is applied across the filament and the anode so that the electrons are accelerated towards the anode.

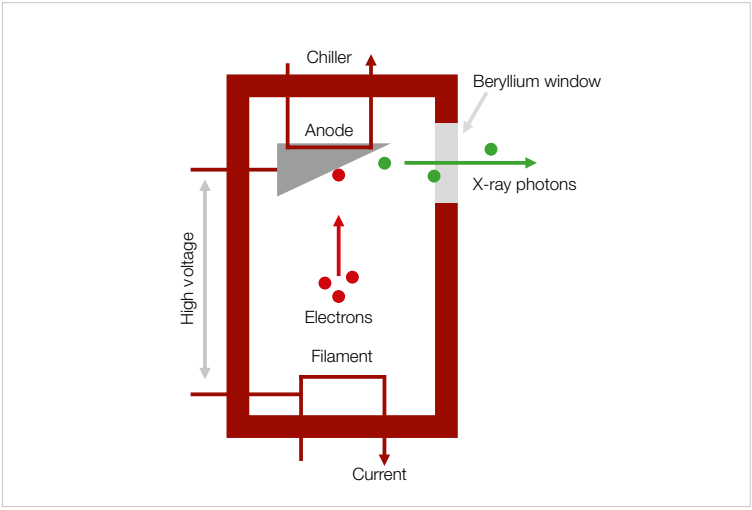

Fig. 16
The basic design of a sealed tube.

When the electrons hit the anode they are decelerated, which causes the emission of X-rays. This radiation is called Bremsstrahlung (German for deceleration radiation) and it is a broad spectrum of wavelengths with energies not exceeding the applied high voltage (e.g., 40 kV limits it to 40 keV). A fraction of the electrons will expel electrons from the atoms of the anode. An internal rearrangement of the remaining electrons then causes emission of characteristic fluorescence radiation with wavelengths typical for the material of the anode (for SAXS mostly copper).

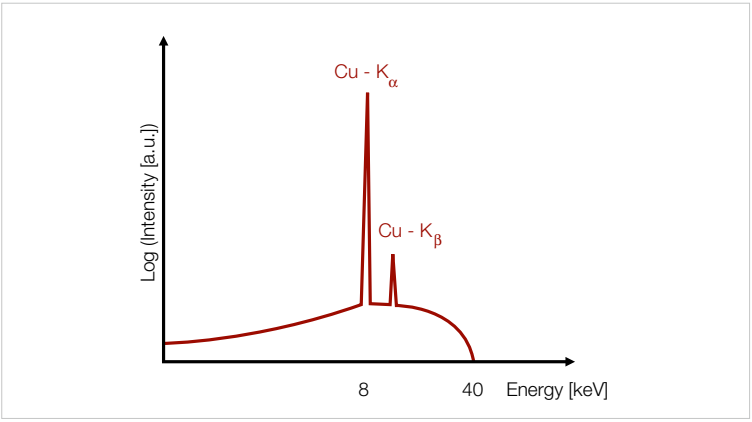

Fig. 17
The emitted wavelength spectrum of a copper tube operated at 40 kV.

The intensity of the X-ray tube (i.e., the number of photons) is controlled by the number density of electrons (current) that hit the anode. Usually the copper tubes are operated with 2 kW, which can be achieved by setting the high voltage to 40 kV and the electron current to 50 mA.

4.1.3 Metal-jet X-ray sources

Metal-jet X-ray sources are a special type of microfocus X-ray source in which the solid target is replaced by a jet of a liquid metal alloy. The constantly moving target reduces the damage of the electron beam to the target material and therefore allows to use of higher power loads. In essence, metal-jet sources can be operated at relatively high power densities, resulting in very high photon flux and brilliance of the X-ray beam. This makes this type of source ideal for experiments in particular on weakly scattering samples or in-situ measurements, where measurement time is critical. It is to be noted that metal-jet X-ray sources require regular maintenance and therefore the cost of ownership is higher than for, e.g., sealed microfocus X-ray sources and more comparable to rotating anode X-ray sources.

4.1.4 Rotating anodes

The bombardment of the anode material with electrons causes aging effects. These are basically grooves or holes, which are burned into the anode material and finally lead to a break-down of the X-ray tube. In order to enhance the lifetime of the source, the anode can be made into a rotating wheel. The bombardment of the anode is then distributed over the whole circumference of the wheel and the reduced wear per area increases the life time or enables higher power settings. People choose this type of X-ray source mostly to increase the electron current and thus the intensity output. The photon flux of a rotating anode can be up to 10 times higher than that of a sealed tube. But also the maintenance costs are 10 times higher than that of a sealed tube. In addition, the work load to keep the anode chamber clean enough to obtain a high vacuum definitely requires permanently employed staff.

4.1.5 Synchrotron radiation

Synchrotron facilities provide X-rays of all wavelengths as a by-product of forcing charged particles (electrons or positrons) to move along a circular (or wiggly) path at high speed. This process produces Bremsstrahlung and therefore a continuous wavelength spectrum is available. The power consumption of a synchrotron facility is enormous and the photon flux is accordingly. Because the charged particles are moving in bunches, the synchrotron radiation is a pulsed source. The intensity from a synchrotron is not constant over time. It decays due to the dissipation of charged particles, and it needs to be refreshed by injecting new particles from time to time.

At almost every synchrotron one or more beam lines are available for specially dedicated experiments such as SAXS. Projects must be formulated and applied for at the synchrotron stations. After a reviewing process and upon acceptance the applicant is granted a time slot from a few hours to a few days once or twice per year.

Usually those applicants are favored for acceptance who can show that high flux is mandatory for the success of their experiments and that previous screening experiments (e.g., with laboratory instruments) have indicated that their samples are suited for the synchrotron application.

➤ 4.2. The collimation system

In SAXS the biggest challenge is to separate the incoming beam from the scattered radiation at small angles (around <0.1°). If the incoming beam has a larger divergence than this small-angle requirement, then it becomes hard to distinguish the relatively weak intensity of the scattering pattern from the much higher intensity of the direct beam. Therefore the divergence of the incoming beam must be kept small.

Hence, a collimation system is required. This is basically a system of slits or pinholes through which the beam has to pass. In order to make the beam narrow, the slits or pinholes must be very narrow and far away from each other. But this cuts down the intensity of the incident beam considerably. As a trade-off one allows the slit or pinhole size to be larger than zero but at the cost of instrumental broadening of the results, called slit smearing.

Usually, the X-rays that are emitted by the source are polychromatic, which means they are a mixture of photons of different wavelengths. A sample that scatters the photon of one wavelength into one specific direction (angle) will scatter the photon of another wavelength into a different direction. Polychromatic radiation is therefore another cause for instrumental broadening, called wavelength smearing.

In order to prevent wavelength smearing, multilayer optics can be used to monochromatize the beam. These optics diffract X-rays of only one particular wavelength λ according to Bragg's law, $n\lambda = 2d \sin(\theta/2)$, with a typical multilayer d-spacing of about 4 nm.

The wavelength can be selected by tilting the multilayer by an angle with respect to the direction of the incident beam. The integer θ indicates that also n-times shorter wavelengths can pass through, but these are suppressed by the special design of the multilayer.

SAXS instruments are normally classified in two categories according to the collimation system employed:

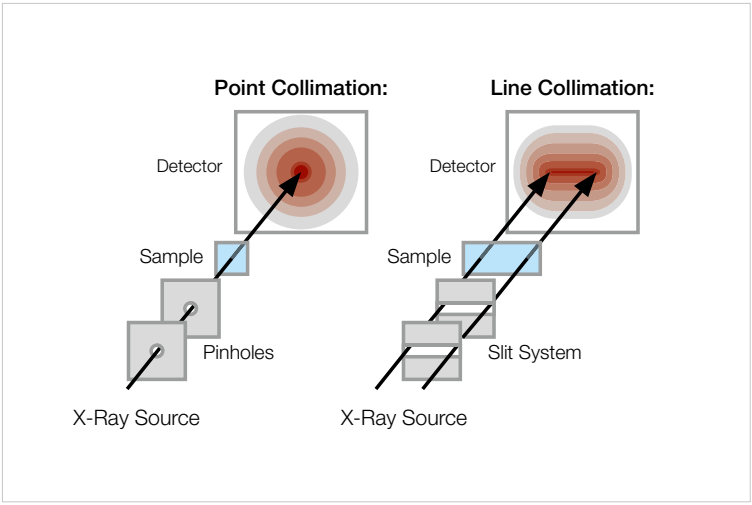

Fig. 18
The two collimation systems used in SAXS instruments.

(1) Point-collimation instruments have pinholes (either pinholes with a fixed size or technically more advanced motorized scatterless slit assemblies that allow adjusting the aperture) that shape the beam to a small circular or elliptical spot. Only a small spot of the sample is illuminated. The beam dimensions at the sample position are typically 0.3 x 0.3 mm^2. The scattering is therefore centrosymmetrically distributed around this illuminated spot, and the 2D pattern in the detection plane consists of concentric circles around the primary beam (Fig. 18). The scattering patterns have only little slit smearing, which is mostly neglected in subsequent data evaluations. However, at small angles this slit smearing can become evident and non-negligible even with point-collimation systems.

Point-collimation instruments are widely used and needed in particular for anisotropic (oriented) materials whenever orientation distributions are investigated (Pole figure, RheoSAXS) as well as when small sample areas (Microdiffraction) or surface properties (GISAXS, GIXD) are investigated.

(2) Line-collimation instruments confine the beam only in one dimension so that the beam profile is a long but narrow line (typically 20 x 0.3 mm^2). The illuminated sample volume is much larger than in point collimation (up to 100 times) and the scattered intensity (at the same flux density) is therefore bigger by the same amount. The beam profile can be made cleaner than with point collimation so that a small sample-to-detector distance can be exploited to the full. In consequence, the intensity is larger by another factor of about 10 (due to the $1/R^2$-dependence of the scattered intensity, see „Intensity and contrast“ on page 24).

The large sample volume however causes broadening (slit smearing) of the scattering pattern (see Fig. 18) so that the beam profiles must be measured and incorporated into the data evaluation. Slit smearing becomes increasingly negligible with larger scattering angles so that the benefit of high intensity is not compromised in the wide-angle region. At smaller angles the smearing effect can be eliminated by an additional mathematical treatment, called “desmearing” (see „Correction for collimation and wavelength effects“ on page 57). This can be performed with several software packages.[20]-[22]

Line-collimation instruments are ideally suited for non-oriented (= isotropic) systems, such as diluted dispersions and emulsions, and for the screening of large sample volumes.

➤ 4.3. The sample holder

The most complicated part of a SAXS system is the sample holder. This is because most samples cannot stand the vacuum, which is required to keep background scattering low. Also it is often the

change in structure, which is investigated in response to a changing environment or process parameter such as temperature, pressure, flow/shear rate, humidity, strain, projection angle and many others. This huge variety of different parameters makes it impossible to design one general setup, which can make each and every scientist happy. Therefore most sample holders are either completely homemade or are variants of commercially available setups. We cannot ignore the importance of a suitable sample holder but we have to limit our efforts by mentioning only the most basic setups in the experimental section below (see „Sample preparation“ on page 48).

➤ 4.4. The beamstop

The function of the beamstop is to prevent that the intensive direct beam hits the detector. Although some detectors are not necessarily destroyed by high intensities, the strong backscatter from the detector material can overshadow the relatively weak signal from the sample.

Two different types of beamstops are in use. One type consists of dense materials, such as lead or tungsten, which blocks off the direct beam completely. The other type is made of transparent materials which attenuate the beam to an intensity level that can be handled safely by the detector.

The advantage of a transparent beamstop is that the intensity of the direct beam is monitored simultaneously with the sample scattering. Thus, eventual drifts of the generator intensity are easily compensated by normalizing to the same beam intensity. Also the position of the beam and its profile is simultaneously measured in every experiment. Extra experiments to determine the beam-profile and of the zero-angle position are no longer required. However, it must be kept in mind that the material of the transparent beamstop can contribute to the background signal.

The transmitted beam intensity can be used to correct for the absorption of the sample without the need to do extra experiments. However, this absorption correction fails when strong sample scattering towards zero scattering angle is not negligible (e.g., the scattering of powders).

It is noteworthy that modern, CMOS-based detectors systems also allow for reliable beamstop-less experiments as long as the intensity does not exceed a specific threshold. Completely omitting the beamstop has certain advantages such as no beamstop artifacts and a more straight-forward data evaluation.

➤ 4.5. The detector

In modern SAXS synchtrotron beamlines and laboratory SAXS systems mostly photon-counting solid state (CMOS) is in use. In older systems also imaging plates, CCD detectors and wire detectors are used. Some general specifications of varying importance must be considered when selecting a detector.

1. **Resolution:** It is the ability of the detector to identify two neighboring points (pixels) as separated. A high spatial resolution means that the detector has many pixels per length and that the cross-talk between the pixels is negligible. Cross-talk between pixels happens when the intensity of one pixel to a certain degree spreads to neighboring pixels. A high resolution is important for small SAXS instruments.

2. **Linear dynamic range:** It is the range of photon flux which can be converted into exactly proportional intensity values. Usually detectors become less sensitive towards higher flux (called detector saturation). This means that an increase of photon flux by a factor of two does not lead to an increase of the recorded intensity by the same factor. Integrating detectors can add to their linear dynamic range by their high precision.

3. **Precision:** It is the accuracy and stability of the read-out intensity values. If still significant signal remains after subtraction of a background of similar intensity, then the precision is high and additional decades of linear dynamic range are gained on the low intensity side. If only noise remains, then the precision is poor. Every SAXS measurement requires two experiments which then must be subtracted. This is therefore an important specification for SAXS.

4. **Sensitivity:** It indicates how efficiently incoming photons are counted. It is measured in quantum efficiency (QE) values, i.e., the percentage of photons that are effectively counted. QE goes hand in hand with the absorption of the detector medium. Because most detectors nowadays have QE-values at around 90 % (with the exception of wire detectors, which have about 60 %), little can be improved on this side. It is a less important specification for SAXS unless a shorter wavelength than copper radiation is used.

5. **Dark-count rate:** It is the intensity that the detector records even though no X-ray beam is switched on. It is mostly attributed to thermal processes and can be removed by cooling the detector or by filtering the electrical pulses according to their height. Modern solid state photon-counting detectors have no dark current at all, however, detectors with a substantial dark-current rate (e.g., CCD detectors, imaging plate detectors) must have a high precision in order to compensate for it.

6. **Frame rate:** It is the number of scattering patterns (pictures) which can be recorded per second. This does not determine the speed of SAXS experiments or the time resolution of so-called “time-resolved SAXS.” The speed is rather determined by the number of scattered photons per second. In order to obtain a scattering pattern in an acceptable quality, a sufficient number of photons must be recorded. So, the bottleneck is not the frame rate of the detector but the number of the scattered photons per second. The frame rate is a less important specification for SAXS.

4.5.1 Solid state (CMOS) detectors

Solid state detectors are Si-diode arrays (1D and 2D) which record the X-ray photons directly. When X-ray photons hit the semiconductor material, they produce ion pairs which are actually counted. Additional circuitry (op-amps) then selectively counts only those pulses that are above a certain energy threshold. In this way the dark count rate and also fluorescence of longer wavelengths can be eliminated. Because silicon does not absorb so much short-wavelength radiation, their quantum efficiency reduces substantially when wavelengths shorter than copper are measured.

They can stand rather high radiation doses and maintain their linearity up to intensities close to that of the primary beam of a 2 kW sealed-tube source. Their radiation hardness is not unlimited, though, because direct-beam intensities (e.g., of a synchrotron) applied for a longer period of time can cause damages, which result in a permanently reduced quantum efficiency. The costs of these detectors are in the same order of magnitude as that of a CCD detector.

4.5.2 Imaging plate detectors

Imaging plates (IPs) are made of a material that stores the X-ray energy by exciting its electrons into so-called F-traps. These are meta-stable energy states from which the electrons can be brought back by illumination with a laser beam. Thereby visible fluorescence radiation is produced, which is measured by a photo-multiplier or an avalanche photodiode. IPs are flexible sheets which are exposed just as photographic films and are scanned by a separate device in a second step. After the readout (digitization), the imaging plates are cleared by a light-pad before they can be used again. They can be reused thousands of times until mechanical damage causes the end of their life. IPs have have a comparably high linear dynamic range and they can be produced in virtually any shape and size. But they usually need to be scanned by an external device, which makes automated experiments difficult. IPs must

be handled in darkened labs because illumination with ambient light leads to erasure of the scattering pattern. The dark-count rate depends on the scanner model but is usually small, constant and easy to subtract. Also the pixel size depends on the scanner model and lies typically between 25 µm and 100 µm. The pixel cross-talk, however, is substantial. IPs have almost no maintenance costs and they are not easily damaged by overexposure.

4.5.3 Charge-coupled device (CCD) detectors

CCD cameras work like ordinary video cameras. They detect visible light, which is produced by a fluorescence screen. A plate made of glass fibers, a so-called taper, is mounted between the video chip and the fluorescence screen. It guides the light to the chip and maps the fluorescence pattern with little distortion. A beryllium window or an aluminum-coated plastic foil prevents ambient light from spoiling the detection of the comparatively weak fluorescence. The CCD is an integrating detector, i.e., it collects the produced electrons in every pixel (= capacitor) until read-out. Only the resulting charge is recorded and not the photon impact itself. This has two important consequences. First, the noise amplitude of a CCD detector is not the square root of the recorded intensity (i.e., no Poisson statistics, see „Exposure time“ on page 51). Second, no filtering of pulses is possible to eliminate the dark-count rate. So, CCDs need efficient cooling to keep the dark-count rate as low as possible. The dark-count rate also depends on the acquisition time so that it has to be measured quite frequently (instead of once and for all). CCDs have the capability of on-chip binning, which connects neighboring pixels and thus increases the precision considerably. Usually the pixel sizes are small (around 25 µm) and the cross-talk affects hardly more than three neighboring pixels so high-resolution experiments are possible. High-intensity spots, however, can lead to blooming (i.e., extreme cross-talk over the whole chip width), which calls for corrective actions after the acquisition (anti-blooming correction). The chip sizes are relatively

small (max. 5 cm x 5 cm), which limits the angular range. CCD cameras are relatively expensive, depending on the chip quality (specified by the number of failing pixels).

4.5.4 Wire detectors

These have thin wires inside an absorbing gas atmosphere (Xe or Ar/Methane). One X-ray photon that enters this atmosphere expels an electron from the gas molecules. The electron is accelerated towards the wire by the applied high voltage (bias). When the electron hits the wire an electrical pulse is induced. The pulse propagates towards both ends of the wire, where it is recorded. The time difference between the two arrivals is used to determine the position where the electron hit the wire. One wire delivers a 1D scattering profile and many wires running parallel can be used to produce a 2D picture.

Wire detectors usually have large pixel sizes (around 100 µm) and a poor spatial resolution. A larger sample-to-detector distance can be a cure for this, but only at the cost of a diminished angular range and a reduced intensity. Wire detectors have a negligible dark-count rate, however, they can be easily damaged by overexposure and are costly to maintain.

5. SAXS analysis

In order to make a good analysis, it is important to have a well-prepared sample and a good data quality. After the sample is measured, the data are analyzed. This is done in various ways and in various extents, depending on the type of sample and on the intent of the investigation.

➤ 5.1. Sample preparation

The SAXS signal can be optimized by employing a large illuminated sample volume (scattering volume).

- **In transmission mode (SAXS):** A thick sample is not desirable due to the increased sample absorption (see „Absorption“ on page 15). So, the only way to maintain a large scattering volume is to widen up the beam dimensions and to keep the optimum sample thickness, which (for water-based samples and copper radiation) is about 1 mm. Typical sample sizes are 50 µL for liquids and 1 x 1 mm^2 (point collimation) to 1 x 20 mm^2 (line collimation) for solid samples or pastes.

- **In reflection mode (GISAXS):** The sample thickness is of no concern because only the topmost surface layers are probed. The only way to maintain a large scattering volume is to increase the sample length. The footprint of a 0.3 mm high beam on a flat sample with an inclination angle of 0.2 degrees is 86 mm.

Everything that is put inside an X-ray beam, even air, produces scattering. It is therefore good practice to keep the sample-to-detector distance in vacuum. Unfortunately, many samples are destroyed when put into vacuum and need to be kept at ambient conditions. Therefore, special sample holders are necessary to keep the samples fit for the scattering experiments.

5.1.1 Liquids

Liquid samples in transmission mode are measured inside a thin-walled capillary the thickness of which should be around 1 mm when the liquid contains mainly water or hydrocarbons. Solvents that contain heavy atoms, e.g., chlorine, and have a large density absorb too much and must be measured in thinner capillaries (Table 2). Liquids that are so viscous that, in a lifetime, they could not be filled into a capillary are better measured in a paste cell.

5.1.2 Pastes

Pastes, rubbers, and vacuum sensitive materials in general have to be squeezed into a sample holder that has removable windows. The window material must be transparent to X-rays, should not scatter much and should be resistant to chemical attack and elevated temperatures. The most widely used window material certainly is a foil made of Kapton®. Other window materials are also possible but depend on the requirements of the respective application.

5.1.3 Solids

Solids can be clamped onto frames with or without additional window foils for protection against the vacuum. The sample thickness can and must be chosen according to the respective absorption. In case of special atmospheric requirements, such as a specified relative humidity or a gas reaction, the sample must be put into a small compartment which is then inserted into the vacuum. These can be technically quite challenging and are usually also expensive.

5.1.4 Powders

Powders can be measured between two layers of sticky tape or in (disposable) capillaries. Not every powder is suitable for SAXS

investigations, particularly when the grain size or shape is the desired parameter. With the exception of the specific surface of a powder, only internal structure elements can be found with SAXS. So, the crystallinity on the atomic scale (in WAXS) or on the nanoscopic scale (in SAXS) are the only reasons why one would make scattering experiments on powders. The difficulty with powders, however, is that the grain size must be small enough to allow for a random-enough distribution of crystal orientations. This is necessary to be sure that all Bragg reflections fall into the detection area and thus all peaks are represented in the scattering profile. Not all powders can be ground sufficiently small. Also, sometimes crystals just form in the sample (mostly pastes or liquids) and grow fast enough to spoil the randomness of crystal orientations. In these cases it is a good idea to use a sample holder that rotates or vibrates in such a way that all crystals eventually move into an orientation that allows for their detection within the acquisition time.

5.1.5 Materials on a substrate

Sometimes materials must be prepared on a substrate in order to investigate thin-film properties. Normally one would choose to measure these samples in reflection mode (GISAXS). However, if transmission mode is the method of choice (e.g., for Pole figure analysis) one has to choose a substrate material which is sufficiently thin and transparent enough for that particular wavelength. If possible, ordinary X-ray window materials can be used. In many cases the scattering of the thin-film is much weaker than the scattering of the substrate, so that a transmission experiment becomes impossible. Again, the thin-films must be able to withstand vacuum conditions. But if they can stand only a normal (or a special) atmosphere, then they must be put into a small compartment that is inserted into the vacuum.

➤ 5.2. SAXS measurements

When the sample is in (or on) the holder the actual measurement can begin. This is done by exposing the sample to the beam. It is important to note that one measurement always consists of two experiments. The scattering of the matrix material (e.g., the solvent) and of the particle system must be measured in two separate experiments. In order to obtain the scattering from the particles alone, one must subtract the scattering of the matrix material.

If the intensities are required in absolute units, then additional experiments are required to calibrate the detector output with a standard material of known output intensity. Please note, however, that absolute intensity units are not required for the determination of a structure.

5.2.1 Exposure time

The statistical quality of the scattering pattern improves with increasing intensity. The standard deviation of the experimental intensity is equal to the square root of the intensity (i.e., law of Poisson statistics). Thus, it is necessary to measure four-times longer in order to reduce the noise by a factor of two. Clearly, a long exposure time is the recipe for data of good quality. On the other hand, long exposure times are not economical and a trade-off solution must be found anew for every sample.

Every detector has a specified saturation value expressed in counts. When this maximum number of counts is reached, then the time that was needed for it constitutes the maximum exposure time for this particular sample. Any further accumulations of counts would be lost in overflows. If the data still need further improvement, it can only be done by repeated exposures and by averaging all the resulting frames. Repeating short exposures is the preferred measuring mode for CCD detectors due to their low saturation value and the missing applicability of Poisson's law, which says

that the standard deviations of counted intensities are the square root of the intensity-values themselves.
In practice one determines the optimum exposure time by a short, say, 1 minute long screening experiment. If the interesting parts in the scattering pattern have reached M [a.u.] (arbitrary detector units) in t minutes, then the accuracy (relative standard deviation) of the data is $s = 100/\sqrt{M}$ %. If the aimed-at accuracy of s_{opt} is not yet reached, then the exposure time must be extended to $t_{opt} = (s/s_{opt})^2$. This rule of thumb applies to all detectors delivering counts as output. For CCD detectors it is still a good approximation.

5.2.2 Contrast

When the contrast between particle and matrix is zero, no prolonged exposure time and no synchrotron with high photon flux will help and make the particles visible. If possible, select a matrix material (solvent) in which the particles have a high contrast. Always try to use a matrix material which is less dense than the particles, or which is made of lighter elements. This helps to keep absorption losses small, too.

➤ 5.3. Primary data treatment

The distribution of the scattered X-rays is recorded in the plane of detection, which results in a two-dimensional scattering pattern, $I_{exp}(m_y, m_z)$, where m_y and m_z are the horizontal and vertical pixel numbers. Most of the times these are more data than are actually necessary. For example, the scattering of isotropic samples could equally well be described by a one-dimensional scattering profile. Similarly, the orientation angle of an anisotropic sample could be read off from an azimuthal 1D profile. Therefore, the amount of data can be reduced by averaging.

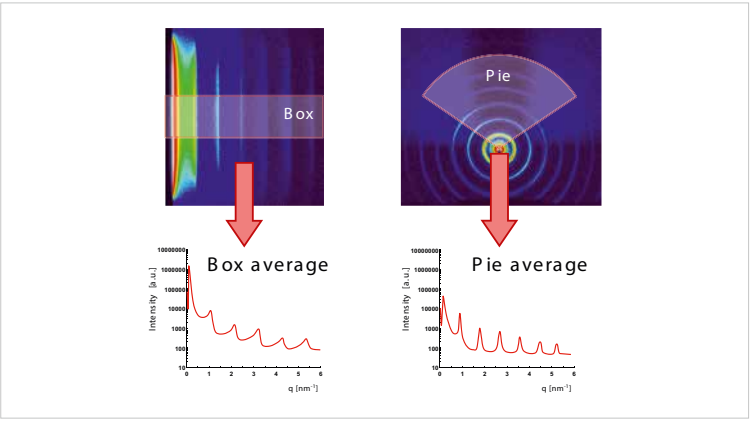

Fig. 19
The box geometry (linear average) and the pie geometry (circular average).

There are three geometries (see Fig. 19 and Fig. 20) to average the data depending on the intent of the investigation and on the collimation type of the instrument.

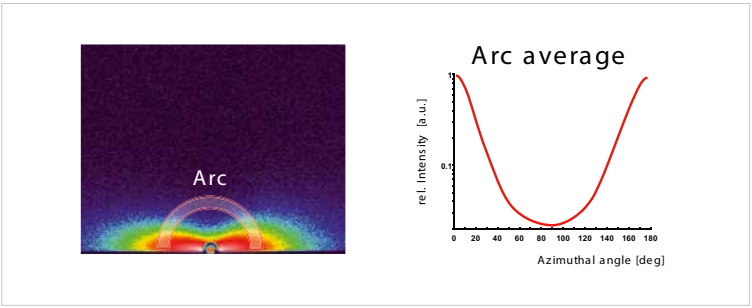

Fig. 20
The arc geometry (radial average).

Averaging also improves the statistical quality of the data. It must be done over a certain width, however, which broadens (smears) the profile. This width must be considered in the subsequent data evaluation procedure (see „Correction for collimation and wavelength effects“ on page 57).

The pixel numbers of the profiles are converted into q-values (or azimuth-angle values, ϕ) by taking into account the wavelength,

the pixel size and the sample-to-detector distance. In this way we obtain the 1D profiles $I_{exp}(q)$ and $I_{exp}(\phi)$.

5.3.1 Subtracting the background

What we have obtained so far are two experimental intensity curves, one from the sample $I_{s,exp}(q)$ and one from the matrix material $I_{M,exp}(q)$. Now we need to subtract one from the other in order to get the scattering of the particles only:

Equation 11

$$\Delta I(q) = I_{S,exp}(q) - I_{M,exp}(q)$$

This seemingly simple operation cannot always be applied as stated above. It works only when the sample and the matrix material have about the same transmittance, $T_s = T_M$. The transmittance is the ratio of transmitted versus incident photons. If a material is not absorbing, then its transmittance is 1. So, if the particles in the matrix absorb more than the matrix, $T_s < T_m$, then the scattered intensity of the sample will be reduced. A negligent application of Equation 11 will then deliver meaningless negative intensities. The experimental scattering curves therefore must be scaled by their respective transmittance values. But before any scaling can be applied, the data must be cleaned from the dark-count rate of the detector, $I_{dc}(q)$. One equation describing this absorption-corrected background subtraction would be

Equation 12

$$\Delta I(q) = \frac{I_{S,exp}(q) - I_{dc}(q)}{T_S} - \frac{I_{M,exp}(q) - I_{dc}(q)}{T_M}$$

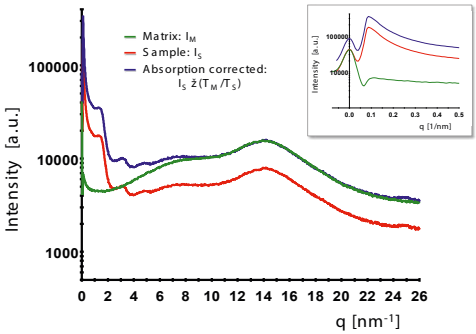

Fig. 21
The scattering curve of a dispersion of absorbing particles (red) in a matrix material (green) of low absorbance. Absorption correction brings the sample intensity (blue) slightly above the background intensity (green). The inlet shows the zoomed-out region of the primary beam.

In Fig. 21 an example is shown where negative values would result in a subtraction without an absorption correction.

Instead of determining all involved transmittance values, it is more practical to determine a scaling factor f_T, which brings the sample intensity above the background intensity. The final equation mostly used is therefore

$$\Delta I(q) = I_S(q) \cdot f_T - I_M(q)$$

Equation 13

where we have abbreviated, $I_S(q) = I_{S,exp}(q) - I_{dc}(q)$, $I_M(q) = I_{M,exp}(q) - I_{dc}(q)$. The scaling factor is effectively a relative transmittance correction, $f_T = T_M/T_S$, which is alright if absolute intensity units are not required. It can be easily obtained when the data reach into the wide-angle region (i.e., q >10/nm^{-1}) and the structure peak of the matrix material (see Fig. 21 at q = 14/nm^{-1}) is not changed by the presence of the dispersed particles. Just scale the sample curve by such a factor that a subsequent subtraction does not yield systematically negative numbers, $f_T \cdot I_S - I_M \geq 0$.

Note that the primary beam intensity (see inlet of Fig. 21) cannot always be used to find the scaling factor. Some samples scatter strongly towards $q = 0$. This scattering can compensate the losses due to absorption and the transmission value can no longer be determined by comparing the intensities at $q = 0$.

Once the obvious background, i.e., the scattering from the sample holder, the matrix material and the dark-count rate of the detector are subtracted, there possibly remains some incoherent scattering (Compton scattering or fluorescence) I_{inc}, which adds a constant to the scattering curve. Its presence can be quickly checked by drawing the background-subtracted data in a double-logarithmic plot:

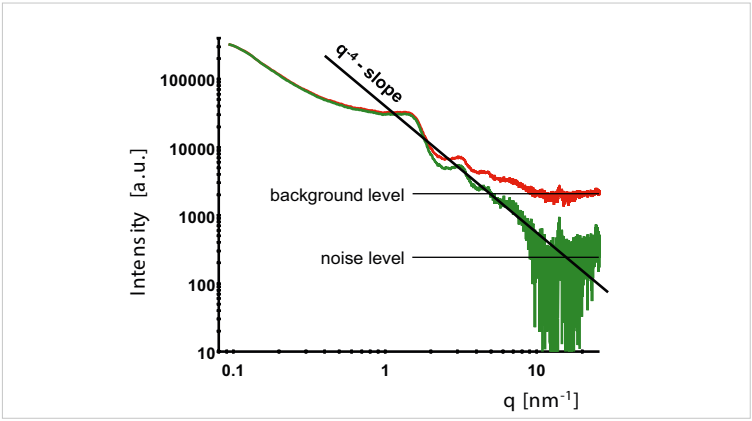

Fig. 22
A double-logarithmic plot of data (red) with and (green) without a constant background.

A constant background makes a scattering curve leveling off at large q-values (see Fig. 22). Once this constant is subtracted, then the scattering curves should follow a linear slope (of q^{-3} or q^{-4}) down to the noise level according to Porod's law, for point collimation $\Delta I(q) \approx K_P/q^4$ or for line collimation $\Delta I(q) \approx K_L/q^3$.

If the experimental scattering curve contains an unknown amount of constant background, then Porod's law can be used to calculate it by fitting a straight line into a so-called Porod plot of $y = q^4\Delta I(q)$ versus $x = q^4$ (see Fig. 23),

$$q^4 \cdot \Delta I(q) = K_P + B \cdot q^4$$

Equation 14

where the slope B = I_{inc}. For line collimation experiments q^3 is used instead of q^4 because of the instrumental broadening.

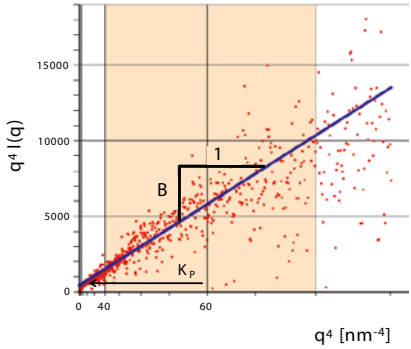

Fig. 23
The Porod plot of a scattering profile with a substantial amount of constant background B and the intercept KP.

5.3.2 Correction for collimation and wavelength effects

All theoretical scattering curves ΔI(q) (form factors and structure factors) which are described in textbooks are calculated for an ideal primary beam. An ideal primary beam has no length, width and has only one wavelength. In real life, a beam has finite length, width and wavelength profiles. That is the reason why experimental scattering curves ΔJ(q) are broader than the theoretical curves. They are said to be smeared. The most important smearing effect for SAXS is beam-length smearing when working with line collimation.

$$\Delta J(q) = \int_{-\infty}^{\infty} U(t) \Delta I\left(\sqrt{q^2 + t^2}\right) dt$$

Equation 15

The beam-length profile U(q) is a trapezoid, which is the measured beam profile additionally broadened by the averaging width of the detector. It can be approximated by a constant value so that a smeared scattering curve can approximately be regarded as the integral of its theoretical scattering curve, $\Delta J(q) \approx \int \Delta I(q) dq$. This is a very useful result because it immediately allows translating theoretical predictions into the case of line collimation. For example, Porod's law $\Delta I(q) \approx K_p/q^4$ for line collimation can be calculated quickly, $\Delta J(q) \approx \int K_p/q^4) dq \approx K_p/(-3q^3)$.

Also the inverse operation is possible. It is called desmearing and is effectively the first derivative of the experimental scattering curve. Therefore, also the noise content of an experimental scattering curve is magnified during desmearing.

Desmearing can be done in two ways:

1. **Model-free way**:[20] No assumptions on the scattering system are made. However, no difference is made between signal and noise. Therefore the noise level is equally increased as the waved features of the scattering curve. Longer exposure times can help to compensate the increase of noise. This method is recommended, if Bragg peaks are in the SAXS curve or no suitable fitting model can be found.

2. **Model-dependent way**:[21], [22] Theoretical scattering curves of a model are fitted to the data after they have been smeared with the experimental beam profiles. A fitting procedure automatically separates signal from noise in an effective way so that the results are always smooth. There is no increase of noise, but having chosen a wrong model can still lead to unacceptable results. This method is recommended, if the SAXS curve can be interpreted in terms of finite pair-distance distributions (see „Particle structure“ on page 70).

Nowadays, for SAXS applications wavelength smearing is history because multilayer optics make the wavelength distribution of X-ray tubes sufficiently narrow. Neutron scattering applications, however, still have to deal with it.

5.3.3 Intensities on absolute scale

Intensities are called “on absolute scale” if they are normalized by the flux density of the primary beam I_0 [a.u./cm^2] and the illuminated sample volume V_S [cm^3]:

$$\Delta I_{abs}(q) = \frac{\Delta I(q)}{I_0 \cdot V_S}$$

Equation 16

With modern photon-counting detectors, the absolute intensity can directly be determined (the sample thickness and transmission have to be determined). If this is not possible, then two additional experiments must be made to calibrate with a standard. In these experiments the empty sample holder (e.g., empty capillary) $I_{cap}(q)$ and the sample holder with the reference material (e.g., water) $I_{water}(q)$ are measured. The scattering of the empty sample holder must be subtracted in order to obtain the scattering of the reference material.

$$\Delta I_{water}(q) = \frac{\Delta I_{water+cap}(q)}{T_{water+cap}} - \frac{\Delta I_{cap}(q)}{T_{cap}}$$

Equation 17

If we divide the background-corrected sample intensities by the mean intensity of the reference material, then we obtain them in units of the reference. Once the absolute intensity of the reference material is known (e.g., $I_{water,20°C} = 1.641 \cdot 10^{-2}$ cm^{-1}), the intensities of the sample can be scaled to absolute units [cm^{-1}] too.

$$\Delta I_{abs}(q) = \frac{\Delta I(q)}{\langle \Delta I_{water} \rangle_q} \cdot I_{water(20\,°C)}$$

Equation 18

where $\langle \Delta I_{water} \rangle_q$ indicates an average value in a q-range, where ΔI_{water} is sufficiently constant. Using water as reference has the advantage that it fills the sample holder evenly and both, I_0 and V_S cancel, when we divide by the intensity of the water filled sample holder. So, Equation 18 can be readily exploited if water is the reference. Other reference materials, which are not liquid (e.g., glassy carbon), need a modification of Equation 18,

Equation 19

$$\Delta I_{abs}(q) = \frac{\Delta I(q)}{\langle \Delta I_{ref} \rangle_q} \cdot I_{ref} \cdot \frac{V_{ref}}{V_S}$$

where V_{ref} is the illuminated volume of the reference material. Converting intensities of solid samples into absolute intensity units is complicated because it is hard to determine the illuminated sample volume precisely.

The method of using reference samples works only if the intensity I_{ref} is known. In the case of water, it can be calculated theoretically.[23] Other reference materials need to be calibrated and certified, before they can be used. Such a calibration can only be made with an instrument[24] that is capable of measuring the direct-beam flux density I_0 and the scattering of the reference sample under identical conditions.

➤ 5.4. Data interpretation

Once the intensity of a sample is recorded and background corrected, the question arises as to which information can be obtained from it. We can summarize Equation 6 and Equation 7,

$$\Delta I_{abs}(q) = K \cdot P(q) \cdot S(q) \qquad \textit{Equation 20}$$

where we have lumped together all constant terms into. It is evident that there are three components to be considered. One is the constant, which consists of the particle contrast, volume, concentration, etc. This constant is important to know when the molecular weight of the particles is investigated.

The other factors, *P(q)* and *S(q)*, have their value in their angle dependence only. The intensity units are of no concern. The form factor *P(q)* bears the shape and the internal density distribution of the particles. The structure factor *S(q)* carries the information about particle-particle interactions, such as inter-particle distances and degree of order to name just a few. When distances and shapes are to be determined, then the first question should address the range of distances, which can be observed.

5.4.1 The resolution

Owing to its close relationship to microscopy (see „Scattering and microscopy“ on page 10), SAXS is equally limited in resolving details of structure. In any optical experiment, objects of size D can be detected only in a limited range, starting from a smallest distance D_{min} and ending at a largest distance D_{max}. In microscopy as well as in SAXS these limits are established by the wavelength of the radiation and by the aperture of the lens, i.e., the range of scattering angles $q_{min} < q < q_{max}$ between which the scattering pattern (or the form factor) is sampled.

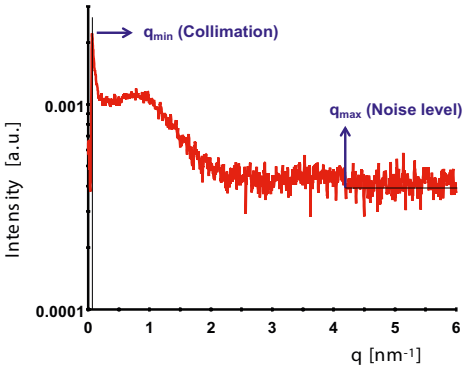

Fig. 24
The two limits for the resolution of a scattering curve.

The lower limit q_{min} is due to the presence of the primary beam and is governed by the quality of the collimation system. The upper limit q_{max} is due to the fading of the signal into the noise level. Without going into mathematical details (see the Nyquist theorem[26] of the Fourier transformation), we just give the result that a scattering profile, which is measured between q_{min} and q_{max}, can be used to resolve particle features only between D_{min} and D_{max},

Equation 21
Equation 22

$$D_{min} \approx \frac{\pi}{q_{max}} \qquad D_{max} \approx \frac{\pi}{q_{min}}$$

For SAXS the technological challenge is to reach a small q_{min} without disturbance of the signal by the much stronger direct beam. The quality of the collimation system and the alignment of the beamstop are the main ingredients which determine the accessible q_{min}. Therefore the quality of a SAXS device is usually specified in terms of q_{min} or D_{max}. Typical SAXS instruments have a resolution of about D_{max} = 30 nm to 50 nm.

Sometimes people specify the resolution by means of a largest "Bragg distance,"

$$d_{Bragg} \approx \frac{2\pi}{q_{Peak}}$$

Equation 23

where d_{Bragg} is the lattice spacing of a crystal plane whose reflection is hypothetically positioned at q_{Peak}. The discrepancy between d_{Bragg} and q_{Peak} is a factor of two. So, how come that a lattice distance two times larger than the resolution limit can be considered resolved? The answer is simple: It isn't. If a peak had its maximum at one end of a curve, then one could not even tell that it is a maximum. Not even its position would be determined. In order to call a peak resolved, it must lie within the curve. Thus a Bragg-peak position can never be used for a resolution specification because $q_{min} < q_{Peak} < q_{max}$ must hold.

5.4.2 Radius of gyration

Any form factor *P(q)* can be approximated by a Gaussian curve at small angles. According to Guinier (1939), the curvature of this Gaussian is due to the overall size of the particles, so that

$$P(q) \approx a_0 \cdot e^{-\left(\frac{R_G^2 \cdot q^2}{3}\right)}$$

Equation 24

The size parameter R_G is called the "radius of gyration." It is model independent. That means it contains no information about the shape or the internal structure of the particle. But if the structure of the particles could be assumed, then R_G could be used to calculate the particle dimensions. For example, if the particles are known to be spherical with an equal density everywhere inside (i.e., with a homogeneous density), then the average radius of such particles could be calculated from the radius of gyration by $R = \sqrt{(5/3 * R_G)}$. Other equations can be derived for any other particle shape.

The parameter a_0 is the extrapolated zero-angle intensity. In the equation above $a_0 = 1$ because P(0) = 1 by definition, but if ΔI(q) is used instead, then $a_0 = \Delta I(0)$, which can be used to determine the molecular weight (see „Molecular weight“ on page 68). In a so-called Guinier plot, the logarithm of the intensity is printed versus q^2,

Equation 25

$$ln[\Delta I(q)] = ln[a_0] - \frac{R_G^2}{3}$$

The parameters R_G and a_0 are determined by straight-line fitting from the slope $-(R^2_G/3)$ and from the intercept ln (a_0) as shown in Fig. 25.

Fig. 25
Guinier's plot of a form factor in order to determine the particle's radius of gyration RG and the zero-angle intensity a0.

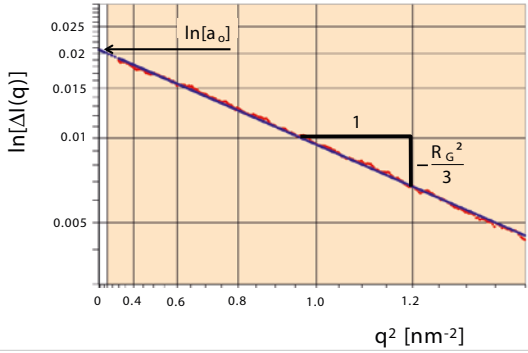

Interestingly, almost the same radius of gyration can be obtained, even if line-smeared intensity data ΔJ(q) are used instead of ΔI(q). This is not quite unexpected since the exponent of a Gaussian function does not change upon integration. Still, the radii of gyrations from line-smeared data come out too large (by about 4 %) due to Guinier's approximation that the form factor is equal to a Gaussian curve.

Note, that the obtained size parameter is the average of squares ($<R^2_G>$) and that only in sufficiently monodisperse cases the linear size parameter can be obtained by taking the square root,

$<R_G> \approx \sqrt{<R^2_G>}$. The monodispersity criterion is indicated in a Guinier plot, when the data points fall onto a straight line. If the sample is polydisperse (particularly when some particles are larger than the resolution limit), then the data points do not fall onto a straight line. In this case, the Guinier approximation fails and should not be applied. The only way out in such cases would be the calculation of the size distribution by inversion techniques (see „Polydispersity analysis“ on page 74).

At very small angles the data points suddenly drop below the fitted line (see Fig. 25). This sudden intensity drop is caused by the beamstop. The edge at q_{min} indicates the resolution limit of the instrument. Thus, a Guinier plot is very useful for finding the resolution limit (q_{min}) of an experiment.

When cylindrical particles are considered, then the “radius of gyration of the cross-section” R_C can be extracted by using

$$q \cdot P(q) \cong a_0 \cdot e^{-\left(\frac{R_C^2 \cdot q^2}{3}\right)}$$

Equation 26

This works even when the axial dimension is larger than the resolution limit because the form factor is multiplied by q, which cancels the contribution of the axial dimension (assumed to be infinitely long). The radius R of a circular homogeneous cylinder can then be calculated by $R = \sqrt{2}R_C$. When ΔI(q) is used in absolute units instead of *P(q)*, then a_0 is proportional to the molecular weight per unit length.

For lamellar particles a similar equation can be used,

$$q^2 \cdot P(q) \cong a_0 \cdot e^{-\left(R_T^2 \cdot q^2\right)}$$

Equation 27

where R_T is the thickness radius of gyration. For a homogeneous plate the half thickness R theoretically equals $R = \sqrt{3}R_T$. When

applied with absolute-intensity data, the parameter a_0 can be used to calculate the molecular weight per unit area.

5.4.3 Specific surface area

The small-angle X-ray scattering method can be used to obtain the specific surface area of porous materials and nanoparticulate systems. There are two general rules originating from Porod (1951) that apply to scattering profiles. The first rule states that the scattering profile of any particle system decays at large scattering angles with K_P/q^4, where the Porod constant K_P is proportional to the surface per sample volume. The other rule is that the second moment of any scattering profile is a universal constant, called the invariant (Q),

Equation 28

$$Q = \int_{-\infty}^{\infty} q^2 \Delta I(q) dq$$

The invariant contains instrumental factors which are not easy to obtain, such as the primary beam intensity and the illuminated sample volume. But the same factors also appear in the constant K_P. Because the invariant is a theoretically well-defined constant, it can be used in a quotient to cancel the unknown instrumental factors.

This is straight forward because both parameters, Q_P and K_P, are calculated from the same data set. In this way the volume-specific surface area S_V can be calculated by

Equation 29

$$S_V = 1000 \cdot \pi \cdot \frac{K_P}{Q} \cdot \varphi(1 - \varphi)$$

where φ is the volume fraction of the particles, which must be determined by independent means, such as Helium-Pycnometry (for porous solids) or concentration protocols (for dispersions and emulsions).

This method can also be applied to dense particle systems because inter-particle interferences have no effect at large angles (i.e., *S(q)* ≈ 1). The accuracy of the resulting surface-per-volume values is not very high, though. That is caused by two facts.

1. The constant K_P is determined from the final slope of ΔI(q), which is close to the background level and usually very noisy.

2. The invariant Q must be calculated by extrapolating ΔI(q) towards zero and infinitely large scattering angles, i.e., into regions where no experimental data are available. The first extrapolation can be done by applying Guinier's approximation and the second extrapolation can be done by applying Porod's q^{-4} dependence.

Modified equations apply approximately, when line-collimation experiments are used,

$$S_V = 4000 \cdot \frac{K_P}{Q} \cdot \varphi(1-\varphi)$$

Equation 30

where the Porod constant K_P is calculated by fitting $\Delta J(q) \approx K_P/q^3 + B$, and the invariant Q is the first moment of the smeared intensity,

$$Q = \int_{-\infty}^{\infty} q^2 \Delta J(q) dq$$

Equation 31

These last modified equations hold strictly only for the assumption of an infinitely long primary-beam profile (line collimation).

The volume-specific surface area Sv can be converted into the mass-specific surface area S_m, which requires knowledge of the sample density ρ_S:

Equation 32

$$S_m = \frac{S_V}{\rho_S}$$

Another method for determining the specific surface area is the "absolute-scale method," which requires the obtaining of the scattering profiles in absolute units.

Further information on determination of the specific surface area can be found in an international standard.[25]

5.4.4 Molecular weight

SAXS can also be used to determine the mean molecular weight [g/mol] of particles,[23] because the scattered intensity is proportional to the squared particle volume V_1. If we knew the density d_1 of the dispersed particles as well, then we could calculate the molecular weight from the scattered intensity. But let us first convert the ingredients of Equation 6 into a form amenable to experimenters. Equation 6 and Equation 7 can be combined:

Equation 33

$$\Delta I(q) = I_0 \cdot N \cdot V_1^2 \cdot (\Delta\rho)^2 \cdot P(q) \cdot S(q)$$

We express the total volume of illuminated particles $NV_1 = (c \cdot V_S)/d_1$ in terms of concentration c [g/cm^3], density of the particle material d_1 [cm^3/g] and illuminated sample volume V_S [cm^3]. Likewise, the particle volume $V_1 = M/(N_A \cdot d_1)$ can be converted into molar particle mass M [g/mol], where $N_A = 6.0221367 \cdot 10^{23}$/mol is Avogadro's number. Substitution renders the contrast $\Delta Z = \Delta\rho/(N_A d_1)$ in units of mol electrons per gram:

Equation 34

$$\Delta I(q) = I_0 \cdot V_S \cdot N_A \cdot c \cdot \left(\frac{\Delta\rho}{N_A \cdot d_1}\right)^2 \cdot P(q) \cdot S(q)$$

We can write the contrast as a difference of mol electrons per gram $\Delta Z = Z_1 - \overline{v}_1 \rho_2$, where Z_1 is the mol of electrons per gram particle material [mol/g], $\overline{v}_1 = 1/d^1$ is the specific volume of the particle [cm^3/g] and ρ_2 is the electron density of the solvent in [mol/cm^3]. We also have to make the equation independent of the primary-beam flux density i_0 [a.u./cm^2] and the illuminated sample volume V_S [cm^3]. The constant factors are put together into $K_0 = I_0 \cdot N_A/i_0$ [cm^2/mol], so that the intensity can finally be written in terms of concentration, contrast and molecular weight of the particles.

$$\Delta I_{abs}(q) = \frac{\Delta I_q}{I_0 \cdot V_S} = K_0 \cdot c \cdot M \cdot (\Delta Z)^2 \cdot P(q) \cdot S(q)$$

Equation 35

Note that the intensity is now in absolute units (see „Intensities on absolute scale“ on page 59).

The contrast $\Delta Z = Z_1 - \overline{v}_1 \rho_2$ must be determined independently with a density meter capable of measuring high-precision density values of solvent (d_2) and dispersion (d). Good approximations for $\overline{v}_1$ can be obtained by calculating apparent values $\overline{v_{app}} = (c - d - d_2)/(cd_2)$ from a series of concentrations c.

The electron density of the solvent ρ_2 can be calculated from the knowledge of its chemistry. If one solvent molecule of molecular weight m_2 has e_2 electrons, then its electron density is $\rho_2 = (e_2 \cdot d_2)/m_2$. The number of mol electrons per gram Z_1 can be calculated in the same way, $Z_1 = e_1/m_1$.

If the form factor and the structure factor are known, say, by fitting the data ΔI(q), then the molecular weight could be determined at any q-value using

Equation 36

$$M = \frac{\Delta I(q)}{K_0 \cdot c \cdot M \cdot (\Delta Z)^2 \cdot P(q) \cdot S(q)}$$

If a correct model for $P(q) \cdot S(q)$ cannot be found, then people try to extrapolate ΔI(q) towards zero scattering angle so that P(0) = 1. In order to apply $S(q) \approx 1$ one also extrapolates towards negligible concentration. A series of scattering curves are measured at different concentrations. These are extrapolated[27] at every q-value, as is commonly done in light scattering with a so-called Zimm plot.

5.4.5 Particle structure

Every particle produces a form factor that is characteristic to its structure. The slope of the form factor at small angles is primarily determined by the overall size and the final slope at large angles bears the information of the surface. The information about the shape and the internal density distribution lies in the oscillating part in the middle section of the form factor ("Central part" or "Fourier part," according to Porod).[55]

A rough classification into globular, cylindrical and lamellar shape (with axial ratios bigger than 5) can be quickly done by investigating the power law of the form factor at small angles (see Fig. 26). In a double logarithmic plot an initial slope of 0, -1 or -2 indicates globular, cylindrical or lamellar shape, respectively. If the slope is steeper than that (e.g., -3 or -4) then the particles are larger than the resolution limit and the Porod region is the only part of the form factor that can be observed.

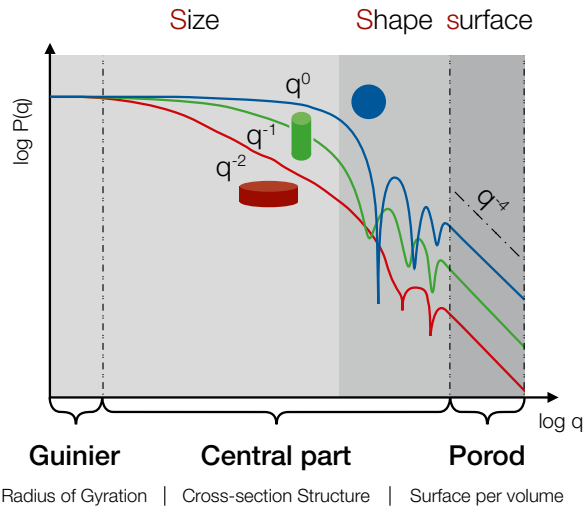

Fig. 26
The information domains of a particle form factor.

The oscillating "Central part" or "Fourier part" of the form factor can be profitably investigated by transforming it into "real space," i.e., the calculation of p(r) from an experimental *P(q)* via

$$P(q) = 4\pi \int_{-\infty}^{\infty} p(r) \sin \frac{\sin(qr)}{r} dr$$

Equation 37

The applied method is basically a Fourier-transformation and the resulting curve, p(r), is a so-called "pair-distance distribution function" (PDDF). This is a histogram of distances which can be found inside the particle. Details of how these PDDFs are calculated can be found in the original literature.[22]. It is not within the scope of this document to present these details. Instead, let us discuss the features of a PDDF which give indications about the particle structure.

The shape of a particle can be quickly classified into spherical (or globular), prolate (or cylindrical) and oblate (or lamellar) symmetry by identifying some key features in the PDDF as shown in Fig. 27.

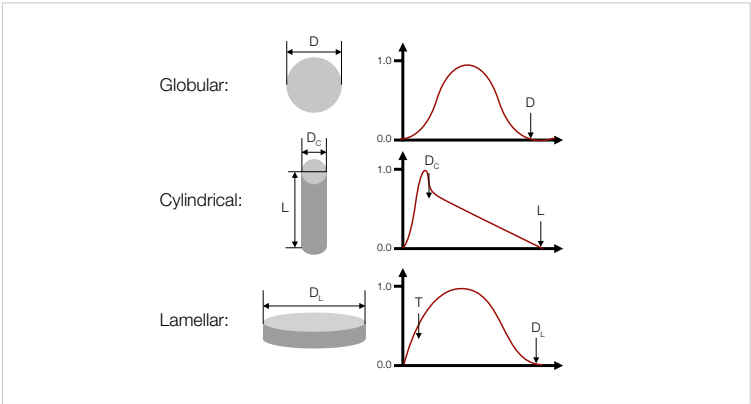

Fig. 27
The key features of the PDDF, which are indicative for the particle shape.

Globular particles can be identified from the bell shaped, almost symmetrical peak. Cylinder particles are identified by a small overshoot and a linear tail in the PDDF. The PDDFs of lamellar particles are not bell shaped at small r-values. They have a resemblance to the globular PDDF, but the curvature at small r-values is different (see Fig. 27). All PDDFs decay to zero at some distance r, which indicates the largest distance that can be found inside the particle.

Inhomogeneous (or core-shell) particles are also quickly discovered because the PDDF is a histogram of distances which is weighted by the contrast values ($\Delta\rho$) that are connected by each distance. So, all distances that cross the border from positive to negative $\Delta\rho$-values count negative. This causes a dip in the PDDF, which can even go to negative (see Fig. 28), when the contrast of one region is smaller than that of the matrix material. The contrast of the matrix material counts zero and all distances which connect matrix material with particle material do not count at all.

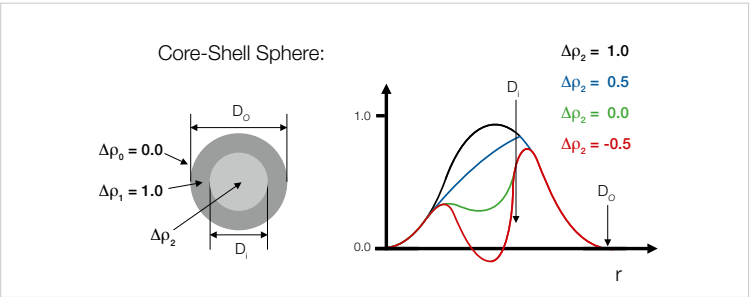

Fig. 28
The PDDFs of core-shell particles.

It is comparatively easy to recognize the PDDFs of aggregates, i.e., of particles that stick together. They show a second peak, too. But in contrast to the second peak in the PDDF of a core-shell particle, it is smaller than the first peak (see Fig. 29).

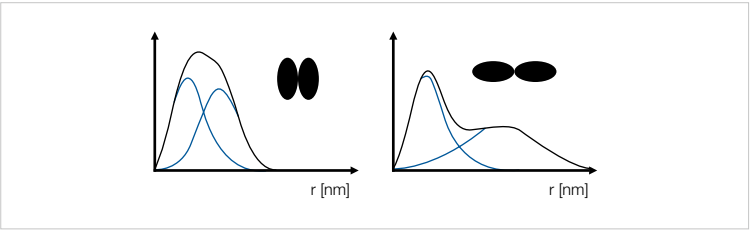

Fig. 29
The aggregate of two subunits make a PDDF which can be recognized by a second peak.

Particles of arbitrary shape produce PDDFs that cannot be analyzed without additional information. In general, it must be noted that any PDDF, as well as the scattering function is ambiguous, when polydispersity or polymorphism are taking part. Any shape can be generated by a "smart-enough" distribution of polydisperse spheres or other shapes. So, microscopic techniques should always be used to complement the proof of structure.

When particles are centro-symmetric (i.e., spherical, cylindrical or lamellar), then their PDDFs can be transformed (deconvoluted)[28],[29] into the corresponding radial density profiles. For all other particle symmetries, model calculations[30]-[34] must be performed and compared to the experimental PDDF (or form factor) in order to refine a structure model. This can also be attempted directly by means

of fitting routines[32]-[34] which can cope with the challenges of local minima in the search for the best-fitting structure.

5.4.6 Polydispersity analysis

The particle shape concluded from SAXS experiments is always ambiguous if no additional information about the sample is available from some other technique, such as electron microscopy. The ambiguity lies in the fact that the shape of a PDDF (as well as the shape of a form factor) is the average of ALL illuminated particles in the sample. And these can be many! The PDDF is therefore the sum of contributions from

1. identical particles (in **monodisperse** samples),

2. particles of the same general shape but different size (in **polydisperse** samples), or

3. particles of totally different shapes and sizes (in **polymorphous** samples).

Extracting the single components from the experimental form factor or the PDDF is known as polydispersity analysis. It can be done with the same basic concept shown previously in the synthesis (see Fig. 12). It is important to know, however, that it is possible to split up the experimental PDDF (or form factor) into a unanimous distribution of sizes, only when the shape of the particles is established.

If a sample contains two different but known shapes, then the relative volume fractions of the two particle species can be quantitatively determined by calculating the best fitting coefficients (a and b) of the following equation,

Equation 38

$$P_{Sample} = a^2 \cdot P_{Shape\,1} + b^2 \cdot P_{Shape\,2}$$

where $P_{Shape\ 1}$ and $P_{Shape\ 2}$ are the theoretical PDDFs or form factors of the respective shape or size component. The parameters a and b are the respective volume fractions of each component.

Once the shape is established, the size distribution of one parameter, such as the particle radius, can be calculated by an inversion of

$$P_{exp}(q) = \int_{-\infty}^{\infty} D_I(R) P(q,R) dr$$

Equation 39

P(q, R) is the theoretical form factor of the assumed shape and D_1 is the intensity-weighted size distribution. Volume and number distributions can also be obtained by using $D_V = D_I/V_1$ and $D_N = D_I/V_1^2$, respectively. Once the size distribution is calculated, the mean particle size $\langle R \rangle_I$ and the mean distribution width $\sigma_I(R)$ can be calculated therefrom,

$$\langle R \rangle_I = \int_{-\infty}^{\infty} R D_I(R) dr \qquad \sigma_I(R) = \sqrt{\langle R^2 \rangle_I - \langle R \rangle_I^2}$$

Equation 40
Equation 41

For volume and number weighted averages, the corresponding distributions must be used instead of D_I. Here we take it that the distributions are all normalized to unit area.

The determination of the particle size and size distribution by small-angle X-ray scattering is also addressed in an international standard.[35]

5.4.7 Particle number concentration

Small-angle X-ray scattering (SAXS) can be applied for the measurement of the concentration of nanoparticles in liquids.[36] This approach requires sufficiently monodisperse particles and dilute nanoparticle dispersions, i.e., that particle-particle interactions are absent. It is based on calculating the differential scattering

cross-section per volume $\frac{d\Sigma}{d\Omega}(q)$ by using different parameters measured in the SAXS experiment: the scattered intensity I(q), the sample transmission T, the solid angle ΔΩ and the sample thickness t_S.

Equation 42

$$\frac{d\Sigma}{d\Omega}(q) = \frac{I(q)}{I_{in} \cdot T \cdot \Delta\Omega \cdot \eta_{QE} \cdot w}$$

The mean particle diameter d_{num} and the standard deviation – both are part of the number-weighted size distribution $g_{num}(r)$ – and the particle number concentration C can then be obtained from fitting the below equation to the measured scattering data.

Equation 43

$$\frac{I(q)}{I_{in} \cdot T \cdot \Delta\Omega \cdot \eta_{QE} \cdot w} = r_e^2 \cdot C \cdot \Delta\rho_e^2 \int_{-\infty}^{\infty} g_{num}(r) \cdot |P(q,r)|^2 dr$$

5.4.8 Model calculations

When the structure of a particle is known to consist of a couple of known subunits, then model calculations are needed to determine the relative positions and orientations of the subunits. The determination consists of repeated calculations of theoretical PDDFs (or form factors). Comparisons with the experimental curves then help to decide which changes are needed to improve the fit. The subunit configuration that fits best is taken as the refined structure model.

Of course, structure refinements only make sense when it is established that the experimental PDDFs or form factors are from monodisperse samples. The presence of any diversity in size or shape is detrimental to a structure determination.

Computer programs that can be used to model form factors and PDDFs are abundant and available.[30]-[34]

5.4.9 Particle interaction

When determining the single-particle structure, most of the time the structure factor *S(q)* cannot be neglected. For this you would have to dilute your sample and this is not always practicable because

1. A minimum concentration is required to get sufficient particle scattering above the background level (particularly with low-contrast samples such as proteins in solution).

2. The particle structure can change with the concentration (e.g., surfactants in solution) and this fact might even be the reason for the investigation.

Interparticle forces are responsible for the development of a structure factor. The interaction strength depends on the concentration of the particles and on the force they exert on each other. Known force classes or interaction types are briefly listed here.

1. **Hard-sphere interaction:** The particles can move freely but cannot penetrate each other. It is described by a hard-sphere radius and a concentration.

2. **Coulomb interaction:** Particles that carry electrical charges can move freely unless their electrical fields start to penetrate and repel each other. It is described by an effective hard-sphere radius, a concentration, a surface charge and an ionic strength of the solvent (which leads to a layer of counter ions that shield off the electrical fields of neighboring particles).

3. **Van-der-Waals interaction:** Refers to those forces which arise from the polarization of molecules into dipoles. It is a property that all molecules have. Condensation and aggregation of particles are caused by it, because it makes particles attract each other, once they have reached a minimum distance. The parameters are an effective hard-sphere radius, a concentration and two exponents that describe a short-ranged attraction and a

long-ranged repelling distance. The two exponents inherently form a potential minimum which defines an equilibrium inter-particle distance. The deeper the potential minimum, the more stable the inter-particle distance.

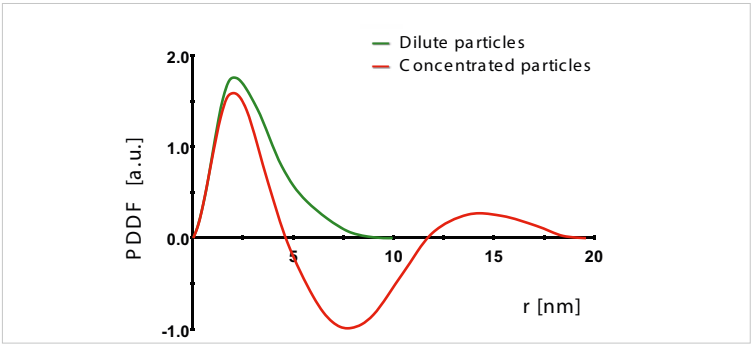

Fig. 30
The PDDF of (red) a concentrated particle system shows a negative part with a minimum approximately at the largest dimension of the particle (D = 10 nm). Due to a shell of next-neighboring particles a second peak appears around r = 14 nm. The same particle system, but diluted, gives the green PDDF.

The first indication of interparticle interference is when the scattering curve bends down at small q-values (see Fig. 8). The corresponding PDDF goes negative and shows a second maximum at larger distances (see Fig. 30). The negative dip originates from the excluded volume caused by the presence of one particle which prevents other particles from entering the same volume (hard-sphere effect). The electron density in the excluded volume is therefore smaller than the bulk electron density (which is the zero line in the PDDF).

The second peak at larger distances is caused by a “shell” of next neighbors, which increases the density above the bulk level due to the locally increased particle concentration. This alternating arrangement of particle densities is commonly known as short-range order and is typical for the liquid-phase state.

At larger concentrations or stronger interaction forces the particles

can rearrange into a long-range order, i.e., they develop a crystallinity, which is typical for a solid-phase state. In this case the PDDF oscillates up to large r-values with a periodicity of the unit-cell dimension. The corresponding scattering curve then shows Bragg peaks for every periodic component in the PDDF. The spacing of the peaks relative to each other tells something about the symmetry of the crystal system. The relative peak intensities reflect the form factor of the unit cell's ingredients because of the product of structure and form factor (see Fig. 31).

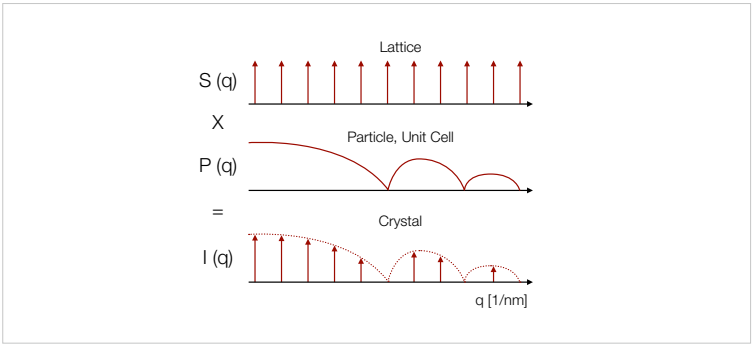

Fig. 31
The scattering curve of a crystal I(q) is the product of the structure (or lattice) factor S(q) with the form factor P(q) of the particles (or atoms) in the unit cell. When lattice peak and form-factor minimum collide, then a so-called systematic extinction follows and the peak cannot be observed.

Other factors that influence the peak intensities are

1. the degree of order of the "particles," which leads to a decay of peak intensities with increasing scattering angle (the better the order, the smaller the decay and the more peaks can be observed at large angles) and
2. the spatial extent of a crystalline domain, which is reflected in the peak width (the larger the domain, the smaller the peak width).

In many practical applications it is desirable to eliminate the structure factor which obstructs the access to the single-particle structure. The old-fashioned way was to cut away data points at very small angles and interpret the particle structure from the scattering profile at larger angles. A much better method[37] is to fit a

theoretical *S(q)* simultaneously with the PDDF. In this way the interparticle terms are taken into account by fitting an effective *S(q)* and the single-particle terms are represented by the PDDF with only little disturbances from the *S(q)*. In addition, the fitted *S(q)*-parameters can be used to retrieve interparticle parameters.

5.4.10 Degree of orientation

Particles of non-spherical shapes can have a preferred orientation due to applied shear or strain. The azimuthal profiles of randomly oriented samples (or with spherical particles) have a constant intensity along a circular path centered at the primary beam position. As soon as some preferred orientation is introduced into the sample (e.g. in block co-polymer melts) the intensity profile starts to oscillate or becomes peaked at certain azimuth angles. It is clear that the amplitudes of these oscillations are useful to quantify the degree of orientation. Also the angle of preferred orientation is of interest. There are two approaches commonly in use.

1. **Herman's orientation parameter** P_2 is a frequently used parameter to define the angle of orientation. It is defined by

Equation 44

$$P_2 = \frac{3\langle\cos^2\phi\rangle - 1}{2}$$

where $\langle\cos^2\phi\rangle = \left(\int_0^{\pi} \cos^2\phi \cdot \Delta I(\phi) \cdot \sin\phi d\phi\right) / \left(\int_0^{\pi} \Delta I(\phi) \cdot \sin\phi d\phi\right)$

If $P_2 = 1$, then the intensity is perfectly peaked towards $\phi = 0°$, if $P_2 = -1/2$, then it is perfectly peaked towards $\phi = 90°$ (antiparallel). Confusion arises though when $P_2 = 0$. Because this can mean that the intensity profile is either a constant (no orientation at all) or perfectly peaked towards the "magic angle" of $\phi = 54.7356°$. This mix-up between degree and angle of orientation makes this parameter practically useless for SAXS applications.

2. **Cinader & Burghardt**[38] proposed to characterize anisotropy in SAXS patterns by an anisotropy tensor

$$S = \begin{bmatrix} S_{11} & S_{12} \\ S_{12} & S_{22} \end{bmatrix} = \begin{bmatrix} \cos^2\phi & \cos\phi\sin\phi \\ \cos\phi\sin\phi & \cos^2\phi \end{bmatrix}$$

where $\langle z\rangle = \left(\int_0^{\pi} z \cdot \Delta I(\phi)d\phi\right) / \left(\int_0^{\pi} \Delta I(\phi)d\phi\right)$

Equation 45

ϕ increases anti-clockwise, starting from 3 o'clock.

The degree of orientation is then defined by $\Delta S = \sqrt{(S_{11} - S_{22})^2 + 4S_{12}^2}$

and the mean orientation angle is calculated by $\chi = \frac{1}{2}\mathrm{atan}[\frac{2S_{12}}{S_{11} - S22}]$

Possible values of ΔS lie between 0 (no orientation) and 1 (perfect orientation) and there is no ambiguity as in the case of Herman's orientation parameter.

It is also worth mentioning that Cinader & Burghardt's approach, as shown above, is sensitive towards a two-fold symmetry (C2). For example, a clover-leaf shaped intensity pattern, having a four-fold symmetry (C4), will give a zero degree of orientation (ΔS = 0), because it is not a two-fold symmetry. But the algorithm is easily extended to a 2n-fold symmetry by substituting cosϕ and sinϕ by cos(nϕ) and sin(nϕ), respectively. In the case of a clover-leaf pattern n would be 2.

5.4.11 Degree of crystallinity

The degree of crystallinity (DOC) is used to characterize materials which can exist in both modifications, amorphous (DOC = 0) and crystalline (DOC = 1). It tells us how much of the sample volume is in the crystalline state. It is, however, a relative measure because it can only be determined if an amorphous reference sample is available. Please note, that amorphous not necessarily means "no crystallinity at all," but rather that it contains either no crystallinity or the

"wrong" crystallinity. Thus, also the amorphous reference sample can have Bragg reflections in its scattering curve.

The DOC is determined by making two scattering experiments. One is the acquisition of the reference sample [$\Delta I_{amorphous}(q)$] and the other one acquires intensities of the sample under investigation [$\Delta I_{sample}(q)$]. The DOC is then calculated via

Equation 46

$$DOC = \left(\int_{q_{min}}^{q_{max}} q^2 \left[\Delta I_{Sample}(q) - \Delta I_{amorphous}(q)\right] dq\right) / \left(\int_{q_{min}}^{q_{max}} q^2 \Delta I_{Sample}(q) dq\right)$$

The background must be carefully subtracted before the DOC is calculated because any residual baseline will make the integrands rise quickly due to the multiplication with q^2.

If an amorphous sample is not available, then an assumed smooth background curve must be used, which makes the results less accurate. One good way of determining the background curve was devised by Steenstrup.[39]

Finally, we have to mention that the determination of a DOC is a common quest in XRD (WAXS) but it is a relatively rare sought-after value in SAXS applications due to the enhanced difficulty of determining the background.

➤ 5.5. Data interpretation in reflection mode

Data from surface-scattering experiments need special treatment and interpretation. This also requires that we have to reconsider the previously simplified definition of the momentum transfer.

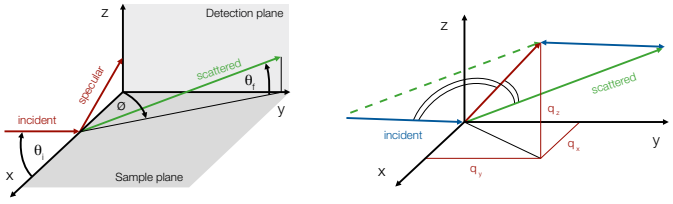

Fig. 32
Every point in the detection plane can be attributed to a scattering vector, which is the difference of the two directions: scattered minus incident direction.

If we define the scattering geometry as shown in Fig. 32, then the scattering vector is defined by

$$\vec{q} = \begin{bmatrix} q_x \\ q_y \\ q_z \end{bmatrix} = \frac{2\pi}{\lambda} \begin{bmatrix} \cos\theta_f \cos\phi - \cos\theta_i \\ \cos\theta_f \sin\phi \\ \sin\theta_f + \sin\theta_i \end{bmatrix}$$

Equation 47

Until now we were confronted with the z-component (q_z) only and we have called it q for short. In XRR experiments the detection angle is strictly the same as the angle of incidence ($\theta_f = \theta_i$ and $s = \phi$). It follows that $q_z = q$ and $q_x = q_y = 0$. In GISAXS experiments scans along q_y and q_z are extensively used. See 6.2 for a more detailed discussion of GISAXS experiments.

➤ 5.6. Summary

In conclusion, we can summarize the parameters that affect the scattered intensity and influence the SAXS-signal quality.

1. **Size:** The intensity of the scattering signal goes with the sixth power of the particle size. The larger the particles are, the more intensity will be detected from them. However, there is an upper limit to this statement. Particles which are bigger than the spatial resolution limit of the setup (see „The resolution“ on page 61) will scatter to inaccessibly small angles and, thus, become invisible. But, generally, large particles will overshadow the signal of the smaller ones.

2. **Volume:** The sample volume increases the intensity linearly. Twice the illuminated sample volume will give twice the intensity and √2-times the signal quality. Care must be taken that the sample volume is maximized without exceeding the optimum sample thickness (see „Absorption“ on page 15).

3. **Contrast:** The electron-density difference between particles and matrix material (e.g., the solvent) increases the intensity quadratically (see „Contrast“ on page 52). Given the choice, one should always opt for a low-density solvent to maximize the contrast of the dispersed particles. On the other hand, one can make bothersome particles invisible by matching their contrast and facilitate the analysis of mixtures.

4. **Sample-to-detector distance:** Because the sample scatters into all directions, the scattered intensity is diluted over the surface of an ever increasing sphere, the surface of which increases with the squared radius R. Thus, short instruments (with small sample-to-detector distance R) have a higher efficiency than long instruments. The objection that longer instruments have a higher resolution is not always true because the divergences of beam and optics determine the resolution. These do not improve if only the sample-to-detector distance is increased.

5. **Resolution:** Whenever the divergence of the beam is reduced to resolve large particles, the intensity of the setup suffers. USAXS instruments (e.g., Bonse-Hart systems) with really a whopping resolution in the micrometer range use crystal optics to reduce the divergence so much that even the primary beam can no longer harm the detector. It is clear that the samples then must have sufficient contrast and size to produce a scattered intensity comparable to the primary-beam intensity. Otherwise there will not be enough photons reaching the detector.

6. **Collimation:** Every collimation has its function. The function of point collimation is to resolve orientation effects not to improve the signal quality or resolution. Similarly, the function of line collimation is to improve signal quality and resolution, not to investigate orientation effects.

6. Scientific applications

➤ 6.1. SAXS for structural biology

by Jill Trewhella, The University of Sydney, and
Tobias Madl, Medical University of Graz

Introduction

In the last decade, SAXS studies of biological macromolecules and the complexes or assemblies they form have gained tremendously in popularity. This increase has been driven in part by structural biologists undertaking increasingly challenging systems along with the substantial developments in and increased availability of both lab-based and synchrotron-based instrumentation.[40]-[42] At the same time, there have been significant developments in data interpretation and structural modeling tools.[43] SAXS provides detailed insights into the structures and conformations of biological molecules and can probe a wide range of dimensions, as well as biomolecular dynamics. It therefore is not surprising that the recent developments have stimulated applications of SAXS to a wide range of basic and applied studies of biological materials, especially in structural molecular biology.

SAXS is increasingly used routinely in combination with X-ray crystallography and Nuclear Magnetic Resonance (NMR) spectroscopy, and more recently with cryo-electron microscopy (EM), for structural modeling using hybrid data sets,[44] providing information which is complementary to the traditionally more mainstream structural biology techniques. With SAXS, the structure and dynamics of a biomolecule are probed in solution where key physiological parameters such as ionic strength, pH, and temperature can be tuned and tested, and the effects of ligand binding or complex formation assessed. Proteins, polynucleotides (DNA and RNA), their biomolecular complexes, and lipid assemblies all can be studied.

An excellent and comprehensive text has recently been published covering all aspects of small-angle X-ray and neutron scattering on biological molecules in solution in depth,[45] and there are a number of excellent reviews.[46]-[48] Note that scattering profiles of biological macromolecules are now collected in the Small Angle Scattering Biological Data Bank (SASPDB), a searchable curated repository of experimental SAXS and SANS data.[50] Here we will present a brief summary of the important foundations for SAXS and structural biology and the nature of the structural information obtained. The following sections will provide context and illustrative examples of SAXS studies of the major biological polymers, polynucleotides (DNA and RNA) and polypeptides (proteins), and the assemblies they form in their functional units.

6.1.1 Some basics about biomolecular SAXS and structure analysis

The SAXS signal from a biomolecule in solution arises from the elastic, coherent scattering of X-rays by its electrons, and represents the time and ensemble average of all structures present. As such, it is generally isotropic due to the random orientations of the particles in solution. The information derived from the molecules having a fixed orientation within a crystal lattice that facilitates three-dimensional (3D) structure solution with crystallography is lost. Only information on the distribution of distances between scattering centers (the electron cloud of each atom) is preserved. The isotropic scattering pattern reduces to a one-dimensional intensity profile that depends only on the scattering angle with respect to the direct beam, usually expressed as $I(q)$ where $q = \frac{4\pi sin\theta}{\lambda}$, 2θ is the scattering angle, and λ the wavelength of the scattered X-rays. This profile can provide accurate and precise structural parameters for a solution of non-interacting biological macromolecules that are essentially identical at the resolution of the measurement; including molecular mass *(M)* or volume *(V),* radius of gyration R_g, and overall shape and dimensions often expressed in the form of the probable distribution of distances between scattering centers as

P(r) vs *r*. In the case of a heterogeneous mixture, e.g., where flexibility results in conformational variability or there is polydispersity, the SAXS data and associated structural parameters represent the population weighted average.

The limits on the dimensions that can be probed in the SAXS experiment are determined by the measured *q*-range, which has a reciprocal relationship with the real space dimensions. The upper dimension limit is thus determined by the minimum reliably measured q, q_{min}. For a maximum dimension of d_{max}, it is generally agreed that q_{min} must be at least $\frac{\pi}{d_{max}}$, and data below this limit are essential to demonstrate that no larger particles are present. The maximum *q*-requirement is to be sufficiently beyond the *q*-value where the scattered intensity is flat, as this is where the essential shape information encoded in the intensity profile ends. SAXS instruments can be configured to achieve q_{min} values as small as 0.001 Å^{-1} to 0.003 Å^{-1} and q_{max} values as large as 0.5 Å^{-1} to 0.7 Å^{-1}. Most 20 kDa to 150 kDa biomolecules (50 Å to 250 Å) are readily accessible for accurate SAXS analysis with a measured *q*-range of ~0.005 Å^{-1} to 0.35 Å^{-1}, but it is possible to study much smaller or larger particles (10 A to 1000 A) by setting up the needed instrument configuration.

The scattered intensity from a biomolecular particle in solution can be simply expressed as:

Equation 48

$$I(q) = N \cdot (\Delta\rho V)^2 \cdot P(q) \cdot S(q)$$

where N is the number of particles per unit volume; $\Delta\rho$ is the scattering density difference with respect to solvent (or "contrast"), and V is the volume of each particle; $P(q)$ is the "form factor" that encodes the structural information on the particles; and $S(q)$, the "structure factor" that encodes correlation distances between particles. For an ideal solution of non-interacting particles $S(q) = 1$.

From Equation 48, it is evident that the scattered intensity from the

biomolecule is proportional to the square of its contrast. Zero contrast means the biomolecule will be essentially invisible in the scattering experiment; in other words, it appears to be the same as the solvent and contributes only a flat, incoherent background scattering. Equation 48 also speaks to the stringent requirements on samples for SAXS if accurate structural analysis is the goal. As *I(q)* is proportional to the square of the particle volume, high molecular weight contaminants and small amounts of non-specific aggregation will contribute to the scattering so that structural parameters will be systematically larger than the particle of interest. Inter-particle distance correlations due to charge repulsion give rise to a non-unity *S(q)* that suppresses the lowest-angle scattering data and makes the structural parameters smaller than the particle of interest. Nevertheless, with care taken in sample preparation and data evaluation,[46], [49] the lack of a need for crystals, the ability to probe structures in solution at much lower concentrations compared to NMR, and at physiological temperatures means that the SAXS experiment can provide complementary structural information that is important to the structural biologist. The fact that SAXS requires only very small amounts of sample — a few to tens of microliters of sub-milligram to a few milligrams per milliliter depending on the molecular mass (or *V*) and $\Delta\rho$ for the particle of interest — adds to the attraction of the technique.

The SAXS sample is typically exposed to a monochromatic beam of X-rays with wavelengths in the range of 1 Å to 3 Å, and the resulting scattering pattern is observed at small angles (up to 10° from the primary beam). Data acquisition is carried out within seconds to minutes for synchrotron sources, or in minutes to hours for in-house, laboratory-based X-ray sources. One of the challenges for structural analysis using SAXS is that biomolecules are relatively weak scatterers of X-rays and samples must be measured in the dilute solution regime. High-intensity X-ray sources therefore provide a great advantage, providing the damage arising from free radicals generated by the X-rays can be sufficiently controlled, e.g., by using free-radical quenching agents added to the solvent and/or by flowing the sample through the X-ray beam. For lab-based systems, the use of a line source to expose a larger sample volume,

pioneered by Otto Kratky, made it practical to study proteins with a simple sealed tube X-ray source. This Kratky-style beam geometry has been further optimized in modern lab-based instrumentation and applications.[51] The line beam geometry results in a smearing of the data that has to be taken into account in data treatment and analysis. The high speed of data acquisition with synchrotron intensities has made time-resolved studies of dynamic systems and also high throughput screening experiments possible.[52] The brightness of modern synchrotron beams also have made it practical to do a last step in-line purification with SEC-SAXS opening up many systems for study that were previously impossible to study due to time-dependent aggregation.[53], [54]

The SAXS signal from a biomolecule in solution falls off rapidly as a function of angle, dropping several orders of magnitude to a flat and very weak background signal arising from internal density fluctuations within the scattering particle and its solvent. As noted above, the size and shape information in this SAXS profile is encoded in the *q*-region prior to the flat background. Accurate structural analysis requires very accurate and precise subtraction of the solvent scattering. A solvent blank measurement with the identical configuration immediately prior to or after the sample measurement is required from a precisely matched solvent (e.g., from a last step dialysis or column flow-through from a last step purification by chromatography). Precise scaling of the biomolecule plus solvent and solvent measurements to constant X-ray counts on sample is also required. For well-folded uniform density scattering particles, one can apply a correction in the solvent subtraction step using the Porod approximation.[55] A better strategy, of course, is to ensure accurately scaled and matched sample and solvent measurements because if there is significant flexibility present in the molecule of interest, this information is compromised by applying such a correction.

Given the preponderance of flexibility and even large regions of intrinsic disorder that can be present in biomolecules, the capacity to probe flexibility in biomolecules using SAXS is of increasing

interest. It is the high-q region of the SAXS profile that can provide evidence of this flexibility. A well-folded, uniform density compact structure with a defined boundary will approach zero with a q^{-4} dependence (the Porod approximation), but a q^{-2} dependence will be observed for an unfolded structure in a random coil configuration. For partially flexible structures, the behavior will be intermediate. There are various plots that aid in interpretation of scattering data in terms of relative flexibility (e.g., Kratky or dimensionless Kratky plots). A recent summary of these analyses is available in.[56]

Fig. 33 provides an illustrative example of SAXS data and some of the kinds of analyses possible for the protein bovine serum albumin (BSA) whose crystal structure is known (Fig. 33 A).[57] The log-log plot of the scattering from BSA (Fig. 33 B) shows the zero slope at low q expected for a monodisperse solution. Further, the Guinier plot ($\ln I(q)$ vs q^2, Fig. 33 B inset) is linear. Guinier showed that this plot has a slope equal to $R_g/3$ in the small-angle limit where $qR_g < 1.3$. The probable frequency distribution of inter-atomic distances (Fig. 33 C), calculated as the inverse Fourier transform of $I(q)$ vs q, has a bell-shaped profile consistent with the globular BSA structure that goes to zero at the r-value corresponding with the maximum dimension of the structure. The dimensionless Kratky plot (Fig. 33 D) also has the bell-shaped curve expected for a mostly well-folded protein, with a maximum of about 1.1 at around $qR_g = 1.75$.

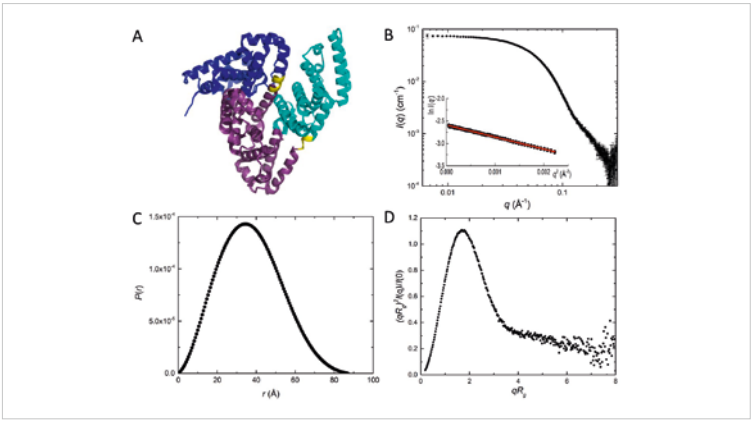

Fig. 33
Scattering experiment on solutions of bovine serum albumin (BSA). ***A.*** *Cartoon representation of the crystal structure of BSA (protein data bank entry 4F5S, chain A) highlighting the three tightly networked domains (blue, violet, cyan) and amino acids identified as having high thermal parameters and potentially being responsible for domain movements.* ***B.*** *Log-log plot of I(q) vs q with a Guinier plot inset.* ***C.*** *P(r) vs r from the data in A.* ***D.*** *The dimensionless Kratky plot ($\frac{(qR_g)^2 I(q)}{I(0)}$ vs qR_g) shows the expected bell shaped curve, with a maximum of ~1.1 near ~1.75, with a small upturn ay high qRg consistent with some limited flexibility present. These data were acquired using the SAXS/WAXS instrument at the Australian synchrotron.*[58]

Excellent recent guides for the successful preparation of SAXS experiments are available,[49], [59] as well as for the accurate interpretation[46] and adequate reporting[60] of SAXS experiments.

Structural modeling with SAXS

In addition to determining size and shape parameters, detailed 3D structural modeling can provide important insights relating to biomolecular function.[43] Because the SAXS profile can be predicted from atomic coordinates[61], [62] it can be used to evaluate high-resolution structures in various solution conditions and identify differences with respect to, say, a crystal form or different solution states, including the effects of ligand binding. Further, rigid body modeling against SAXS data can be used to determine the dispositions of domains or subunits of known structure (from crystallography or NMR) (e.g., using programs within the ATSAS suite.[63] The conformational space that must be sampled in such modeling

can be significantly reduced by utilizing additional restraints from experiments (e.g., close contacts from chemical crosslinking and mass spectrometry, EPR, sequence covariance) and known chemical stereochemistry.

In the case of biomolecules with flexible hinges or linkers, one can use known domain or subunit structures and any additional restraints from complementary studies to perform multi-state or ensemble modeling that provides insights into the structures present in the conformationally heterogeneous ensemble.[64], [65] Because of the large number of degrees of freedom in an ensemble model, this kind of modeling is the most vulnerable to over-fitting and over-interpretation and thus benefits greatly from robust restraints. Another example of a heterogeneous solution that can be analyzed successfully is a mixture of a small number of distinct multimers or a monomer-multimer mixture. For these systems it may be possible to determine the proportion of species present and in some cases even to extract the scattering profiles of the contributing species.
There are an increasing number of publicly available software packages for biomolecular structural modeling that can yield *ab initio*, 3D bead models that are inherently low-resolution, atomistic models from rigid body refinement, and ensemble modeling where there is inherent flexibility. One of the most comprehensive scattering data processing, analysis, and modeling packages is the ATSAS package[63] (online version at https://www.embl-hamburg.de/biosaxs/atsas-online/), but there are also other important innovations and alternative approaches, such as in the ScÅtter analysis package (available for download at http://www.bioisis.net/tutorial), and atomistic modeling routines FoXS, Multi-FoXS, AllosMod-FoXS, FoXS-DOCK[64] (online versions at https://salilab.org/). It is therefore advisable to explore the different available options as structural modeling using SAXS data, including prediction of scattering profiles from atomic coordinates, is a subject of ongoing research. This research is particularly relevant for integrated or hybrid structural modeling where SAXS data are combined with data from complementary techniques, e.g., for improved solution structure determination from NMR[66] and for challenging complexes and assemblies.[44]

An example of model-fitting to SAXS data based on the known crystal structure of BSA with putative flexibility that facilitates domain movements (see Fig. 33 A) is shown in Fig. 34. By allowing for the flexibility indicated by the dimensionless Kratky plot (Fig. 33. D) and the thermal parameters of the crystal structure,[57] the model fit substantially improves as measured by the error-weighted residual for the N points of the experimental (exp) and modeled (mod) scattering profiles $x^2 = \frac{1}{N-1} \sum_{i=1}^{N} \left(\frac{I_{exp}(q_i) - I_{mod} - I_{mod}(q_i)}{\sigma(qi)} \right)^2$, which drops from 4.4 to 0.8. The improvement is most evident in the point-by-point error-weighted difference plot in the mid-q region (q ~ 0.06 Å^{-1} to 0.15 Å^{-1}) that is most sensitive to domain movements.

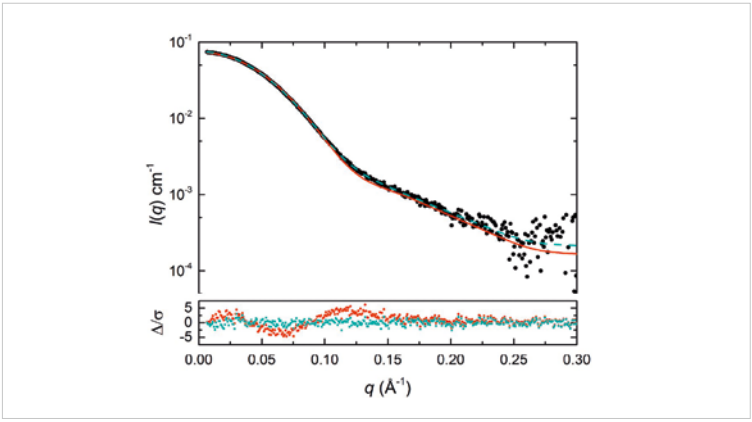

Fig. 34
Log-linear plot of I(q) vs q of the data in Fig. 33 B, with model fits corresponding to the unmodified crystal structure shown in Fig. 33 A (solid red line, modeled using FoXS) and a multistate model (dashed cyan line, a 3-state model from Multi-FoXS) that allows flexibility in the residues identified in the crystal structure as being potentially responsible for domain movements. The lower plot shows the error weighted difference as $\frac{I_{exp}(q) - I_{mod}(q)}{\sigma(q)}$.

6.1.2 The polynucleotides: DNA and RNA

The DNA polymer is formed from just four deoxyribonucleic acids whose order in the polymer chain codes for all the proteins required for life's processes. The RNA polymer is composed of ribonucleic acids. RNAs are essential to the processes that transcribe the DNA code, initially in the form of messenger RNA, and synthesize the proteins. The DNA thus serves as a as a kind of "memory" for cells

and organisms: encoding the information required for the transmission and expression of this “memory” inside and outside the cell.

SAXS is well-suited to study the structure and dynamics of DNA and RNA in solution. Their electron-rich phosphate backbone means that they have relatively high scattering density contrast with respect to water. In terms of scattering density expressed in units of electrons/Å^3, nucleic acids, proteins, and water are ~0.55 e$^-$/Å^3, ~0.42 e$^-$/Å^3, and ~0.33 e$^-$/Å^3 respectively. As scattering intensity is proportional to the contrast square, this means that the SAXS signal from a polynucleotide will be six times that for a protein of the same molecular mass (Equation 48).

DNA adopts limited possible structural forms, as might be expected for a polymer whose primary function is the storage of information; most famously the double-stranded helix that is stabilized via strong nucleic acid base-pair interactions, though single-stranded forms are also found in nature. Structural modeling of the overall shape of a DNA molecule from solution scattering data can be relatively straightforward given the limited structural forms (Fig. 35).

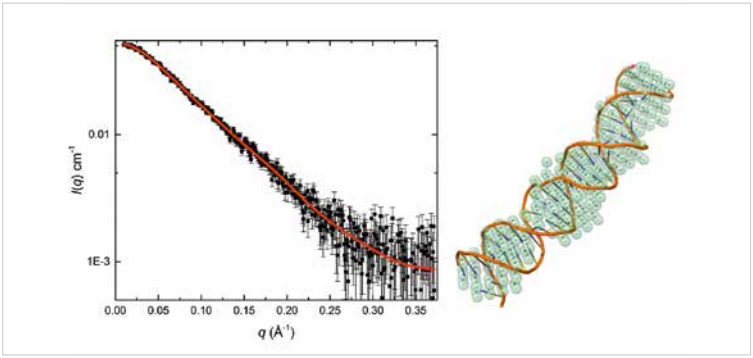

Fig. 35
A. I(q) vs q for a DNA oligomer in solution. B. Bead model reconstruction from the data in A with a cartoon representation of a segment of a double helical DNA structure that is distorted due to chemical modification (via methylation) of select bases as occurs in vivo for this sequence that recognizes a key regulatory protein. Scattering data acquired at the University of Utah using a SAXSess instrument with 10 mm line source and a Mythen strip detector.

Unlike DNA, RNA adopts a wide variety of structures as it functions as an enabler or regulator in DNA transcription, translation, splicing, and replication. Base-pair interactions stabilize the more rigid parts of RNA structures, while flexible non-base-paired regions allow for the conformational changes required for function. Besides their regulatory functions, RNAs carry out catalysis in the protein synthesizing units of a cell, the ribosomes, and the spliceosomes that selectively cut out specific regions from the messenger RNA. They can also act as sensors of environmental parameters, such as temperature or metabolite concentration. With the discovery of retro-viruses, such as HIV, the structural biology dogma of the 20th century (that is DNA makes RNA makes proteins) was turned on its head when we learned that genomic information could be stored as RNA in these viruses. The virus uses a reverse transcriptase to generate the corresponding DNA within the host cell so that the host cell machinery can translate that DNA and synthesize the viral proteins during proliferation.

Structural characterization of RNAs is challenging. X-ray crystallographic analysis of RNA structure is complicated by the difficulty of crystallizing highly charged RNA molecules. Furthermore, the low-energy states determined in X-ray crystallography have frequently been found to represent inactive conformations, rather than the active conformation present under physiological conditions. NMR spectroscopy is well-suited for structural studies of small- to medium-size RNAs, but is difficult to apply to large RNAs due to technical challenges caused by spectral overlap and extensive line broadening, the low number of observable restraints that can be used to define RNA structure.

A significant challenge for RNA studies is ensuring solutions are free of RNA-degrading enzymes. General protocols for RNA sample preparation, SAXS data acquisition, analysis and processing are available (e.g.,).[67] SAXS has been used very effectively to study RNA folding[68] and the relationship between RNA conformation and the ion environment that modulates RNA function in cells.[69] There are a growing number of structural and dynamic studies of RNA enzymes, riboswitches, aptamers, and viral RNAs,[42] one example

is illustrated in Fig. 36. Another example is the recent study of the Rev response element of HIV-1,[70] where SAXS with ab initio 3D shape reconstruction was used to characterize the unusual topological structure that enables the virus to recognize its own mRNA. The SAXS-derived structural model aided in the design of functional studies that led to solving the longstanding question of how the virus selects its own mRNA among more abundant host cellular RNAs for export.

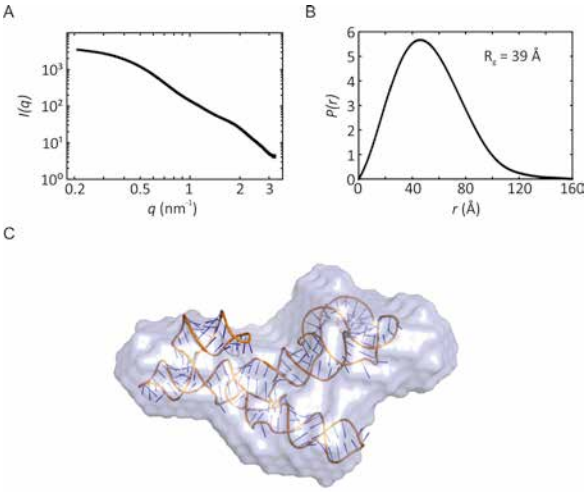

Fig. 36
I(q) vs q (A) and the corresponding P(r) vs r function (B) for the Varkud Satellite (VS) ribozyme G638A RNA dimer in solution. C. DAMMIF-based bead model reconstruction from the data in B with a cartoon representation of the ribozyme crystal structure (PDB 4R4V). SAXS data was taken from the SASDB (entry SASDAC9).

6.1.3 The polypeptides: Proteins

Proteins are the molecular "workhorses" of life's essential functions. They are involved in every molecular process within cells, including catalyzing biochemical reactions, structuring the cell, replication and transcription of DNA, motility, responses to stimuli and communication, transport of molecules, and many more. The 3-dimensional (3D) structures and dynamic properties of proteins are foundational for understanding the how life works at the molecular level.

Distortions of protein structure are often associated with human diseases. Single-point mutations, for example, can lead to structural rearrangements, protein mis-folding, and in changes in the capacity to interact with partners or in self-association behavior. These altered structural states are hallmarks of a plethora of diseases, including cancers, neurological disorders such as Alzheimer's or Parkinson's disease, heart diseases, metabolic diseases, and many others. To understand the molecular mechanisms underpinning healthy function, how these are interfered with in disease, and potentially to design novel pharmaceutical compounds to treat diseases it is essential to study the 3D structure of proteins, their interactions, and the impacts of disease-related pathological modifications.

Molecular chaperones

Molecular chaperones assist proteins to fold into the correct structures or to unfold misfolded proteins and support them in the assembly or disassembly of biological subunits. The so-called heat shock protein, Hsp90, helps other proteins fold into their correct 3D structure or to correctly refold damaged proteins. Hsp90 is implicated in a number of diseases, including neurological disorders, cancer, and cystic fibrosis. Structural studies of Hsp90 are complicated by its conformational dynamics, which inhibit crystallization. Numerous SAXS-based studies in recent years have provided insights into Hsp90's structure and dynamics that shed light

on several key aspects of Hsp90's function and regulation, including an important series of structural studies[71]-[73].

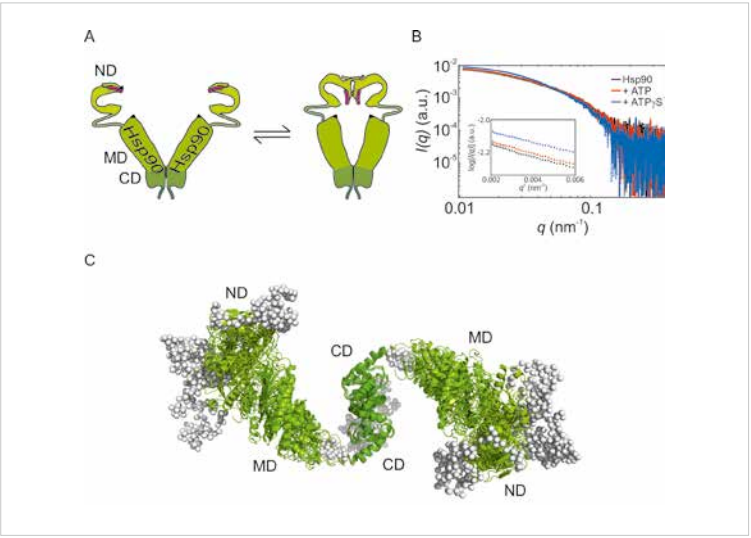

Fig. 37
A. Cartoon of the Hsp90 dimer showing the conformational changes upon binding of ATP. The 3 domains of Hsp90 are labeled (ND: N-terminal domain, MD: middle domain, CD: C-terminal domain). B. I(q) vs q for Hsp90 in the absence and presence of ATP or the non-hydrolysable nucleotide ATPγS. D. CORAL rigid body model of Hsp90. A bundle of 5 structures with the best fit to the experimental data is shown. Disordered regions were modeled with dummy atoms and are shown as spheres. Scattering data acquired at the Technical University of Munich using a SAXSess instrument with 10 mm line source and a CCD 2D detector.

Myosin-binding protein C (MyBP-C)

In muscle, thick and thin filaments made up of proteins slide past each other in response to Ca^{2+} signals (Fig. 38). Thin filaments are formed by a helical arrangement of actin monomers, while thick filaments are formed from myosin tails and have protruding lever arms with head groups that can reach across the inter-filament space to form a "cross-bridge" that provides the force for the sliding motion via a conformational change.

A number of thick and thin filament accessory proteins regulate the interactions between myosin head groups and actin, including the large modular MyBP-C.

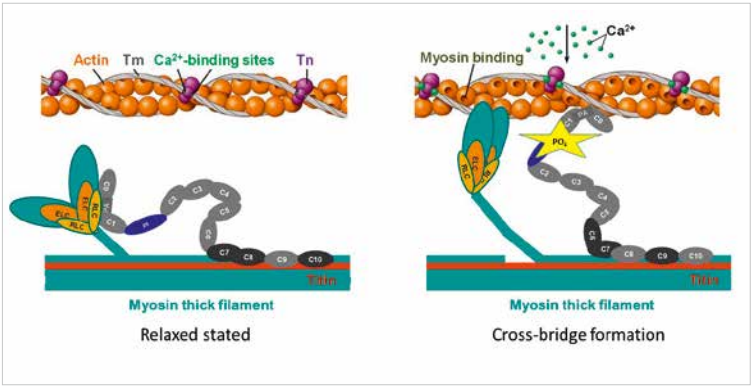

Fig. 38
Schematics showing the relaxed state for the thick and thin filaments within cardiac muscle, and the formation of cross-bridges by myosin head groups that bind to actin upon Ca^{2+} binding to the troponin (Tn) complex that sits on the actin thin filament and controls the movement of tropomyosin (Tm) that in turn controls access to the myosin-binding sites. The immunoglobulin and fibronection modules of cMyBP-C are represented as light and dark gray ellipses, with the mostly unstructured m domain in blue. The yellow and orange ellipses represent the essential and regulatory light chains that are an integral component of myosin, and the yellow star indicates phosphorylation of the m domain thought to be important in switching cMyBP-C between interactions with myosin and actin.

MyBP-C has 10 immunoglobulin or fibronectin domains (labeled as C1 through C10) and a 100-amino-acid, mostly unstructured sequence between the C1 and C2 domains, referred to as the "motif" or m-domain. The form of the protein found in cardiac muscle (the cardiac isoform cMyBP-C) has an additional C0 domain. The so-called regulatory N-terminal domains of the protein (C0 through C2) are proposed to switch between interacting with the myosin head group and actin in response to phosphorylation of the m domain during contraction. The intense interest in cMyBP-C in recent years is based on the fact that around 50 % of hypertrophic cardiomyopathies, estimated to affect as many as 1 in 200 individuals and the most common cause of fatal heart attacks in the young, are linked to mutations in cMyBP-C.

SAXS provided the first structural view of the key regulatory domains of cMyBP-C (C0 through C2).[74] As is often the case with modular proteins, the structures of individual domains are readily solved by crystallography and NMR, but longer constructs and the full length protein are resistant to crystallization and too large for NMR. SAXS has thus continued to provide unique structural insights into domain relationships and flexibility in the protein.

SAXS studies of the central domains (C5 through C7) examined the structural impacts of clinically linked mutations associated with distinct disease phenotypes, with respect to severity, stage of onset and end phase. Mutant and wild type forms were analyzed in terms of understanding the key structural features of these domains essential for healthy function and the role they may play in disease development.[75]

An extensive study of N-terminal domain constructs of increasing length revealed a highly extended yet distinctively "bent" modular arrangement that is similar to the giant elastic muscle protein titin that is associated with the thick filaments.[76] The *P(r)* profiles in Fig. 39 show the expected increases in the maximum dimension as modules are added in an extended configuration giving rise to multiple peaks. For example, the two domain C3C4 construct gives a *P(r)* with two peaks (lower *P(r)* plot). The first peak arises from interatomic distances within each of the individual domains, and the second peak, approximately half the height of the first, arises from interatomic distances between two domains in an extended configuration. Longer constructs extend to large *r*-values and have more peaks as there are more domain pairs contributing. The two longest constructs in this study include the C0 and C1 modules and their 50-amino-acid-proline-alanine-rich linker (P/A_L). The modeling revealed alternate arrangements for the C0 module with respect to the rest of the construct and NMR relaxation data confirmed that this linker was highly mobile.

Thus, while the arrangement of domains C1-C2-C3-C4 remains relatively fixed and independent of the length of these constructs, the structural flexibility in the P/A_L linker could facilitate its putative role as a molecular switch between actin and myosin.

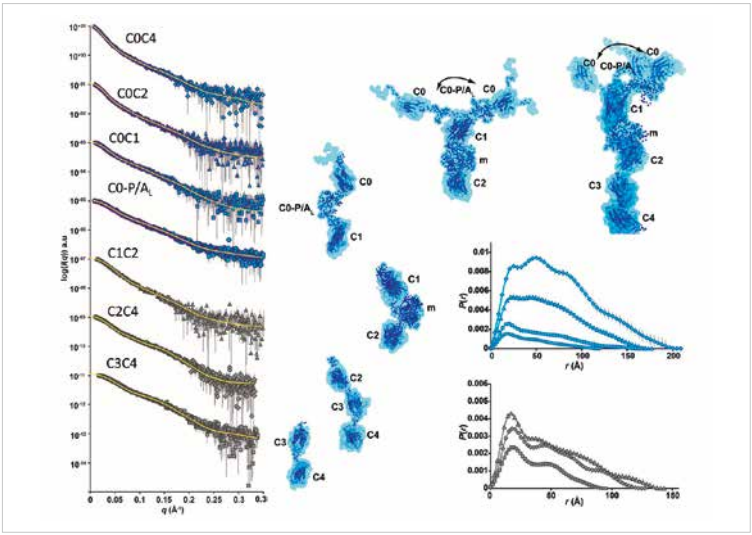

Fig. 39
SAXS data as logI(q) vs q (left panel) for N-terminal constructs of cMyBP-C, labeled with the first and last module of each construct. The symbols are the experimental data and the solid lines are the best-fit models, representations of which are shown in the same order from top to bottom as the data plots. The models are shown as a surface representation of ab initio shape models with atomistic representations for the modules of known structure overlaid. The corresponding P(r) vs r functions, calculated as the indirect Fourier transform of I(q), are in the lower right panels and with the same color coding as for the I(q) vs q plots. Scattering data were acquired using the SAXSess instrument fitted with a 2D CCD detector at the University of Sydney.

6.1.4 Complex biomolecular assemblies and integrative methods

Networks and assemblies of biomolecules interacting in dynamic processes are the foundation of cellular life. Biomolecular complexes built up from multiple protein subunits and nucleic acids are responsible for complex, multi-step processes such as the regulation of gene expression, translation of the genetic code and protein synthesis, responses to environmental stimuli, and – more broadly – also muscle action and motility. The structure and dynamics of biomolecular complexes and assemblies are at the frontier of structural biology today and SAXS is making important contributions to advancing that frontier. SAXS data can provide an important restraint in integrative structure determination when combined with data from other techniques.[44]

SAXS studies of biomolecular complexes include studies of protein complexes,[77]-[81] protein-nucleic acid complexes,[82]-[86] complexes of proteins and/or nucleic acids with ligands,[87] protein-lipid complexes (e.g., proteins embedded in lipid nanodiscs,[88] lipoproteins,[89] and even membrane-less organelles,[90] viruses[77] or entire cells.[91] In addition to structural information, SAXS can provide information regarding the stoichiometry of subunits,[79] and binding affinities.[92], [93] Particularly powerful for studying complexes is a combination of SAXS and SANS (small-angle neutron scattering) and contrast variation.[81], [94] Here we will focus on just a few illustrative examples.

Molecular chaperones and partners

Molecular chaperones function as part of an intricate interaction network with other proteins and ligands. SAXS studies of Hsp90 have informed our understanding of these complex networks through studies of specific complexes with numerous ligands, co-chaperone proteins and substrate proteins,[79], [95], [96] and of Hsp90 mutants.[97] SAXS provided invaluable structural data which was challenging to obtain by other techniques to identify

conformational changes upon interaction of Hsp90 with binding partners, characterize the dynamic interconversion of Hsp90 structural states, and to define stoichiometry of protein complexes of Hsp90 with co-factor and substrate proteins. In several integrative approaches, SAXS data were combined with complementary data from NMR spectroscopy, X-ray crystallography, cryo-EM, and mass spectrometry to obtain a high quality of Hsp90 complex structures with co-factor and substrate proteins,[79], [95], [96] see Fig. 40.

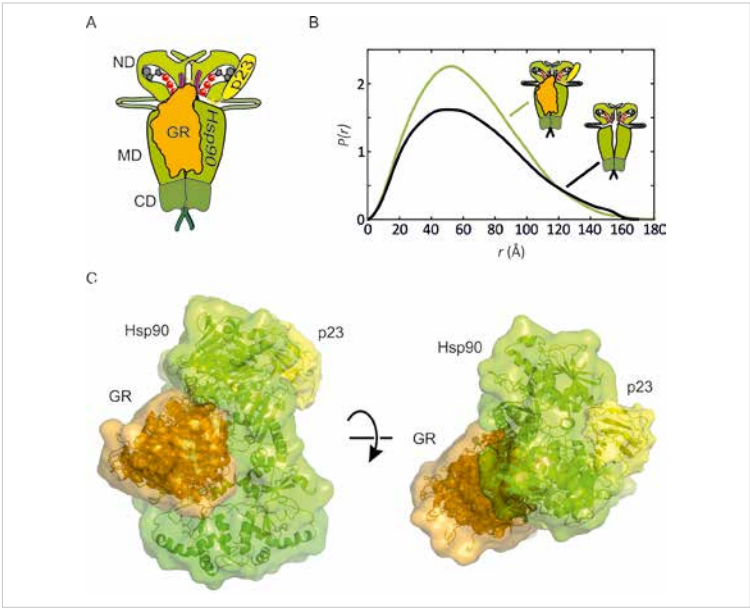

Fig. 40
A. Cartoon of the Hsp90-GR (glucocorticoid receptor)-p23 complex in its ATPγS bound state. GR is a Hsp90 substrate and p23 a co-factor stabilizing the closed conformation of Hsp90. The 3 domains of Hsp90 are labeled (ND: N-terminal domain, MD: middle domain, CD: C-terminal domain). B. P(r) vs r for Hsp90-ATPγS in the absence and presence of one stoichiometric equivalent GR and p23 per Hsp90 dimer. C. CORAL rigid body model of the Hsp90-GR-p23 complex. The structure was obtained using SAXS (overall shape), NMR (intermolecular contacts), EM (overall shape), and X-ray crystallography (structures of subunits) data. A bundle of 5 structures with the best fit to the experimental data is shown. Scattering data acquired at the Technical University of Munich using a SAXSess instrument with 10 mm line source and a CCD 2D detector.

A viral C3 Protease-RNA complex

Picornaviruses are responsible for a range of diseases including meningitis, hepatitis, poliomyelitis, and the common cold. These viruses replicate their RNA genomes through a highly conserved mechanism that involves an interaction between the principal viral protease (3C(pro)) and the 5'-UTR region of the viral genome. The 3C(pro) catalytic site is thus a fine target for drugs that would inhibit virus replication and hence proliferation. Using a combination of SAXS data on the 3C(pro) alone and its complex with a region of the 5'-UTR RNA, termed stem-loop D (SLD), with previous mutagenesis results and NMR, we determined the shape, position, and relative orientation of the 3C(pro) and SLD components (Fig. 41).[98] The data clearly demonstrate the 1:1 binding stoichiometry, with pronounced loops from each molecule providing the key binding determinants for the interaction. Binding between SLD and 3C(pro) induces structural changes in the proteolytic active site that is positioned on the opposite side of the protease relative to the RNA/protein interface, suggesting that subtle conformational changes affecting catalytic activity are relayed through the protein.

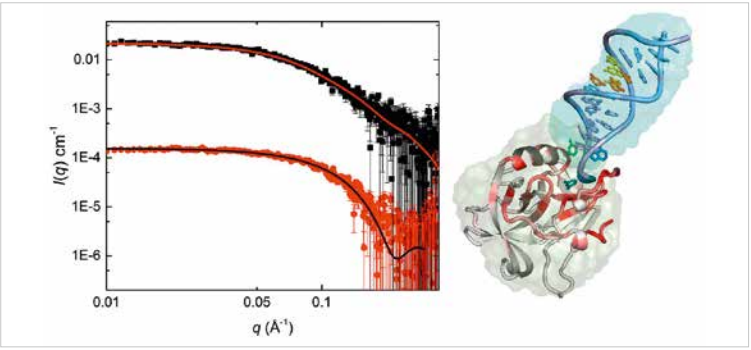

Fig. 41
SAXS data for C3(pro) (red) and its complex with the stem loop region of its RNA binding partner is shown with model fits (solid lines) based on the structure to the right. The protein and RNA components are shown as cartoon representations, with a transparent envelop defining the shapes and dispositions of the two components derived from the scattering data. The SAXS data were acquired using the SAXSess instrument equipped with a CCD 2D detector at the University of Sydney

Cardiac myosin-binding protein C and actin

The interaction of cMyBP-C with actin was explored with a combination of SAXS and SANS with contrast variation.[94] SAXS data were used first to develop a model structure for the N-terminal regulatory domains of cMyBP-C (C0 through C2, or C0C2). Then a solution of actin monomers was combined with deuterated C0C2 in a 1:1 stoichiometry. Upon mixing, the actin monomers formed mini-fibrils and by measuring SANS profiles in solvents with increasing D_2O content, the contribution of the deuterated and non-deuterated proteins to the total scattering was systematically varied. These data encode information about the individual structures and their dispositions. Taking advantage of the SAXS-derived structural model of C0C2 and the known helical assembly of actin monomers in a filamentous form, a model for the C0C2-actin assembly was obtained that fit all of the data. This model predicts that cMyBP-C interacts with actin via the C0 and C1 domains. Interestingly, the binding interface on the actin extends across neighboring actins, thus explaining why the binding appears to stabilize the actin filament. Most significantly, however, and referring to Fig. 38, the binding interface on actin is such that cMyBP-C would interfere with tropomyosin returning to its position in the relaxed state that closes the myosin-binding sites, and at the same time it would compete for myosin head group binding in the cross-bridge forming state see (Fig. 38). The cMyBP-C is found in a specific region of the muscle sarcomere and is present in a stoichiometry of about 1 to 30 actin monomers. Thus we see that the binding predicted by the model could act effectively as a buffer to the primary Ca^{2+} signal that controls the contractile cycle; holding myosin-binding sites open in the absence of Ca^{2+}, which would enable cross-bridge formation and motility, while also competing for the myosin- binding sites, which would decrease motility in the presence of Ca^{2+}. This effect is exactly what is observed in actin/myosin motility assays upon the addition of C0C2.

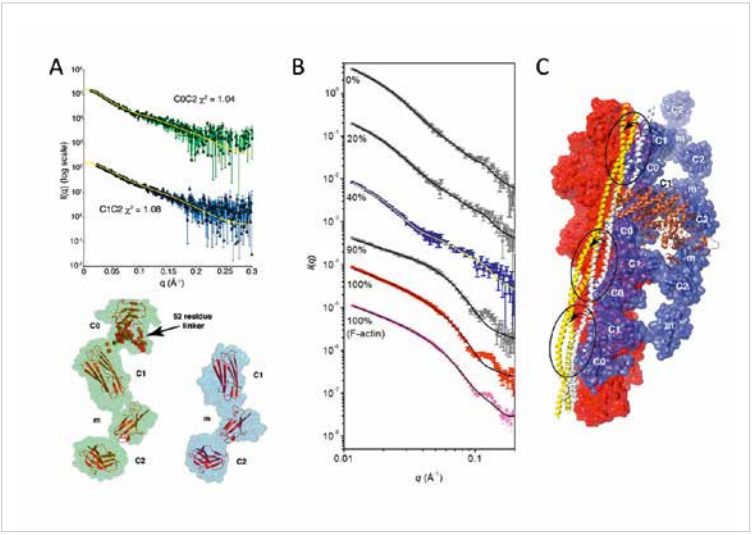

Fig. 42
A. SAXS data as logI(q) vs q for C0C2 and C1C2 of cMyBP-C (mouse isoform) with the derived molecular models shown below as surface representations of ab initio shape models with atomistic models of domains as cartoons. SAXS data were acquired using the SAXSess instrument equipped with a CCD detector at the University of Sydney B. SANS neutron contrast variation data (symbols) for filamentous actin (pink symbols) and for solutions of actin with deuterated C0C2 in different D2O solutions (percentages of D2O as indicated). SANS data were acquired using the 30-m SANS instrument at the NIST Center for Neutron Research. The solid lines are model-fits to the SANS data based on the model in C. C. Model of filamentous actin (red) decorated with C0C2 (blue) based on the SAXS data in A. and showing where tropomyosin would sit in the closed (yellow) and open (white) states and where myosin (brown) would bind to actin.

6.1.5 Summary and conclusion

SAXS is a powerful tool for studying the structure and dynamics of biomolecules and biomolecular complexes in solution. While the experiment is conceptually simple, the requirements of purity, monodispersity, and measuring in the dilute solution regime mean that great care is required in the sample preparation phase, and in the validation that the scattering is from the particle of interest

and free of systematic biases from, for example, concentration-dependent aggregation or inter-particle interference. Most experiments will benefit from synchrotron intensities, especially with the increased availability of inline purification and characterization. Nevertheless, an in-house laboratory-based instrument can be of great value when in training, when synchrotron intensities are not needed or are particularly damaging to the sample, in preparing for a synchrotron experiment, or for dealing with samples that have a very limited lifetime and require sophisticated equipment in their preparation. The flexibility of the solution environment means important physiological parameters and states can be evaluated. By combining SAXS with complementary techniques, detailed structural modeling is possible.

Structural biology progresses when experiments provide information about (i) overall shapes and structures (by SAXS, SANS, X-ray crystallography, NMR spectroscopy, cryo-electron microscopy), (ii) specific distances (NMR spectroscopy, electron paramagnetic resonance, fluorescence spectroscopy), or (iii) proximity/interface information (NMR spectroscopy, cross-linking and mass spectrometry, sequence covariance). The structural biology frontier is increasingly being pushed forward using computational integration of complementary data. By virtue of their critical roles in fundamental biological processes, structures of large biomolecular complexes and assemblies are a central focus. Structural and dynamic characterization of these systems is often challenging due to the scarcity of experimental data, and can only be addressed efficiently by employing an integrative approach. SAXS is maturing as a structural biology technique as evidenced by recent initiatives to establish publication guidelines,[60], [99], [100] its role in integrative/hybrid methods[101] and the establishment of a public database for SAXS data and associated models that is designed to be interoperable with the Protein Data Bank.[102] SAXS is thus poised to continue to grow and develop its contributions to our understanding of biological mechanisms underpinning healthy function, how they are altered in diseased states with the view of contributing to biomedicine, or how we might take advantage of biomolecules and their properties for biotechnology applications.

➤ 6.2. GISAXS – Grazing-incidence small-angle scattering

by Detlef-M. Smilgies, Cornell High Energy Synchrotron Source (CHESS)

6.2.1 Introduction

GISAXS has developed into an important tool to study nanostructured surfaces and thin films.[103] Soft materials have been of particular interest, as many of them can be solution-processed and can self-organize on a nanometer length scale. Well-known examples are conjugated polymers and molecules for organic electronics (typical d-spacings from 1 nm to 10 nm), lipids (3 nm to 30 nm), nanoparticles (3 nm to 30 nm), as well as block copolymers (10 nm to 100 nm). Such systems are of interest to use with industrial coating and printing techniques for flexible consumer electronics, medical sensors, and many other applications.

Now, why do we need grazing incidence for this purpose? X-rays have peculiar optical properties. In particular, their complex refractive index n is slightly less than one:

$$n = 1 - \delta + i\beta \qquad \textit{Equation 49}$$

where δ is the dispersive part governing refraction, and β accounts for absorption. δ is on the order of 10^{-6} to 10^{-5} for common elements. This property has important consequences when we apply Snell's law: X-rays feature total external refraction, i.e., total reflection occurs on the air or vacuum side, as opposed to total internal reflection familiar from transparent optical media. The critical angle α_c of total external reflection can be derived from Snell's law if we take into account that by convention the incident angle α_i of the X-ray beam is measured relative to the substrate surface:

Equation 50

$$\alpha_c = (2\delta)^{1/2}$$

δ depends on the electron density of the material,[104] and for typical materials we get the following values of the critical angle for 10 keV X-rays (λ = 0.124 nm):

organics:	α_c = 0.1° to 0.15°
silicon and glass:	α_c = 0.18°
gold:	α_c = 0.44°

If X-rays impinge on a surface below the critical angle, they cannot propagate into the material. Instead the electric field associated with the X-ray beam is exponentially attenuated and hence scattering from the bulk is suppressed. This way even weak scattering signals from thin films or deposits become accessible.

Working at small incident angles poses some constraints on the substrate surface quality: it should be as flat as possible and with low roughness. Polished silicon wafers with a thin oxide layer are the ideal and readily available substrate material for GISAXS. On a lower budget, glass slides work similarly well, but have a higher background. The other critical constraint of working close to the critical angle is that the line-up has to be just so: a typical substrate with 20 mm width along the beam and at 0.2° incident angle exposes a cross section of only 30 µm to the beam. In order to avoid excessive parasitic scattering the incident beam is also set to only 100 µm or less in height. This requires a thorough line-up procedure. In addition it is very useful to collect the X-ray reflectivity in the vicinity of the critical angles as well. Due to the strong scattering in this angle range, the reflectivity can be detected with the direct beam monitor.

So why are we going to the effort of using GISAXS? The answer lies in the kind of sample we would like to study: a typical organic or inorganic film has a thickness somewhere between 30 nm and 300 nm. Due to the small incident angle we typically probe an area given by the elongated footprint of the X-ray beam on the sample.

The horizontal beam width is typically around 0.5 mm, and the footprint extends the full length of the sample along the beam direction. Typical GISAXS samples are 10 mm to 30 mm in size, so we probe a macroscopic area on the surface of several mm^2, while structures have periods of 1 nm to 100 nm! Moreover, the scattering signal is proportional to the squared volume of the illuminated sample area which for a 100 nm film on a 20 mm substrate amounts to 10^6 μm^3. In comparison a typical transmission SAXS beam probes an area of about 1 mm x 1 mm, that is a factor 10 less scattering volume and thus a factor 100 less scattering intensity. On top of this there is the attenuation by the substrate which for a 0.5 mm silicon wafer at 10 keV reduces the transmission to 3 %. And we don't get information along the height of the film. So that's why we go for grazing incidence.

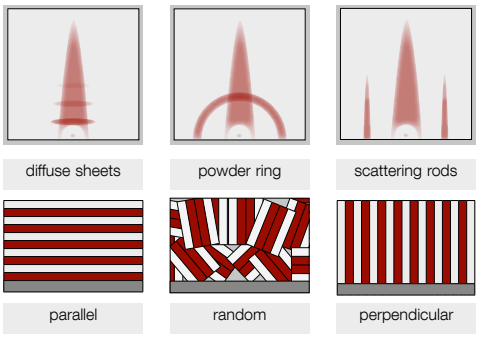

Fig. 43
GISAXS signatures of parallel, random, and perpendicular lamellae (from left to right).

Fig. 43 illustrates the power of GISAXS using the simplest system, regularly spaced lamellae. Lamellae are formed by a variety of soft matter systems such as block copolymers or surfactants. Lamellar stacks only produce Bragg peaks in a direction perpendicular to the lamellar planes. The scattering vector is simply given by the lamellar period L:

$$q_{lam} = \frac{2\pi}{L}$$

Equation 51

If lamellae are oriented parallel to the substrate, we get scattering peaks in the incident plane along the surface normal. For lamellae with random orientation we obtain a powder ring. Due to the fact that scattered X-rays are blocked by the substrate, the powder ring is only visible for exit angles larger than zero. If the lamellae are partially oriented the powder ring will become an arc. Finally, for perpendicular lamellae we will observe Bragg reflections in the direction parallel to the substrate surface. Parallel and perpendicular lamellae are associated with the interaction of substrate and polymer film as well as the free surface energy of the film at the air-polymer interface,[105] while rings or arcs are observed in disordered systems, such as block copolymers right after spin coating, or thick films where the interface-induced order does not persist throughout the whole film thickness.

6.2.2 Basic GISAXS scattering theory

There are already some excellent introductory articles on GISAXS scattering theory.[106]-[108] Here we will give a basic introduction that focuses on concepts rather than on the complete mathematical description. The goal is to make some peculiar scattering features of GISAXS more accessible.

As we saw in the SAXS chapter, transmission SAXS is described within the Born approximation. If ϕ_i and ϕ_s denote the incoming and scattered plane wave, respectively the scattering intensity is given by

Equation 52

$$I_{BA} \propto |\langle \phi_S \mid \rho \mid \phi_i \rangle|^2$$

where ρ is the electron density distribution of the scattering material. With ϕ_i and ϕ_s being plane waves, the scattering intensity is essentially the squared modulus of the Fourier transform of the electron density with respect to the scattering vector q, the difference between outgoing and incoming wave vectors of the respective waves.

In reflection geometry we have to work with the reflectivity wave functions to capture all scattering contributions. Fortunately, the reflectivity wave functions are just a linear combination of the incoming and reflected waves:

$$\psi \propto \phi_i + r\phi_r$$

Equation 53

The complex reflection factor r determines the amplitude and phase of the reflected wave relative to the incident wave and is a function of the incident angle (see[109] for details). Now we are ready to write down the GISAXS scattering amplitude:

$$I_{DWBA} \propto \left|\langle \psi^S \mid \rho \mid \psi^i \rangle\right|^2$$

Equation 54

As we have replaced the simple plane waves of the (Born approximation) with the reflectivity eigenfunctions, this approximation has been termed the "distorted wave" Born approximation (DWBA). Before we evaluate this expression further, let's take a look at the reflectivity eigenfunctions. The X-ray reflectivity R is given as

$$R \propto |r|^2$$

Equation 55

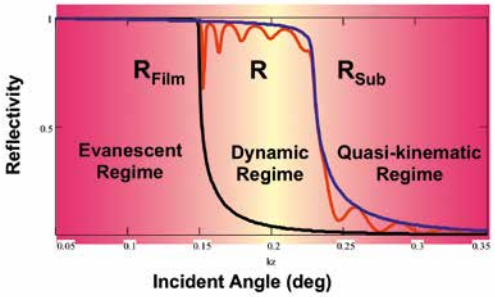

Fig. 44
Typical X-ray reflectivity curves and associated GISAXS scattering regimes.

In Fig. 44 typical X-ray reflectivity curves are shown – substrate (blue), film material (black), and the combined reflectivity of a thin film on a denser substrate (red). Striking features of the latter are the oscillations between the critical angles and above the critical angle of the substrate. The oscillations of the intensity above α_{cS} are the well-known Kiessig fringes[110] that are due to interference of the wave scattered from the surface and the interface of the film and provide a precise determination of the film thickness. The oscillations between the critical angles are of a different nature. Here the reflected wave is almost as strong as the incident wave, and a standing wave field forms.[111] When a node of this wave field coincides with the film surface, a resonance condition is attained, and the wave gets trapped inside the film, similar to a waveguide.[112] Because of the wave getting trapped in the film, there is more absorption, and the waveguide modes show up *as* minima in the reflectivity curve.

Because of the strong interplay of incident and reflected wave, the scattering regime between the critical angles can be termed the *dynamic* regime, in analogy of the dynamic theory of X-ray diffraction. There are two other regimes where for the most part only one wave comes into play: In the evanescent regime the incident wave impinges below the critical angle of the *film* material and undergoes total external reflection. Hence the scattering intensity gets exponentially damped in the film, and at about half the critical angle the penetration depth of the wave reaches a minimum penetration of about 5 nm to 10 nm.[109] This regime is often used to obtain information about the near-surface region of the film, as compared to the fully penetrated film at higher scattering angles. Finally, beyond the critical angle of the *substrate* there is the *quasi-kinematic* regime: when the intensity of the reflected wave is below 10 % of that of the incident wave then interference effects can be neglected, except for the Yoneda band of the scattered wave. In this regime scattering intensities are much lower, but the scattering theory can be much simplified.[113]-[114]

When we look at a typical GISAXS image of a smooth film, as shown in Fig. 45, we see a system of bright horizontal lines between the

critical angles of film and substrate. These are due to the standing waves/waveguide resonances in the *scattered* wave: in this case scattering from the film is enhanced and the resonances show up as *maxima*. The complex behavior between the critical angles is related to the Yoneda peak in diffuse reflectivity and the Vinyard peak in grazing-incidence diffraction and originates from the incident and reflected wave being of similar amplitude and scattering in-phase.[109]

As in GISAXS we are in the vicinity of the incident plane, we have termed the bright band of scattering between the critical angles of film and substrate the Yoneda band. The Yoneda band is a feature of the scattered wave and thus related to the scattered wave field in the DWBA.

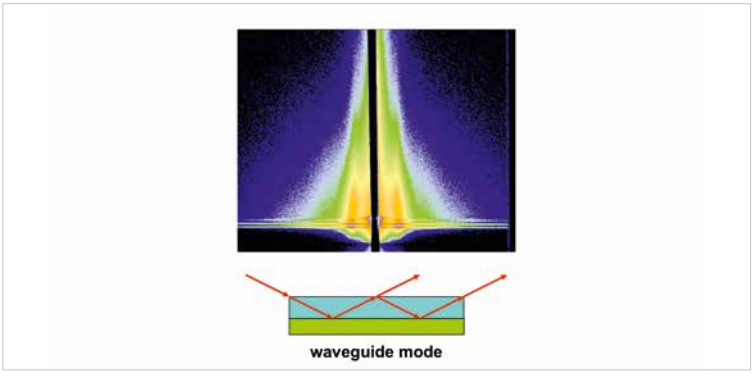

Fig. 45
Yoneda band with 3 waveguide resonances, showing up as the bright lines of scattering between the critical angles. The vertical streaks are due to standing cylinders in the block copolymer thin film.

For practical purposes the first waveguide mode, just above the critical angle of the film, is very useful: The wave field probes all of the interior of the film, and scattering intensity is enhanced. Higher-order waveguide modes have nodes inside the film. This can be used for very precise structure determination[115] but is beyond the scope of this chapter. In Fig. 46 we show the resonant scattering as the incident wave goes through the resonances. It needs to be emphasized that this behavior can only be observed in very flat and smooth films, such as spin-coated polymer films, so that the incident angle is well-defined.

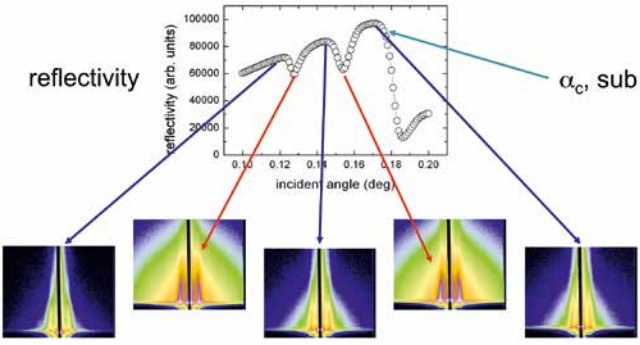

Fig. 46
Reflectivity curve between the critical angles with two waveguide resonances and associated scattering images taken at the same exposure time. The intensity enhancement due to the waveguide resonances is clearly visible.

So back to the original purpose: how do we derive quantitative information about the film? First of all we note that the GISAXS intensity factors into scattering parallel to the surface and perpendicular to it. The parallel part essentially can be evaluated as SAXS in the Born approximation. However, the scattering in the perpendicular direction turns out to be more complex. We will now evaluate the DWBA matrix element which yields:

Equation 56

$$I_{DWBA} \propto \left|\langle\phi_i^s \mid \rho \mid \phi_i^i\rangle + r^i\langle\phi_i^s \mid \rho \mid \phi_r^i\rangle + r^s\langle\phi_r^s \mid \rho \mid \phi_i^i\rangle + r^i r^s\langle\phi_i^s \mid \rho \mid \phi_i^i\rangle\right|^2$$

The leading term is the BA matrix element referring to the direct scattering process. The other matrix elements refer to processes in which either the incoming beam gets reflected before scattering or the scattered beam gets reflected after scattering or both, respectively. As it turns out, the squared moduli of these four matrix elements are the dominant contribution to the scattering,[108] although occasionally a mixed interference term can show similarly strong effects.[105] Terms one and four yield scattering in the same direction (the double reflections in term 4 cancel out), as do term two and three involving a single reflection.

This characteristic of the scattering process produces doubled up features in the dynamic scattering regime: there is the scattering

from the direct beam and the scattering from the reflected beam. For practical applications we distinguish two important cases:

- One interface, objects on the substrate surface
- Thin film with two interfaces and embedded objects

The first case corresponds to the above equation and is important to characterize nanoscopic objects on the substrate surface. This can be, for instance, metal clusters on an oxide surface,[106] self-organized quantum dots,[116] or a layer of nanoparticles.[113] The associated DWBA wave function is well discussed in literature.[106]

The second case which is one of the most-applied scattering geometries has an extra challenge: The reflectivity wave function has now three regions (vacuum/film/substrate). However, the wave function remains a simple superposition of two plane waves in each region, as in the previous case. In addition it is very important to take the refraction of the X-ray beam into account. Specifically for the vertical component of the wave vector κ inside the film the following holds:

$$K_z^i \propto \sqrt{(k \sin \alpha_c)^2 - \left(k_z^i\right)^2}$$

Equation 57

where κ_z^i is the wave vector component inside the medium.

If there is a scattering event inside the film with associated scattering vector $\boldsymbol{q}$, then the following holds for the z components:

$$K_z^S = K_z^i \pm q_z$$

Equation 58

The plus sign refers to the direct and double-reflected scattering events, the minus sign to the scattering events involving a single reflection.[107]

Finally, the scattered wave vector undergoes refraction as it leaves the film:

Equation 59

$$k_z^s \propto \sqrt{(k \sin \alpha_c)^2 - (k_z^s)^2}$$

With the help of these formulae, we can relate the vacuum wave vector components to the scattering inside the film:[107]

Equation 60

$$k_z^{s\pm} = \sqrt{(k \sin \alpha_c)^2 + (K_z^i \pm q_z)^2} = \sqrt{(k \sin \alpha_c)^2 + \left(\sqrt{(k \sin \alpha_c)^2 - (k_z^i)^2} \pm q_z\right)^2}$$

Thus, the z-component of apparent scattering vector as measured on the detector in the air/vacuum region is related to the z-component of the scattering vector inside the material by

Equation 61

$$q_z^{app} = k_z^{s\pm}(q_z) - k \sin \alpha_c$$

Fig. 47 shows a typical application of this refraction/reflection correction for the case of a block copolymer film featuring parallel lamellae. Due to the weak scattering intensities these measurements were performed in the dynamic regime for a range of incident angles. The resulting peak positions as a function of incident angle can be fitted by two parameters: α_{cF}, the critical angle of the film, and the lamellar period L, which relates to the scattering vector associated with the parallel lamellae as $q = 2\pi/L$. Note that without taking the refraction/reflection effect into account, a naive determination of the period using the vacuum wave vectors would either yield values that are off (red branch – direct scattering) or outright wrong (green branch – reflected beam scattering).

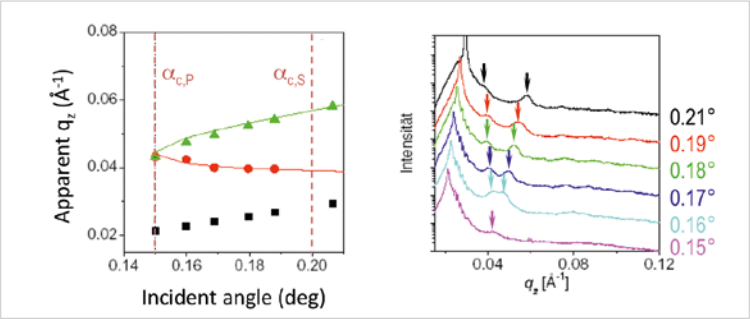

Fig. 47
Vertical scattering intensity close to the beamstop of a film consisting of parallel lamellae. Left panel: The lamellar peaks show a specific shift and splitting as a function of the incident angle in the dynamic range due to the refraction/reflection effect. Right panel: Fitting the peak positions with the formula for the apparent qz yields a polymer critical angle of 0.15° and a lamellar spacing of 19.7 nm.

If we have a truly 3D lattice, the refraction formulae are also to be used to model the perpendicular peak locations properly and derive the correct vertical periodicity. The case of scattering objects enclosed in a film has been discussed by a variety of authors.[105]-[108], [117]-[118] As a general rule we always need to take the scattering layer and the refracted wave vectors therein into account, also for more complex multilayer systems.

In the full-fleshed DBWA scattering theory, the refraction correction is included automatically as a property of the reflectivity wave functions. A variety of codes are available for simulation of scattering images: e.g., IsGISAXS,[106], [119] FitGISAXS,[120]-[121] HipGISAXS,[122]-[123] and BornAgain.[124] The publication by Müller-Buschbaum in Springer Lecture Notes in Physics 776, 2009, provides a step-by-step introduction to IsGISAXS, how adding features to the electron density distribution contributes to the scattering pattern.[125]

6.2.3 Application examples

Having delved deeply into the subtleties of the GISAXS process, the time has come to reward ourselves with some pretty pictures. When GISAXS was initially applied to thin films of soft materials, much work was done on block copolymers. All known phases of diblock copolymers have been observed by now. In addition the thin film interfaces often induce a preferential orientation of the polymer domains. Both parallel and perpendicular lamellae and cylinders have been observed. In addition BCC spheres,[118] the gyroid,[108] and hexagonally perforated lamellae[126] were identified. Silica mesophases[127] and nanoporous thin films[117], [128] behave quite similar to block copolymers, and display analogous structures.

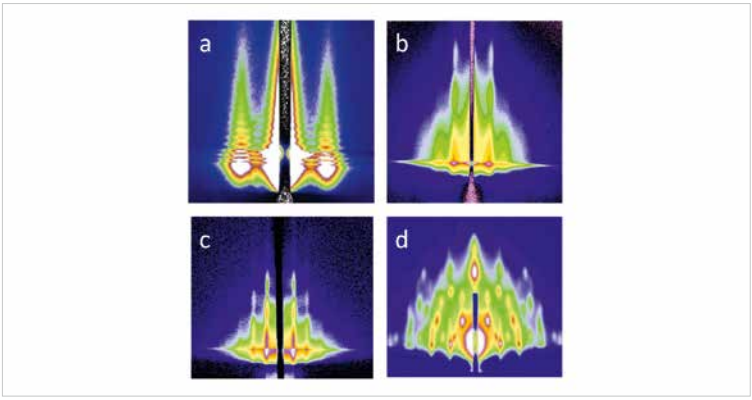

Fig. 48
A glance at the variety of GISAXS images for block copolymer-derived structures: (a) standing cylinders with height corresponding to the film thickness[129] (b) monolayer of spherical voids in a silica matrix[130] (c) monolayer of shear-oriented lying cylinders[131] (d) titania gyroid after pyrolysis of the original block copolymer.[128] More detailed information about the samples can be found in the indicated literature.

Another important class of target materials are self-assembled nanocrystal superlattices. Nanoparticles are typically synthesized in the 2 nm to 20 nm size range. In addition a variety of shapes can be obtained which have influence on the superlattice symmetry.[132]

Simple round particles with short ligands form a dense FCC packing. If ligands are on the same length as the particle diameter, entropy wins out and particles form BCC packing,[133] similar to the situation of block copolymer micelles.[134] Another case arises for non-spherical particles: nano-octahedra pack in a very open bcc packing with an unusual tip-to-tip orientation of adjacent particles.[135] A possible reason for this behavior may be the low density of ligands at corners and edges as opposed to the flat faces.

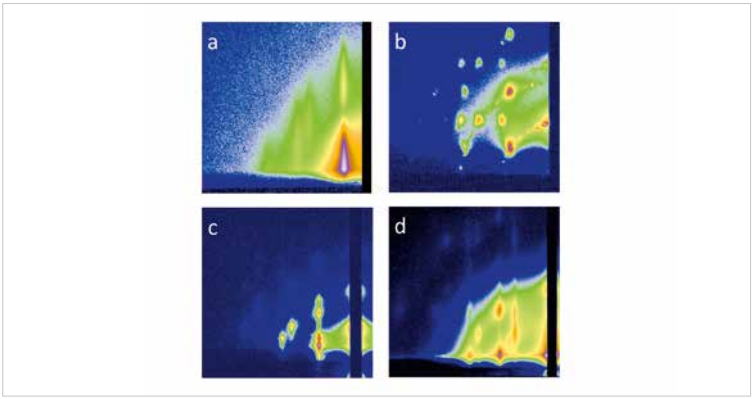

Fig. 49
Overview of the variety of nanocrystal superlattices. (a) Hexagonal monolayer of FePt nanospheres,[113] (b) BCC lattice of Pt3Ni nano-octahedra [Fang], (c) Rhombohedral arrangement of PbS nanocubes[136] (d) Binary AB2 superlattice of Fe oxide and gold nanoparticles.[137]

Even the crystallization of nanocubes is more complex than one would assume: simple cubic, tetragonal, and rhombohedral superlattices have been observed, depending on the specific crystallization conditions.[136], [138] Particles with a pronounced non-spherical character such as nanorods[139] or platelets[140] display other types of lattices. Finally, binary superlattices consisting of two particles of different size form yet another sequence of lattice morphologies.[137], [141]

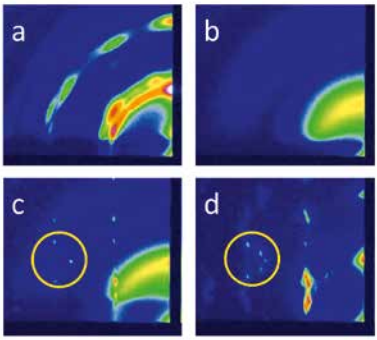

Fig. 50 *Lead sulfide nanocrystal superlattices: (a) after dropcasting a 3D FCC lattice is formed with random orientation of the superlattice grains (b) in hexane vapor the nanocrystals return to the solution phase (c) onset of crystallization with some solvent left: a well-oriented FCC phase develops with the (111) plane parallel to the substrate. (d) Upon further drying the nanocrystals "feel" their neighbors more strongly and the lattice becomes body-centered tetragonal, as evidenced by the spot splitting indicated by the yellow circles. Shrinkage in one of the <100> direction is stronger than in the others. Eventually the superlattice goes through the full Bain transition and ends up BCC. For a detailed description see references [142] and [143].*

A spectacular orientational transition was observed for cuboctahedral particles: as the solvent evaporates they start out with isotropic orientation of the individual particles, the well-known Kirkwood-Alder transition for spherical colloids,[145] but as particles get closer they start to feel the anisotropy in the ligand sphere more strongly, and undergo a continuous Bain transition from FCC through a variety of tetragonal phases to finally a BCC structure.[142]-[143] Grazing-incidence wide-angle X-ray scattering revealed that these particles acquire more and more orientational organization as the superlattice sheds more and more interstitial solvent molecules and compacts into the BCC phase.

An overview over the variety of GISAXS applications is given in several web tutorials.[103], [144]-[146]

6.2.4 Acknowledgements

This GISAXS chapter is the fruit of my longstanding collaborations with a number of CHESS user groups as well as discussions with other X-ray scattering experts. Specifically I would like to thank (in alphabetical order): Peter Busch, Tobias Hanrath, Andy Heitsch, Brian Korgel, Ruipeng Li, Peter Müller-Buschbaum, Ben Ocko, Christine M. Papadakis, Dorthe Posselt, and Markus Rauscher. I thank Kaifu Bian, Peter Busch, Josh Choi, Phong Du, Brian Goodfellow, Tobias Hanrath, Marleen Kamperman, Christine Papadakis, Vincent Pelletier, Danielle Smith, Ben Treml, and Jun Zhang for providing me with data files that were used in the figures. GISAXS images were plotted using the Fit2D software.[147]

➤ 6.3. USAXS – Ultra-small-angle X-ray scattering for materials science

by Jan Ilvasky, X-Ray Science Division, Advanced Photon Source, Argonne National Laboratory, and Fan Zhang, Material Measurement Laboratory, National Institute of Standards and Technology

6.3.1 Introduction

Ultra-small-angle scattering refers to small-angle scattering collected for scattering vectors q smaller than 0.001 $Å^{-1}$ of X-rays (USAXS) or neutrons (USANS). Using $d = \pi / q_{min}$, where q_{min} is the minimal q that the instrument can access, the typical maximum dimensions (d_{max}) characterized by USAXS/USANS are greater than 300 nm. Currently, the state-of-the-art USAXS instruments routinely achieve a q_{min} of ≈ 10^{-4} Å-1 or a d_{max} of ≈ 3 µm, and USANS instruments can achieve a q_{min} of ≈ 10-5 Å or a d_{max} of ≈ 30 µm. These dimensions often provide unique insight into features that would typically require imaging techniques. Scattering offers capabilities that may be difficult to obtain from, and are complementary to, imaging – scattering results are statistically representative because of the larger sample volume. When placed on absolute intensity scales, scattering techniques provide information regarding the scattering objects' size, shape, specific surface area, and absolute volume. The scattering methods are also nondestructive and can accommodate complex sample environments, enabling in-situ or ex-situ experiments for samples that are not optically transparent or lack optical contrast. Such advantages make USAXS/SAXS techniques uniquely useful for studies of complex materials with hierarchical structures such as polymers, metals and alloys, natural materials (such as minerals, sediments, and soils), and many more.

For the USAXS instrument, q_{min} defines the smallest accessible q. An often-overlooked component is that USAXS instruments must have a meaningful q resolution, q_{res}, especially for the data points close to $q$min, because a significant number of data points in the ultra-small-angle range are required to describe and interpret the

structures of interest. For the USAXS instrument in a Bonse-Hart geometry (see below), the q_{res} is defined by the width of the crystal rocking curve and is similar to q_{min}, allowing for 10 or more meaningful data points below 0.001 $Å^{-1}$. For pinhole-based USAXS instruments, one must be conscientious about this criterion and carefully evaluate the q_{res} based on the targeted X-ray energy, the detector pixel size, and other geometrical parameters.

As alluded to above, the two types of standard USAXS instruments are 1) long pinhole cameras (e.g., ID02 at ESRF and P03 at PETRA III) with a focused X-ray beam and 2) Bonse-Hart-type devices available as desktop instruments and a synchrotron instrument (APS USAXS). Between these two types of designs, the Bonse-Hart devices are more compact and can measure sizes up to four decades in q. Furthermore, when combined with a supplementary high-performance SAXS camera and an X-ray diffraction camera (XRD, or wide-angle X-ray scattering, WAXS), a superior measurement capability is created which covers five or more decades in q and enables comprehensive structural characterizations from less than an angstrom to several micrometers. These attributes make the Bonse-Hart devices the most popular choice to access the USAXS regime in commercial desktop setups. We emphasize that Bonse-Hart and pinhole USAXS devices have their respective advantages and disadvantages, making these two configurations more complementary than competitive. Proper selection of the most appropriate configuration is essential for successful experiments, and so is the proper selection of other experimental conditions, such as type of radiation (X-rays or neutrons), X-ray wavelength, and sample environment.

The Bonse–Hart geometry, which utilizes crystal optics, has a high angular resolution defined by the width of the crystal rocking curve. It is worth mentioning that the Bonse-Hart geometry finds applications in both X-ray and neutron scattering. While USAXS and USANS share the same general principles, they have their niches and advantages. For example, the crystal rocking curve of neutrons is significantly narrower than its X-ray counterpart, allowing

USANS instruments to access a size ≈ 10 × d_{max} for USAXS with the same crystals. The Bonse-Hart USANS instruments are available as dedicated user instruments at several neutron-scattering facilities worldwide (ILL, NIST, ORNL, and ANSTO). However, they fall outside the scope of this chapter.

For the rest of this chapter, we will further discuss the Bonse-Hart-type USAXS instruments, which have been used for ultra-small-angle scattering experiments for more than 40 years.[148]-[151] We will focus on USAXS and provide an overview of its development state and technical capability in the form of desktop instruments or dedicated synchrotron facilities. We will use USAXS and Bonse-Hart USAXS interchangeably, unless specified otherwise.

6.3.2 Bonse-Hart instrumentation

The Bonse-Hart device (Fig. 51) utilizes two pairs of crystals. Here, we assume the crystals reflect the X-ray beam vertically, but horizontally scattering devices are also available.[152] In a USAXS measurement, a monochromatic X-ray beam first arrives at a pair of channel-cut crystals, referred to as collimating crystals, that collimates the X-ray beam. The crystal optics have an angular acceptance window of approximately the full width at half maximum (FWHM) of the double-crystal rocking curve. This acceptance window is extremely narrow, allowing only the X-ray beam parallel within the acceptance angle to pass through. For example, at 21 keV, Si (111) optics has an FWHM of ≈ 17.2 µrad (3.5 arcsec), ensuring the exiting beam is highly parallel along the vertical direction. Once aligned, the collimating crystals remain stationary. After the collimated beam encounters the sample, small-angle scattering events occur. A rotating second set of crystal optics, placed after the sample, resolves the scattered beam. This second pair of crystals, known as analyzer crystals, probes the angular intensity distribution of the scattered beam and provides the point-wise data acquisition for the USAXS data. We also note that in the schematics below, the collimation only occurs along the vertical direction,

and the beam divergence along the horizontal direction is significantly larger. This disparity in orientationally dependent collimating conditions creates a slit-smearing geometry, requiring post-experiment data analysis to acquire the proper differential scattering cross-section.

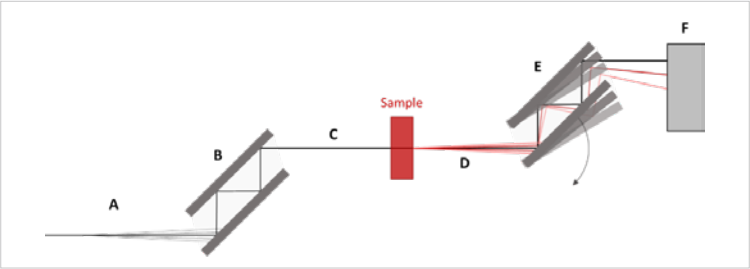

Fig. 51
Schematics of Bonse-Hart device: Uncollimated primary beam (A), collimating channel-cut crystals (B), vertically collimated (parallel) primary beam after the collimator (C), primary beam which has passed through the sample, includes attenuated primary beam with addition of sample scattering (D), rotating analyzer channel-cut crystal (E), X-ray detector (F).

Bonse-Hart USAXS data acquisition requires two measurements. First, without the sample, one acquires the instrumental profile ("empty" or "blank"), including the crystal rocking curve and other instrumental scattering signatures such as air scattering, scattering from crystal surfaces, slits, and any X-ray windows. The second measurement requires the sample in the beam, and the acquired scattering curve combines both the instrumental profile and the sample scattering profile. The difference between these two rocking curve profiles (after normalization and transmission correction) is the (slit-smeared, see below) scattering of the sample.

Because USAXS data acquisition involves rotation of the analyzer crystals, USAXS instruments are much slower than the pinhole SAXS instruments, where all q values are collected at once. Hence, when measurement efficiency is essential, in, e.g., in-situ experiments, we must consider the data collection strategy for USAXS measurements to enable an efficient throughput. Two common measurement strategies exist for USAXS measurements: step

scan or fly scan. In step scan mode, the analyzer crystals move over a pre-determined set of angles (q) and collect data for a predefined time at each angle. In the fly-scan mode, the analyzer crystals rotate continuously with simultaneous data acquisition. The fly-scan mode does not involve repeated starts, stops, and counting cycles. Hence, the measurement is typically faster and more X-ray efficient. However, during a fly scan, the measured intensity at each resulting q represents integrated intensities acquired over a range of angles (qs), resulting in additional smearing that modifies the instrumental q-resolution. The step-scan mode does not have this movement-induced smearing issue. Furthermore, one must recognize that it is impractical to use linearly spaced steps because of the wide range of q the USAXS instruments cover. A common practice is to define an array of measurement angles (q) on a semi-logarithmic scale, with small steps at the smallest measurement angles and progressively increasing step sizes towards higher angles. A rule of thumb is to have 10 to 50 points per decade in q, a data density suitable for most USAXS applications. Because of these limitations, the Bonse-Hart USAXS data collection will always be slower than the pinhole SAXS, and USAXS data points will have worse counting statistics.

Bonse-Hart USAXS instruments can measure scattering data over a broad q-range. For example, the APS USAXS instrument has provided measurement capability from 10^{-4} Å^{-1} to ≈ 1 Å^{-1} since the early 2000s. However, because the SAXS intensity typically decreases asymptotically following q^{-4} (in the slit-smeared case, q^{-3}), the instrumental q-range also depends on the X-ray flux on the sample and detector capabilities. Desktop instruments with a typical flux ≈ 10^7 photon/s can realistically measure about two decades in q (typically from 0.0002 Å^{-1} to 0.01 Å^{-1}) with a data collection time between 10 min and 30 min, depending on the sample's scattering power. Synchrotron instruments, with an undulator or bending-magnet source, may have X-ray flux exceeding 10^{12} photon/s, enabling access to a q value of 0.3 Å^{-1} or higher with a data collection time of minutes.[153]-[155] However, the counting statistics above q=0.1 Å^{-1} are poor even with synchrotron measurements.

A unique feature of the Bonse-Hart geometry is that the beam size has no impact on the *q*-resolution of the instrument because the *q*-resolution is related only to crystal optics and potentially data collection strategy (e.g., fly scanning as described above). The USAXS instruments routinely utilize beam sizes ≈ 1 mm^2 and USANS instruments even 1 cm^2. This feature is valuable because the illuminated sample volume can be substantial, yielding excellent sampling statistics. For example, the APS USAXS instrument, when operated at 21 keV, enables the measurements of water-based samples that are 4 mm thick. With a beam size of 1 mm x 1 mm, the sample volume is 4 mm^3. This large, illuminated sample volume enabled by USAXS may be necessary when the scattering objects have low concentrations or contain significant inhomogeneities, thus circumventing the sampling challenges experienced by typical pinhole SAXS instruments, especially those utilizing a focused beam.

Bonse-Hart devices also have different requirements for their detectors compared to typical pinhole SAXS instruments. While USAXS detectors do not require spatial resolution because of their point-wise detection, they need to have a sizeable linear-intensity dynamic range, high efficiency, and low noise. The extensive linear-intensity dynamic range is critical and requires further explanation. For USAXS measurements, the detector needs to take on the whole, direct beam, where the beam can have a photon density exceeding 10^{12} photon/s at a synchrotron source. Meanwhile, the detector must have linearity and sensitivity to measure the scattering intensity near the background level, which is often six to ten decades below the direct beam intensity. On the one hand, current desktop Bonse-Hart devices typically reuse their SAXS area detectors with single-photon counting capabilities, such as a PILATUS* or an EIGER* detector. On the other hand, synchrotron-based

* Certain commercial products or company names are identified here to describe our study adequately. Such identification is not intended to imply recommendation or endorsement by the National Institute of Standards and Technology, nor is it intended to imply that the products or names identified are necessarily the best available for the purpose.

USAXS devices use photodiodes combined with high-dynamic-range amplifiers[156] or scintillators equipped with calibrated absorptions filters.[151]

We also note that scattering-based imaging using a Bonse-Hart geometry has been exploited. An imaging detector replaces a photodiode detector to image the transmitted and *q*-specific scattered beam directly. While out of the scope of the current chapter, such imaging methodologies provide visible insight into the degree of the sample inhomogeneities at different length scales.[157][158]

As mentioned previously, the crystal optics defines the excellent q_{min} and *q*-resolution of the Bonse-Hart USAXS instrument. Desktop instruments commonly use Si (111) crystals because these crystals allow the maximum throughput of the direct beam after the collimating crystals. Their q_{min} is $\approx 1.2 \times 10^{-4}$ Å^{-1} with Cu Kα radiation. Other options with higher-order crystal optics exist, allowing an even smaller q_{min}, as demonstrated in Fig. 52. For example, Si (220) and Si (440) crystal optics theoretically enable a qmin of $\approx 0.8 \times 10^{-4}$ Å^{-1} and $\approx 0.3 \times 10^{-4}$ Å^{-1}. The lower FWHM, which gives rise to this better qmin, limits the beam throughput, making these higher-order crystal optics primarily suitable for synchrotron instruments. Even for the synchrotron instruments, this reduction of beam throughput caused by higher-order crystal optics can limit the effective *q*-range of the instrument at the high-*q* end of the scattering profile because the photodiode captures fewer scattered photons during a specific measurement duration.

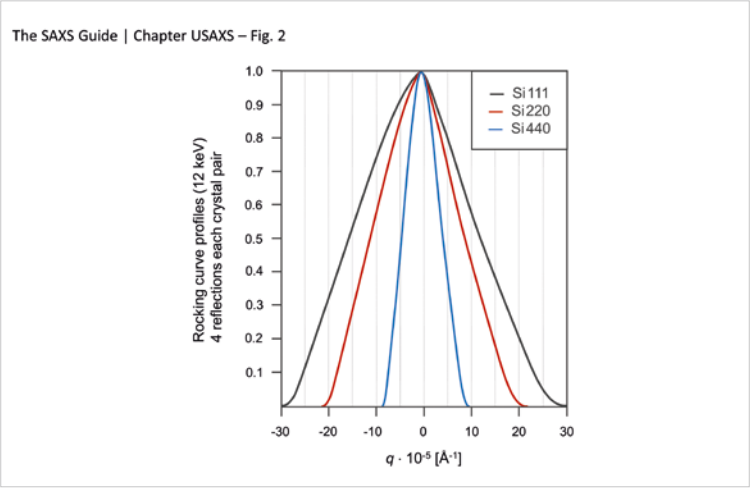

Fig. 52
Comparison for rocking curve widths for Si 111, 220, 440 at 12 keV for four reflections. The higher order planes lead to a narrower rocking curve and enable a smaller accessible qmin and a higher q resolution.

The performance of Bonse-Hart devices also depends on the number of Bragg reflections in each pair of crystals. While the number of reflections does not change the FWHM of the double-crystal curve, it changes the rocking curve profile shape. An increase in the number of reflections reduces the intensity at the tail of the rocking curve and improves the instrument's sensitivity by suppressing its natural background.[159] We believe the minimum number of reflections for USAXS is three in each crystal pair, a criterion also commonly used in the USANS instrument. An odd number of reflections in each crystal pair causes the beam to change direction significantly, which can be advantageous when suppressing background in the detector is critical, such as in the case of USANS. For X-rays, this creates a challenge because the new beam direction is energy-dependent since it follows the Bragg condition. This energy dependency makes it complicated for a USAXS instrument with changeable energy and is usually only adopted for fixed-energy instruments. Most USAXS instruments today utilize four (or six) reflections in each crystal pair. In this case, the beam retains its original direction, hence making changes in X-ray energy much easier to accommodate. Fig. 51 illustrates a case of four reflections in two parallel crystals in both the analyzer and the collimating crystal pairs. For each pair, the outgoing beam is vertically offset

by a small distance determined by the number of reflections, the gap between the crystals, and the scattering angle while maintaining the same direction as the incident beam. Some desktop instruments utilize Bartell channel cut crystals, where the beam direction after four reflections is the same as the incoming beam direction. However, this setup is less X-ray efficient due to Bartell crystal's lower throughput.[160]

The concept of slit smearing, while not unique to Bonse-Hart devices, is critical for data analysis. The detected scattering intensity at a given q in a slit-smeared Bonse-Hart USAXS instrument contains scattering data over a solid angle shaped like a rectangle. In angular terms, the rectangle's minor dimension is defined by the FWHM of the crystal optics. Its major dimension is primarily related to the size and shape of the detector and the sample-to-detector distance. When expressed in a q unit, this major dimension is known as the slit length. When the slit length is less than qmax, we consider the slit length finite. Here, q_{max} is the maximum q of a USAXS measurement. When it is comparable to or greater than q_{max}, we consider the slit length infinite. The distinction between finite slit length and infinite slit length is essential because it impacts data processing and the USAXS instrument's ability to place data on an absolute intensity scale. While devices with finite slit length can place data on an absolute intensity scale using first principles by calculating the solid angle, acquiring absolute intensity data is much more difficult (if not impossible) for devices with infinite slit length.

In mathematical terms, the measured intensity follows

Equation 62

$$I(q) = \Phi_0 \, A \, t \, T \, \epsilon \, \Omega \frac{d\Sigma(q)}{d\Omega}$$

Here, A is the illumination area, t is sample thickness, T is sample transmission, Φ0 is the incident flux in the unit of photon/s/area, ϵ is the detector efficiency, and d∑(q)/dΩ represents the differential scattering cross-section per unit volume per unit angle. In a

slit-smeared USAXS measurement, the observational solid angle is the size of the slit, defined as slit height along the q direction (typically, the rocking curve FWHM described above) × the slit length. If the slit length is infinite, numerically, the solid angle loses meaning and becomes effectively unknown. However, in everyday practice, we can assume a maximum slit length of 4p/*l*, which is significantly larger than q_{max}, to circumvent this restriction and allow absolute calibration.

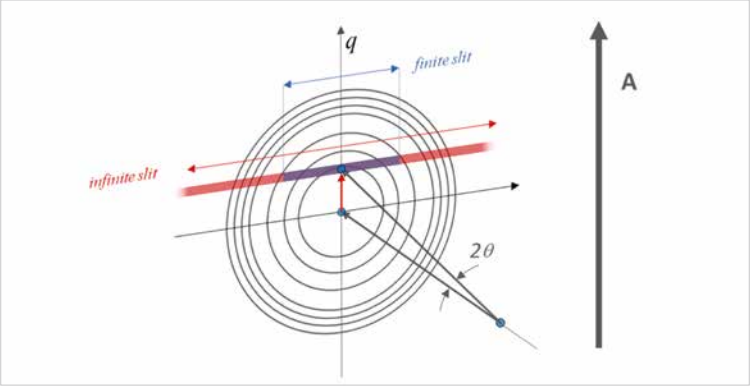

Fig. 53
*Schematics of finite slit scanning: the red area represents the infinite slit and the blue area the finite slit (for the finite slit, the slit length is half of the slit dimension shown in the figure). A represents the scanning direction, 2θ is the scattering angle, and **q** is the scattering vector.*

Slit smearing impacts the applicability of Bonse-Hart USAXS instruments, especially for materials with anisotropic scattering profiles, because slit smearing integrates the scattering signal within the observing solid-angle non-discriminatorily. Based on the experimental slit-smeared data, it is possible to reconstruct a pinhole-collimated scattering profile using various desmearing routines, such as the Lake Method.[20] We strongly recommend smearing the model using a slit calculated from the known instrumental parameters and performing least-squares or other optimization routines using the smeared model on the smeared data. Nevertheless, in either case, the basic assumption is that the scattering data is isotropic. When this assumption does not hold, the data-desmearing or model-smearing approach breaks down, and rigorous and quantitative data analysis becomes difficult or impossible. For this reason, we strongly advocate using a long-pinhole USAXS instrument for materials with known microstructural anisotropy.

Finally, we note that 2D-collimated Bonse-Hart devices have been developed to measure anisotropically scattering samples. These devices use two collimating crystal pairs (one vertical and one horizontal) and two analyzer crystal pairs (one vertical and one horizontal). These crystals define a slight solid angle; the devices become SAXS instruments with an ultra-high resolution. The usage of four pairs of crystal optics also makes the instrument much less X-ray-efficient. Therefore, it is only usable at synchrotrons with highly collimated X-ray sources and high photon flux.[151] Data acquired by such devices no longer require a desmearing routine, and it is possible to rotate the analyzer crystals to map the reciprocal space, albeit with low efficiency. The 2D collimation also places a stringent requirement on the absolute intensity measurements – the crystal tilts in both crystal planes must be centered to ensure that the $q = 0$ position in the scanning direction is also at zero q in the orthogonal plane. Because of these challenges, these 2D-collimated Bonse-Hart devices are rarely used, and long pinhole USAXS instruments are the preferred method to fulfill the measurement need for anisotropic USAXS measurements.

6.3.3 Hierarchical structure in soft materials

Structure hierarchy is the rule, instead of an exception, of nature.[161] From the beauty of DNA, where alternating sugar and phosphate groups self-assemble into a twisted ladder as a double helix, to the superb combination of bending and compressive strength of bone,[162] owing to its uniquely hierarchical structure spanning from sub-nanostructure to macrostructure, nature realizes extraordinary materials properties through the hierarchical organization of molecules to microscopic and macroscopic scales. The pursuit of advanced functional materials with hierarchical structures represents a frontier of not only modern materials science[163] but also human discovery.[164] One central challenge to recapitulate a level of control to precisely create such materials resides in the mastery of control at each structural level, which requires a deterministic characterization of hierarchical materials.

Soft materials, such as polymers and colloids, often form a hierarchical structure. Delineating these structures is essential to developing the application-critical structure-property-performance relationship and requires experimental techniques that resolve microstructures over a large and continuous size range. Moreover, in situ or operando characterization with a time resolution relevant to the transformation of these materials upon external stimuli, such as pressure, temperature, and electrical field, is beneficial. USAXS, especially synchrotron-based USAXS, is well-suited for these applications and provides a unique opportunity to peer into these widely used materials.

In this section, we will present two selected examples to illustrate the exciting science enabled by USAXS and bring forward the vast possibilities for which USAXS may be a suitable characterization tool to contribute to the continued development of materials science benefitting mankind's quality of life.

6.3.3.1 Polymer composite with nanometer-sized reinforcement fillers

Polymer composites with nanometer-sized reinforcement fillers have captured significant imagination from the materials research community because of their potential to drastically improve the materials' mechanical performance at filler loadings at less than 1 % mass. One premier example is the targeted application of nano-silica to replace carbon black as the filler material for automobile tires. This replacement promises to improve the tires' tread life and offers the possibility to enhance the tires' wet-grip properties while providing a more negligible rolling resistance, thereby improving the vehicle's fuel efficiency and reducing its carbon footprint. However, the enhancements to the modulus of the composites with the addition of hard fillers remain marginal, and practical solutions to this problem remain elusive.

Schaefer and Justice, in a now landmark paper, rigorously investigated the filler morphology and critically evaluated the morphology's role in possible modulus enhancement.[165] Using

Dimosil-precipitated silica, a type of precipitate silica with a high specific surface area (100 m^2/g – 400 m^2/g) as an example, they performed structural analysis using the transmission electron microscope, USAXS, and light scattering. The TEM data, shown in Fig. 55(b), clearly demonstrated that the primary particles of the precipitated silica are quasi-spherical and ≈ 20 nm in size with a smooth surface and form aggregates. It is, however, difficult to quantify the size or structure of the aggregates based on TEM data alone.

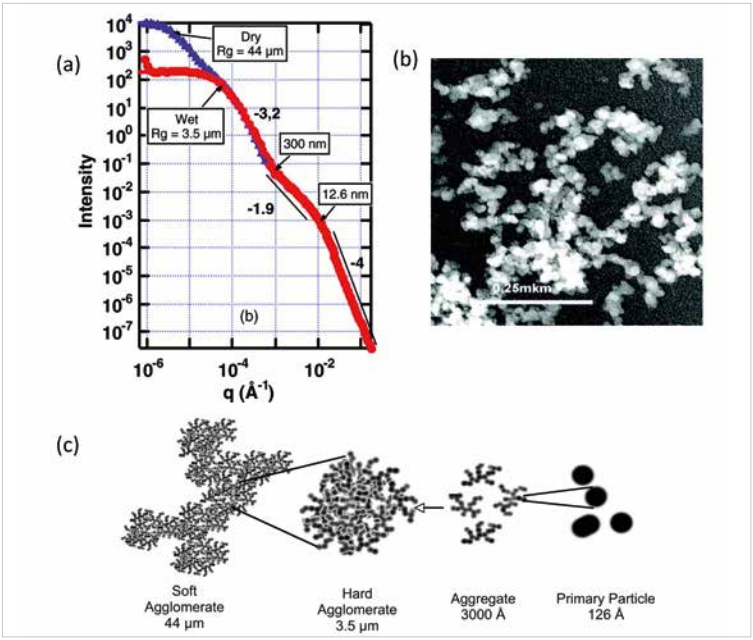

Fig. 54
(a) Combined light scattering and USAXS data revealing different structural levels in the Dimosil-precipitated silica. (b) TEM data showing the primary precipitated silica particles and their aggregates. (c) An illustration of the different structural levels in the precipitated silica. Adapted with permission from [165] Copyright (2007) American Chemical Society .

The scattering data, shown in Fig. 54(a), includes both USAXS and light-scattering data and encompasses a q-range from to ≈ 2 × 10^{-6} $Å^{-1}$ to 0.3 $Å^{-1}$, and provides conclusive evidence of the existence of structural levels of the Dimosil-precipitated silica in their wet (red) and dry (blue) states. Both the dry and wet silica contain:

- Primary particles ($R_G \approx 13$ nm)
- Aggregates ($R_G \approx 300$ nm)
- Hard agglomerates ($R_G \approx 3.5$ μm)

Here, R_G is the radius of gyration.

The dried product also includes a ≈ 44 μm soft agglomerate whose presence is susceptible to ultrasonic perturbation. This rich structural insight, only available through a scattering experiment with a broad and continuous q-range, unveils the mechanistic basis for the lack of improvement to the modulus of the nanocomposites with the addition of hard fillers. The modulus of a fractal aggregate inversely depends on the aggregate size. The filler nanoparticles in polymer nanocomposites aggregate ubiquitously. Hence, once the aggregate size is adequately significant so that the aggregate modulus is below the matrix modulus, the desired reinforcement effect will not occur. This critical insight points to the importance of filler-morphology control in the commercial success of these nanocomposites, a continued direction in optimizing nanocomposite materials.

6.3.3.2 Structure of binary colloidal suspensions

Colloidal suspensions, also known as colloidal dispersions, involve particles in the size range of a few nanometers to a micrometer dispersed in a fluid medium. Colloidal suspensions are omnipresent in everyday life: they are present, e.g., in ink, paint, blood, and milk.[166] They also form the basis for some of the most advanced functional materials, including colloidal hybrid nanostructures with multiple functionalities,[167] colloidal lipid nanoparticles as drug carriers,[168] and self-assembled colloidal gels with dynamic color tunability.[169] Many of the fundamentals of the colloidal suspensions, such as their thermodynamics, microstructures, and transport properties, can be traced to the delicate interparticle interactions. The variety of the interactions, including electrostatic, steric, and depletion interactions, adds to the richness of colloidal science and provides avenues to tailor the structure and property control

at microscopic and macroscopic levels. Traditionally, static and dynamic light scattering played a significant role in understanding the nature of the colloidal interactions. However, they are of limited use when dealing with concentrated or turbid suspensions. USAXS, in contrast, is less sensitive to multiple scattering common to visible light in concentrated suspensions and provides the appropriate size range to understand the structure of the colloidal suspension, including the form factor, structure factor, and the equation of state. Therefore, it has found numerous applications in the investigations of various colloidal suspensions, including colloidal dynamics using a version of X-ray photon correlation spectroscopy in the USAXS regime.[170][171]

Much of the research focused on determining the stabilization conditions of colloidal suspensions has been devoted to monodispersed systems, whose physical description has the most clarity. Because of the introduction of a second species, the binary system adds complexity to understanding the force balance required to achieve colloidal stability. In one remarkable example,[172] Tohver *et al*. demonstrated that introducing a critical volume fraction of highly charged zirconia nanoparticles stabilizes a suspension of charge-neutral colloidal microspheres, which otherwise would flocculate due to van der Waals attractions. Competing theories emerged to explain this so-called “nanoparticle halo” phenomenon. In one case, Karanikas and Louis used a hypernetted chain integral equation closure to calculate the effective interparticle potential[173]. They found the stability is driven solely by electrostatic repulsion between nanoparticles in solution. In another case, Liu and Luijten performed Monte Carlo simulations and demonstrated a weak nanoparticle-microsphere attraction at low nanoparticle concentration leads to stabilization.[174] Yet, in neither instance is the van der Waals potential between the large spheres considered, rendering an incomplete physical description. Characterization of the fluid structure is required to provide the structural details and enable elucidation of the physical nature of the nanoparticle halo effect. However, the large size disparity between the microspheres and nanoparticles makes such measurements difficult. To meet

this challenge, we performed a series of USAXS measurements on a series of silica microsphere and zirconia nanoparticle suspensions,[175] and an example of the results is shown in Fig. 55.

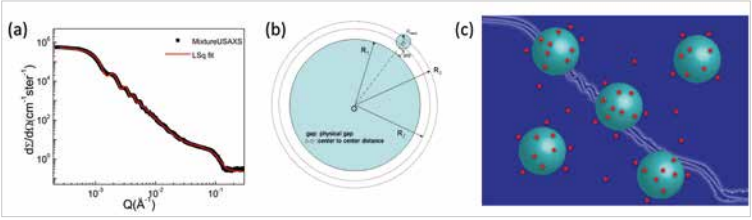

Fig. 55
(a) USAXS data of a stable suspension consisting of monodispersed, charge-neutral silica microspheres (mean radius 280 nm ± 9 nm) and highly charged zirconia nanoparticles (mean radius 2.6 nm ± 0.5 nm). (b) A core-shell model developed to analyze the scattering data. (c) An illustration of the physical picture of the dynamic nanoparticle haloing effect, where a high concentration of zirconia nanoparticles is located near, but not attached to, the microsphere surface. Adapted with permission from[175]. Copyright (2007) American Chemical Society.

Using the experimentally determined scattering form factor of the highly monodispersed uncharged microspheres and highly charged zirconia nanoparticles as input, we constructed a core-shell type scattering model (Fig. 55(b)). In this model, we allowed the physical gap and the electron density of the shell to vary to describe the mean location and the number density of the zirconia nanoparticles near the surface of the microspheres. This model described the USAXS data, shown in Fig. 55(a), very well and presented a physical picture, as illustrated in Fig. 55(c). In short, we determined the zirconia nanoparticles self-organized into a shell near the microspheres. The mean separation distance is approximately the Debye length of the solvent. Within the shell, the nanoparticle concentration is significantly higher than its bulk concentration with a lateral nanoparticle-nanoparticle separation distance ≈ of five × the nanoparticle size. These findings were later confirmed by atomic force microscope measurements,[176] providing the direct structural basis for validating theoretical predictions.

Due to space, we limit the USAXS investigation of hierarchical structure in soft materials to these two examples. However, we must reemphasize the hierarchical structures are the rule rather

than the exception in these fascinating yet complex materials that also include polymer gels, solutions, blends, micelles, vesicles, and microemulsions. USAXS provides a powerful tool for understanding the different structural levels and their roles in determining the properties and performances of these materials[177].

6.3.4 Microstructure and kinetics in hard advanced engineering materials

Andre Guinier, often considered the father of the field of small-angle scattering, first applied SAXS in 1938 to discover the formation of so-called Guinier-Preston zones in an Al-Cu alloy, a specific pre-precipitation phenomenon in alloys critical for alloy hardening.[178] Despite these early applications, soft matter research largely dominates SAXS applications in materials science. One primary reason is the limitations imposed by the limited X-ray energies from a lab-based tube or rotating anode source. In contrast to X-ray diffraction, where lab-based measurements are often conducted in the Bragg–Brentano (reflection) geometry, SAXS (GISAXS not included) requires collecting data close to the direct beam. It must be undertaken in transmission geometry. For example, the Cu source, the most used lab-based X-ray source, sits at 8.04 keV for Cu Kα radiation. For a steel sample to achieve a 5 % sample transmission, the sample thickness must be less than 15 µm. This stringent requirement creates challenges in sample preparation. It also casts questions about the measurement statistics, a key advantage of SAXS that sets SAXS measurements apart from less statistically representative electron microscope measurements. Because of these reasons, the in-house SAXS measurements for hard engineering materials, such as ceramics, alloys, and metal-ceramic composites, have lagged behind their soft materials counterparts. The emergence of synchrotron-based SAXS during recent decades has empowered a resurgence of SAXS measurements of hard engineering materials due to its access to higher X-ray energies. Together with rapid fly-scan measurements and an additional wide-angle X-ray scattering (WAXS or XRD) detector,[150] the synchrotron

USAXS instruments enable a rare window to investigate a comprehensive structure evolution at both atomic and microstructural levels. The USAXS user community has made significant progress toward understanding a multitude of hard engineering materials, such as thermal barrier coatings,[179] cement,[180] alloys,[181][182] rocks,[183][184] and nuclear materials.[185]

In this section, we will use one example to highlight the power of comprehensive studies of the kinetic transformations of an alloy system.[186] The material, commercially available aluminum alloy 2024 (AA2024), is one of the most widely used aerospace materials due to its high yield strength, good fracture toughness, and excellent fatigue properties. This alloy is a precipitation-hardening alloy and primarily consists of Al, Cu, and Mg. Because its mechanical properties depend on the number density, location, and size of the precipitates, understanding the precipitation pathway and kinetics is essential for tailoring the material for specific applications.

We performed several insitu, isothermal experiments at different temperatures within a temperature range of 190 °C and 226 °C, typical of the precipitation heat treatment temperatures of this alloy. A solutionization heat treatment creates an identical condition for different experiments where the solute atoms are part of a supersaturated solution. Upon heating the material rapidly to the target temperature, we captured USAXS and XRD data continuously on the same sample volume as a function of time.

Fig. 56(a) shows an example of the USAXS data acquired at 226 °C. Immediately, we noticed that small, nanometer-sized clusters formed rapidly (within a few minutes) during the heating process. These clusters are similar to what Guinier identified in his aforementioned groundbreaking work on Al-Cu alloys, commonly assumed to be precursors to an equilibrium phase. As time proceeds, our data show that these clusters dissolve entirely, and the second type of large precipitates forms. TEM data of this study[186] provides conclusive evidence that the later-formed precipitate is the primary strengthening phase called the S phase. The in situ XRD

data, shown in Fig. 56(b), also corroborates TEM results regarding the formation of the S phase and the lack of long-range order of the co-clusters. Importantly, our results demonstrate the absence of S″, a controversial transient, nonequilibrium phase speculated to exist in the transformation sequence between co-clusters and the S phase.

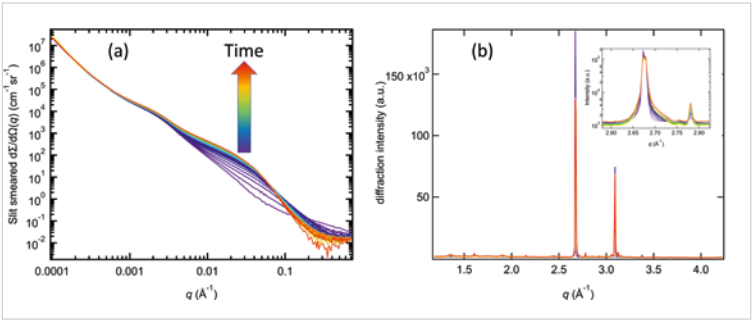

Fig. 56
(a). Time-dependent USAXS data acquired on a commercially available aluminum alloy 2024 during isothermal heat treatment at 226 °C. During this heat treatment, the GPB zones dissolve, and S phase precipitates form. (b) XRD datasets acquired simultaneously with the USAXS data, showing the development of the S phase precipitates during the isothermal heat treatment. More details can be found in [186].

Equipped with the time-dependent data, we could determine the kinetic energies required for the dissolution of the clusters and the formation of the S phase precipitates. The kinetic data demand additional attention because they form a rigorous basis to validate and benchmark predictions made by computational materials science methods, such as Computer Coupling of Phase Diagrams and Thermochemistry (CALPHAD). These computational tools, equipped with machine learning methods, have become increasingly essential to probe the large-parameter space routinely encountered in engineering materials for materials discovery and optimization. Structure- and microstructure-based kinetic datasets are the starting points for such modeling efforts. The capabilities afforded by USAXS and its accompanying SAXS and WAXS are still under-exploited and require more community awareness to unleash their full potential.

To conclude, USAXS, as a statistically significant probe, provides unique measurement capabilities for dimensional metrology. Depending on the source, optics, and accompanying instruments (SAXS and WAXS), a USAXS facility or a desktop SAXS instrument equipped with a USAXS module can cover over five orders of magnitude in sizes, from sub-Angstrom to several μm. USAXS has also evolved from a once-niche technique only available at the synchrotron X-ray facilities to a mainstream measurement tool offered by commercial SAXS equipment vendors. USAXS is also proving to be a powerful technique to enable the across-length-scale structural characterization of a wide range of materials ranging from advanced materials such as alloys and batteries to everyday encounters such as wood and chocolate. These structural data are essential to constructing the processing-structure-property relationships of advanced material, technological building blocks for a 21st-century economy. The recent development in the X-ray sources in synchrotron X-ray and desktop sources is leading to faster and better USAXS measurements and promises an even brighter future for USAXS instruments. We foresee USAXS playing a critical role in advancing materials research, development, and innovation across many industrial sectors.

7. Industrial Applications

➤ 7.1. Introduction

More than 100 years have passed since the discovery of X-rays. The rapid technological developments of X-ray sources, optics, computing power and software programs have revolutionized many experimental techniques, which have evolved X-ray methods and their increasingly dominant role in the characterization of materials. Many of these methods have become routine practice among scientists and researchers who study materials at atomic, molecular and super-molecular structure levels and the material's structure relationship to physical, chemical and biological properties.

Small-angle X-ray scattering (SAXS) is a fundamental method for structure analysis of condensed matter, and has emerged as an essential tool used to unravel structure details with characteristic dimensions at length scales of up to 100 nm and beyond. It is used at all fronts in material science for development purposes. The SAXS method yields information on the sizes or shapes of particles and also on the internal structure of disordered and partially ordered systems. The corresponding method to analyse structures spread over planar surfaces is grazing-incidence SAXS. This is a relatively new method but the interest in it is ever increasing.

The applications cover various fields, from metal alloys to synthetic polymers in solution and as bulk material, biological macromolecules, emulsions, porous materials, nano-particles, etc. In the 1960s, the method became increasingly important in the study of biological macromolecules in solution because it allowed for the first time to get low-resolution structural information on the overall shape without the need to grow crystals. Moreover, SAXS also makes it possible to investigate in real time[187]-[191] intermolecular interactions such as self-assembly and large-scale conformation changes, on which biological functionality often relies. The random orientation of particles in solution leads to an averaged scattering

pattern, so that only a one-dimensional information about a three-dimensional structure can be obtained. The main difficulty and simultaneously the main challenge of SAXS as a structural method is to extract information about the three-dimensional structure of the object from these one-dimensional experimental data. In the past, only overall particle parameters (e.g., mean radius of gyration, particle symmetry, surface per volume) of the macromolecules were directly determined from the experimental data, whereas the analysis in terms of three-dimensional models was limited to simple geometrical bodies (e.g., spherical, cylindrical, lamellar).

For inorganic and especially polymeric systems, integral parameters extracted from SAXS are usually sufficient to answer most of the structural questions. Electron microscopy (EM) was, and still is, often used as a guide to build consensus models. The 1990s brought another class of SAXS data analysis methods, allowing ab initio shape and domain structure determinations[32]-[34] and detailed modeling of macromolecular complexes using rigid body refinement.

The rationale behind new developments in modern materials science is to tailor a material (by varying the chemical composition, constituent phases and microstructures) in order to obtain a desired set of properties suitable for a given application. A key driver in the development of modern materials of today has been the ability to control their structure and functional properties and its relationship to the potential applications in the emerging fields of nano-materials. The self-assembled and hierarchical structures and the functions offered by these self-assemblies, such as micelles, liquid crystals, emulsions, liposomes, and solid-gels, consisting of amphiphilic organic polymers, are utilized in a wide variety of industrial fields. In addition, not only self-assemblies of organic amphiphiles, but also nano-structured inorganic materials, such as composite TiO_2 particles and mesoporous silicas and modified biological substances (e.g., recombinant and purified proteins) are in great demands.

The properties of functional materials are strongly linked to their size, shape, internal structure and interaction potential. To understand and develop functionalized materials, one requires advanced computer programs to evaluate scattering data. Data evaluation forms an important and integral part of SAXS experiments and is required to understand material properties in detail. In dense systems the scattered intensity is a combination of single-particle scattering (form factor) and inter-particle scattering (structure factor). Available standard programs usually assume diluted systems, and neglect the particle interaction. In many applications, it is undesirable or even impossible to dilute a sample. One of the most recent developments in data-evaluation programs now allows the interpretation of such data, the Generalized Indirect Fourier Transform method.[37] It facilitates the determination of the form factor and the structure factor simultaneously from experimental data with a minimum of a priori information.

It is routine now to evaluate with modern computer programs the size, the shape and the internal structure (e.g., the hydrophobic core radius and the hydrated hydrophilic shell thickness).

The information about inter-particle interactions in dense systems can be deduced by analyzing the structure factor with various potential models assuming repulsive or attractive interactions. These are considered[192], [193] to play a vital role in the stability of functionalized systems, the residence time or the activity of medicines in the human body, and similar applications.

➤ 7.2. Functionalization of self-assembled structures

Self-assembled structures[192], [194]-[195] have provoked considerable interest in the context of both natural and synthetic materials, as they can lead to functional materials with nano-scale structures. The most fundamental tasks in nano-science are

1. The development of nanostructures
2. Understanding (or tuning) their function-property relationship in successful applications

Small-angle X-ray scattering is taking the leading role in the determination of key relationships between nanostructures and their functions.

7.2.1 Personal health care (cosmetics, toiletry and sanitary)

Self-assemblies of amphiphilic molecules, called micelles, are often utilized to solubilize water-insoluble functional substances, such as vitamins, perfumes and many more, in water-based products. Lyotropic liquid crystals in lamellar and reversed hexagonal phases are used for emulsion-type products to improve their stability and viscoelastic properties. The sol-gel structures of amphiphilic molecules, especially their high viscosity and good ability to sustain a considerable amount of water, are widely applied to the productions of shampoos, hair conditioners, and cosmetic creams. In addition, high performance cosmetics are on the market that give a gradual release of ingredients on the skin surface. Liposomes or vesicles consisting of phospholipids or synthetic surfactant bilayers play an essential role and act as nanocapsules.

Polymer gels are soft materials that swell due to incorporation of huge amounts of solvent in their three dimensional network of polymer chains. They are widely utilized in sanitary products, baby's diapers, contact lenses, moisturizing agents for dry grounds, etc. Future uses as drug carriers, gel-based actuators, and artificial muscles are also extensively investigated. For instance, a polymer gel consisting of N-isopropyl acryl amide (NIPA) and sodium acrylate possesses hydrophilic and hydrophobic domains in its polymer network. The domain size can be controlled by temperature and/or the adsorption of metal ions and it can be detected by scattering methods. This gives valuable status information about the process of adsorbing materials, for instance, in the recovery of rare or precious metal ions.

Inorganic substances also have emerged and play an important role in these fields. For instance, the recent increase in the risk of skin cancer demands the use of anti-UV foundation creams

(sunscreens) against sunburns. These foundations are functionalized by micron to nanometer-sized inorganic (titanium dioxide) particles. However, to avoid damages of the skin caused by the catalytic effects of TiO_2, the particles have to be coated by silica layers with thicknesses in the order of a few nanometers. Specificially engineered inorganic composite particles can, for the first time, act as hypoallergenic functionalized material to protect human skin.

7.2.2 Pharmaceutical materials

For years, much attention has been paid to drug delivery systems that transport drugs directly to the affected parts of the patient's body. A typical and serious example is that anticancer drugs ward off cancer cells but also damage normal cells simultaneously, which causes a number of side effects and lower the patients' quality of life. Drug delivery systems are made of nano-carriers (in the typical size range of 20 to 100 nm) and they shall make it possible to provide the required amount of drugs timely to a specifically affected part with pinpoint accuracy. A wide variety of self-assembly systems (micelles, microemulsions, liposomes, cubosomes, and polymer-gel nanoparticles) has been tested as drug carriers. Especially, poly(oxyethylene)-polyamino acid block copolymer stabilized cubosomes of monoglycerides are spotlighted as possible candidates. It is also known that surface-conjugation techniques for drug carriers improve their functions, possibly due to modified inter-particle interactions. Not only nano-assemblies but recombinant and purified proteins with special additives have been earnestly examined as artificial oxygen carriers.

7.2.3 Food and nutrients

The structural information has become more and more important for developing better textures and functionalities that make food products wholesome. Surfactants such as poly(oxyethylene) sorbitan ester (tween or polysorbate), sucrose ester, and lecithin are added as an emulsifier or solubilizer to many processed food products, forming micelles or liquid crystals. Polymer gels are very appreciated materials in food such as jelly, the Japanese-favorite Konnyaku (konjak), and tofu (bean curd). They are soft and swelling materials that take up huge amounts of solvent into their three dimensional networks of polymer chains. Nanostructures of triglyceride solids are quite important to obtain good textured chocolate, ice cream, whipped cream, and many more.

7.2.4 Nano-structured inorganic materials

Nano-sized inorganic particles are used in a wide variety of industrial fields such as cosmetics, paints and ceramics production. Among them, mesoporous materials have recently been paid much attention to because of their potential applications as high performance catalysts or molecular sieves. These materials are obtained via ordered nano-templating by surfactant self-assemblies. It is known that chlorophyll extracted from plants is easily damaged by light, but it can be preserved for a long time if trapped in the (2 nm to 50 nm) pores of mesoporous silica. Nanostructures, matter are anticipated to open the door for the development of solar cells that are more efficient than the conventional silicone-based cells.

➤ 7.3. Nanocomposites

The idea of combining the properties of inorganic nanocolloids with polymers has led to a new class of materials, the so-called nanocomposites. These materials have been described as the next great frontier in material science. They have attracted

substantial attention because of their various industrial applications and because of their academic interest. Particular attention has been given to plate-like particles, such as clays, because of their high aspect ratio (large radius r, small thickness h). Because of this anisotropic structure, nanoclay particles enhance the performance properties of the material, even when small amounts of <5 wt% are added. An important property of disperse clay particles is their exfoliation into single silicate layers with a thickness of about 1 nm. In order to facilitate the interaction of silicate layers with the polymer, the hydrophilic nature of the clay particles needs to be changed to organophilic. Traditionally, this is achieved by exchanging the metal cations on the exfoliated clay surface by cationic surfactants.

Inorganic nanoparticles (e.g., soot, silica particles, coated silicates, etc.) are used as fillers to enhance the performance of polymeric materials. One aims to improve the thermo-mechanical properties as well as to achieve value-added performance, such as electrical conductivity, thermal conductivity and selective permeability. The characterization of the morphology of the nanoparticles and their degree of dispersion is an important point in developing such nanocomposites. Presently, organically coated silicates are of great interest for the modification of polymeric materials. The morphological behavior of layered silicates, the structure relationship to the desired properties and the quanitification are desirable information to understand and to tune up these materials.

➤ 7.4. Biological nanocomposites

Biological materials, such as shell, bone and tooth, are organic-inorganic hybrid composites of protein and mineral with superior strength, hardness and fracture toughness. It is quite remarkable that nature produces such tough materials out of protein constituents as soft as human skin and mineral constituents as brittle as classroom chalk. Understanding the mechanisms by which nature designs strong and tough composites with weak materials can give

us a guideline for the synthesis of man made novel materials. Previous research showed that although they have various hierarchical structures, the biological materials have similar elementary building blocks. X-ray scattering (SAXS) has shown that many biomaterials share a nanostructure consisting of staggered nanoscale mineral structures with very large aspect ratios embedded in a soft protein matrix.

➤ 7.5. Liquid crystals

Condensed matter, which exhibits intermediate thermodynamic phases between the crystalline solid and simple liquid states, is called liquid crystal or mesophase. The liquid-crystalline state[196] generally possesses orientational or weak positional order and thus reveals several physical properties of crystals and of liquids. If transitions between the phases are given by temperature, they are called thermotropic. In blends (containing also other components) phase transitions may also depend on concentration, and these liquid crystals are called lyotropic. While thermotropics are at present mostly used for technical applications, lytropics are important for biological systems, e.g., membranes.

Liquid crystals have two main phases, which are called the “nematic phase” and the “smectic phase.” The nematic phase is the simplest of liquid-crystal phases and is close to the liquid phase. The molecules float around as in a liquid phase but are still ordered in their orientation. The smectic phase is close to the solid phase. The liquid crystals are ordered in layers. Inside these layers, the liquid crystals normally float around freely, but they cannot move freely between the layers.

Since their discovery considerable work has gone into trying to understand the properties of liquid crystals and how these relate to molecular structure. Despite this work there exists only a poor understanding of how changes in the molecular structure affect the material properties. The SAXS method provides structural information about heterogeneities, aggregate ordering, size, shape,

separation and intermolecular spacing within the aggregate stack. It is also useful to study interdependence of morphology and phase behavior.

The potential applications of liquid crystals are in display technology, optical imaging and recording, light modulators, thermal sensors and biological membranes (drug delivery carriers).

➤ 7.6. Biocompatible polymers

The name "biocompatible polymers" has evolved in conjunction with the continuing development of materials used in medical devices. Until recently, a biocompatible material was essentially thought of as one that would "do no harm." The operative principle was that of inertness as reflected, for example, in the definition of biocompatibility as "the quality of not having toxic or injurious effects" on biological systems. The discovery of novel polymeric biomaterials – and the refinement of traditional ones – has created a thoroughly unprecedented excitement in the field as polymer chemists and other materials designers increasingly confront many of the fundamental challenges of medical science. As the biomaterials discipline itself evolves, the startling advances of the last few years in genomics and proteomics, in various high-throughput cell-processing techniques, in supramolecular and permutational chemistry, and in information technology and bioinformatics promise to support the quest for new materials. The tremendous range of current biomaterials research is proposing innovative new polymers for applications ranging from cardiovascular devices to gene therapy. Several of the more interesting formulations are highlighted below.

7.6.1 Protein-based polymers

A series of recently introduced casein-based and soy-based biodegradable thermoplastics have recently joined collagen as a source of natural protein-based biomaterials.

In contrast to collagen, however, these polymers are less susceptible to thermal degradation, can be easily processed via melt-based technologies, and can be reinforced with inert or bioactive ceramics. Temporary replacement implants, scaffolds for tissue engineering, and drug-delivery vehicles are among the potential biomaterials uses under investigation.

7.6.2 Polymers for gene therapy

Concerns about the potential risks associated with viral gene-delivery systems have led to the development of both degradable and nondegradable, targeted and non-targeted polymeric gene carriers. Examples are PLL-PEG-lactose as a carrier for the transfection of plasmid DNA at hepatocytes; a biodegradable cationic polymer, poly(a-[4-aminobutyl]-L-glycolic acid), as a carrier for mouse plasmid DNA to prevent insulitis; and biodegradable gelatin-alginate microspheres as a carrier of adenovirus (Ad5-p53) for intracranial delivery.

7.6.3 Silicon-urethane copolymers

A novel family of silicone-urethane copolymers has been developed that, compared with traditional polyurethane biomaterials, offer advantages in biostability, thromboresistance, abrasion resistance, thermal stability, and surface lubricity, among other properties. Copolymer synthesis is performed via two methods: incorporation of silicone into the polymer backbone together with organic soft segments, and the use of surface-modifying end groups to terminate the copolymer chains. The organic soft block can be either polytetramethyleneoxide (PTMO) or an aliphatic polycarbonate used together with polydimethylsiloxane (PSX). Applications for the new materials include balloons, ventricular assist devices, vascular grafts, pacemaker leads, and orthopedic and urologic implants.

➤ 7.7. Mesoporous materials

These materials have pores that can be periodic, non-periodic or amorphous. Porous materials are classified into three classes based on their pore diameters d:[197]

- Microporous (d <2 nm)
- Mesoporous (2 nm < d <50 nm)
- Macroporous (d >50 nm)

A narrow pore-size distribution (PSD) gives rise to interesting and important size and shape-dependent properties, such as separation, adsorption and catalysis. Mesoporous materials have pore apertures similar in size to small biological molecules, supramolecules, metal clusters and organometallic compounds. Mesoporous materials that have a narrow pore size distribution may thus be useful as host, support, catalyst and a separation medium for these molecules. Their pore-size distribution critically depends on the method used to synthesize them.

In general, three approaches are used to synthesize inorganic mesoporous materials:

1. propping layered material with pillars,
2. aggregating small precursors to form gels, and
3. templating inorganic species around organic groups.

In the first approach, organic or inorganic pillars are intercalated into an inorganic host. The pillars prop the layers and create pores. The diffusion of pillars into the host leads to a broad distribution of pillars – the pillar's distance. This anisotropy leads to non-periodic structures with broad pore-size distributions.

In the second approach, small silica species and inorganic polymers are allowed to aggregate and eventually to gelate. This process generally leads to amorphous materials that have broad pore-size distributions. The diffusion paths through the pore system are quite complex.

In the last approach, small inorganic building units are assembled around organic templates to form ordered structures that have narrow pore-size distributions. By using an ensemble of organic molecules to create a larger template, this method can be extended to the synthesis of ordered mesoporous materials.

The original method for making porous materials was to make layered systems supported by pillaring. A guest molecule was introduced into the material and later removed leaving pores. Pillars are used to prevent these pores from collapsing. The sizes of the pillars decide the size of the pores. With this method it is difficult to get a uniform pore size.

The principle of making materials with a uniform pore size is based on liquid crystal templating. Materials with pore diameters from 2 nm to 50 nm can be prepared by this method. A three-dimensional liquid mixture consisting of long chain surfactants and silica oligomers are used. Micelles, which form spontaneously, are used as templates. As the system gelates, the amorphous silica is cross-linked at just below the boiling point. When the mixture is solid the organic parts are taken away, e.g., by calcination, leaving back open pores.

To determine mesoporous materials properties, such as pore size and distributions, inter-spacing between the pores, surface-to-volume ratios, internal structures, monitoring of aggregation and transformation processes, the SAXS method can be used effectively and in-situ. Metal-doped mesoporous structures for catalytic applications can also be studied concerning the doping effects on structure and distribution.

Therefore, SAXS may generally help to understand and quantify a variety of processes including the synthesis of zeolites and ordered mesoporous silicas (e.g., MCM-41, SBA-15) and their structure-property relationship.

➤ 7.8. Membranes

Biological membranes and their functionality (e.g., as small chemical reactors) strongly depend on the geometrical and chemical properties of the amphiphilic molecules that make up the membrane walls. Membrane parameters such as electron density profile or the flexibility are important parameters to know because the functionality of the membrane depends on them. For example, the permeability or the tendency to reorganize into micelles, lamellar stacks or vesicles strongly depends on the internal arrangement of the molecules in the bilayers. The inner structure of the membranes can be modified by pharmaceuticals or by changing the temperature. Drug delivery or gene-transfection strategies can therefore be founded on investigations of the membrane structure. The phospholipid-bilayer membranes such as POPC, DOPC and DPPC can be studied with the SAXS method to obtain their electron density, thickness, repeat distance of lamellae and stacks, number of layers, packing and flexibility parameters.

Polyelectrolyte membrane based fuel cells are a very active area of research. The most significant barrier against running such a fuel cell at elevated temperatures is to maintain the proton conductivity of the membrane. The polyelectrolyte membrane's ability to operate above 120 °C could have benefits for both enhanced carbon monoxide (CO) tolerance and improved heat removal. It is required to keep a given amount of water in the membrane. Higher temperature increases the water-vapor pressure, which increases the likelihood that water loss will occur and thus significantly reduce the proton conductivity.

The conductivity of a dry membrane is several orders of magnitude lower than a fully saturated membrane. A number of alternative strategies have been investigated to maintain membrane conductivity in a dehydrating environment (i.e., elevated temperature and reduced relative humidity). The addition of an inorganic material into a polymer membrane can alter and improve physical and chemical polymer properties of interest (such as elastic modulus, proton

conductivity, solvent permeation rate, tensile strength, hydrophilicity and glass transition temperature) while retaining its important polymer properties to enable operation in the fuel cell. The hydration properties of membranes are key characteristics that can influence fuel-cell performance.

The SAXS method is very useful in studying composite membranes and to establish structure-property relationships.

➤ 7.9. Protein crystallization

To understand and predict protein, crystallization from solutions have been paramount tasks for years. This was motivated by the following reasons.

Sufficiently large single crystals are essential to obtain biochemical structure data of proteins using X-ray crystallography. These data are required for drug design and disease treatment.

1. The growth of protein crystals from solution is important in separation and purification of protein products.

2. Protein aggregation takes place in several diseases, such as cataract and sickle-cell anemia.

3. A slow dissolution rate of protein crystals with a narrow size distribution has advantages in drug delivery.

4. The morphology and the quality of crystals keep protein crystallization an active field of research.

A large number of solution parameters take part in the decision for a crystal to grow.[198] Crystallization is a process involving nucleation and growth in general. Crystallization is determined to a large extent by the effective interaction between the molecules and the kinetic factors that control the nucleation and growth. The driving

force for crystallization is supersaturation, i.e., the concentration of solute in the solution above the equilibrium solubility. Lowering the temperature, increasing the ionic strength, adjusting the pH and increasing the protein concentration favor the development of supersaturation. In addition, the purity of the protein and the precipitant salt determine the kinetics of crystallization.

The SAXS method is very sensitive in detecting aggregate structures at an early stage and can therefore indicate the optimum conditions for the onset of protein crystallization.

➤ 7.10. Lipoproteins

Many dangerous diseases are associated with changes in the concentration of blood lipoproteins (LPs). Monitoring the risk of heart disease is not as simple as just measuring the cholesterol level.[199] No matter how much cholesterol is carried by the lipoprotein particles, it is the number of various lipoprotein particles that are present that contributes to heart disease. As lipoprotein particles move through the blood, they can enter the wall of an artery. As the number of lipoprotein particles increases in the blood, more particles move into the walls of arteries. Once inside the artery wall, lipoprotein particles undergo changes that lead to the formation of blockages inside the artery wall. These blockages grow over time leading to increased risk of heart attack. That is why lipoproteins are so important. It is the number of lipoprotein particles that causes heart disease.

Lipoprotein-fractions analysis[200], [201] is particularly important for people with certain risk factors, even if they have normal cholesterol values (LDL cholesterol <130 mg/dL). A lipoprotein-profile test is most important for people who suffer from heart disease, diabetes and metabolic disorders. But also people who are exposed to risk factors, such as smoking, high blood pressure, and inherited heart diseases, and those who are on cholesterol-lowering medications will appreciate a lipoprotein-profile test.

SAXS offers fast and precise measurements of LP-particles using only small amounts of sample. Its capability to measure all fractions of lipoproteins simultaneously forms it a cost effective and convenient method for lipoprotein analysis in scientific studies and medical practices.

➤ 7.11. Cancer cells

Breast cancer is a very frequent form of cancer and the leading cause of cancer deaths of women. The lifetime risk of a woman developing breast cancer is as high as 10 % to 13 % in the industrial world. Although significant efforts are being made to achieve early detection and effective treatment, 20 % of all women with breast cancer will die from the disease. Currently, diagnosis is based on the so-called triple assessment — a combination of physical examination, mammography using X-rays and/or ultrasound, and fine needle aspiration cytology or core-biopsy.

The histo-pathological assessment relies on alterations to cellular morphology and tissue architecture. Although triple assessment is effective in detecting most malignant lesions, its sub-optimal specificity means that in some cases open biopsy surgery is required to exclude malignancy. There is therefore a considerable interest in developing diagnostic tools that are specific for the presence of malignant breast tissue.

Each tissue in the breast has its own small-angle scattering (SAXS) pattern, which is directly related to the molecular structure.[202], [203] In particular, SAXS is an excellent tool for studying the supramolecular arrangement of the collagen fibrils. Collagen is the main component of the connective tissue. It is present in the tumoural masses of the breast. Formation of collagen (fibrosis) accompanies the development of breast tumours, either benign or malignant. The supramolecular arrangement of collagen fibrils degrades upon cancer invasion, and it can be revealed by SAXS. Scattering characterization of the tissues and their pathologies is therefore possible. A SAXS pattern not only carries information about the

composition of the sample, but also about the pathology of the tissues. In other words, it can help to determine whether cancer cells have invaded the tissue. Therefore, this method has the potential of being developed as a diagnostic tool.

➤ 7.12. Carbohydrates

Carbohydrates (such as starch) are biologically produced materials which are of enormous economic and industrial importance. As a naturally abundant nutrient, carbohydrates are found mainly in the seeds, fruits, tubers, roots, and stem piths of plants, notably in corn, potatoes, wheat, and rice. It varies widely in appearance according to the source but is commonly prepared as a white amorphous powder.

Carbohydrates consist of two main polysaccharides, amylose and amylopectin. Amylose is essentially linear, whereas amylopectin is highly branched. The structure of native carbohydrate is now thought to be hierarchically organized on four length scales.

1. The molecular scale (<1 nm).
2. The lamellar structure (1 nm to 10 nm).
3. The growth rings (about 100 nm).
4. The whole granule morphology (about 1000 nm).

Starch is known to adopt a semi-crystalline lamellar structure which consists of stacks of alternating crystalline and amorphous lamellae. The stacks are separated by regions of a second distinct amorphous phase. This non-lamellar amorphous region corresponds to the amorphous growth ring within the starch granule.

Many commercial products have been developed empirically over many years. The structures of these new products stretch from the molecular to the macroscopic length scale and have a substantial impact on the properties of these products. Thus, the knowledge of the structure of native starch and its changes during processing is very desirable.

The structure of starch changes in many processes such as hydrolysis, gelatinization, dissolving, melting, freezing, extrusion and many more. For example, the staling of bread is mainly the result from the transformation (i.e., retrogradation) of the starch during aging. Also many other compounds such as gluten, water soluble proteins and lipids play a important role in bread staling.

The SAXS method is very useful in investigating[204], [205] both native starch and starch products. For native starch, the SAXS method allows the study of structure and changes in the structure, lamellar repeat distance, fractional lamellar crystallinity, width of the distribution of lamellar sizes, the number of semi-crystalline repeats within each growth ring whose details characterize the starch structure. For starch products, the SAXS method is used rarely as a result from the fact that the lamellae of amyloptectin are quite collapsed or seriously destroyed. Starch is not the only component in these materials, which makes the analysis of SAXS data more complex than in native pure starch. However, for this kind of starch materials (food products) the SAXS method also allows many values to be obtained which can undoubtedly be useful in classifying the properties of these material.

➤ 7.13. Building materials

The study of the kinetics and mechanism of hydration of cement materials is of prime importance for achieving desirable mechanical properties of the hardened products and to control the reactivity of the raw mixtures (the starting material). The main phases in a typical Portland cement can be subdivided into calcium silicates as the main component and calcium aluminates as the minor component. During the hydration of an anhydrous cement, the chemical reactions are generally more complex than simple conversions of anhydrous compounds into the corresponding hydrates. Hydrated cement has a high specific surface almost entirely due to the calcium-silicate-hydrate (C-S-H) reaction product. It is closely related to many properties including strength and permeability.

It is also useful to study the nature of the C-S-H gel itself. The microstructure of cement is quite complex. It contains several reacted products, unreacted clinker grains and voids, which are responsible for the porosity. One major challenge in the measurement of the surface in hydrating cement paste arises from the involved heterogeneous microstructure and the applicable large range of length scales (from few nanometers to tens of micrometers).

When using SAXS, one of the advantages is that they can be conducted in real time during cement hydration without interfering the hydration process. This has allowed the development of a method[206], [207] to monitor the C-S-H gel structure and the surface area from the earliest stage of a few minutes. Instruments with a large q-range, a high resolution with calibrated absolute-intensity data and scattering contrast method is preferable to obtain the surface area. The advantage of a surface area measurement is significant because it is sensitive to the C-S-H gel phase which controls to some extent every property in cement-based materials. This makes the surface-area parameter useful both for the investigation of the C-S-H-gel structure and for relating the effects of processing and composition to the final properties of cement paste and concrete.

➤ 7.14. Minerals

Particles of fine-grained minerals are everywhere in terrestrial, marine and atmospheric environments. They are a major constituent of soils, they form colloidal suspensions in oceans and terrestrial water bodies, and are a major component of atmospheric aerosols. Their abundance, high surface area, reactivity and colloidal characteristics mean that they play an important role within many processes occurring in the natural environment including chemical weathering, biomineralization, transport pollutants in ground waters and the global cycle of elements. The nanoparticulate nature of these mineral phases means that their chemistry (e.g., their solubility) and phase stability are different from bulk

phases of the same composition. The implications for the natural environment require investigations on the nanoscale.

The nucleation and growth of mineral particles is often associated with hydrolysis reactions which, at first sight, are the simplest reactions of metal ions but nevertheless play a fundamental role in industrial chemistry (e.g., production of pigments, magnetic media), effluent treatment (aluminum flocs in drinking water treatment, iron flocs in the removal of radioactive and toxic metals), and environmental and atmospheric processes (e.g., aerosol formation). Particle shape/size and growth rate, in particular, are fundamental controls on the properties of the hydrolysis reaction products and SAXS is the only technique which can provide this information[208] when the particles are suspended in solution. It is however still a challenge when investigations have to be made on fast timescales associated with particle formation.

➤ 7.15. Conclusion

During the last decade, small-angle X-ray scattering has become an increasingly important tool in studying the diverse fields of material science. This process has been accelerated by the accessibility of large-scales facilities and the availability of the latest high-performance laboratory instruments along with the availability of novel and powerful data-analysis programs. Judging from the momentum that has been gained in the last decade by using SAXS, and the technique's inherent and unique capability in addressing the steadily up-coming developments in nanomaterials, suggests that, in future, SAXS will further strengthen its position in the future as a mainstream method for the analysis in a multiplicity of fields in material-science research.

8. Literature

[1] A. Guinier and G. Fournet, Small-Angle Scattering of X-rays (Wiley, New York, 1955).

[2] O. Glatter and O. Kratky (edts.), Small-Angle X-ray Scattering (Academic, London, 1982).

[3] O. Glatter and R. May, "2.6. Small-angle techniques," in A.J.C. Wilson and E. Prince (edts.), International Tables for Crystallography C (Kluwer Academic Publishers, Dordrecht, 1999).

[4] C. Giacovazzo,"The diffraction of X-rays by crystals" in C. Giacovazzo, H. L. Monaco, D. Viterbo, F. Scordari, G. Gilli, G. Zanotti and M. Catti (edts.), Fundamentals of crystallography (IUCr Texts on Crystallography No. 2.) (Oxford, 1992).

[5] J.S. Higgins and H.C. Benoît, Polymers and Neutron Scattering (Clarendon, Oxford, 1994).

[6] M. Kerker, The Scattering of Light and Other Electromagnetic Radiation (Academic, New York, 1969).

[7] Jeffries, C.M., Ilavsky, J., Martel, A. et al., Small-angle X-ray and neutron scattering. Nat Rev Methods Primers 1, 70 (2021).

[8] D.C. Creagh and J.H. Hubbell, "X-ray absorption (or attenuation) coefficients," in A.J.C. Wilson (edt.), International Tables for Crystallography, Vol. C, Sec. 4.2.4., 189-206 (Kluwer Academic, Dordrecht, 1992).

[9] J.H. Hubbell, Wm.J. Veigele, E.A. Briggs, R.T. Brown, D.T. Cromer and R.J. Howerton, "Atomic form factors, incoherent scattering functions, and photon scattering cross sections," J. Phys. Chem. Ref. Data **4**, 471-538 (1975); erratum in **6**, 615-616 (1977).

[10] J.H. Hubbell and I. Øverbø, "Relativistic atomic form factors and photon coherent scattering cross sections," J. Phys. Chem. Ref. Data 8, 69-105 (1979).

[11] D.T. Cromer and J.T. Waber, "Atomic Scattering Factors for X-Rays," in International Tables for X-Ray Crystallography, Vol. 4, Sec. 2.2., 71-147 (Kynoch Press, Birmingham, 1974).

[12] G. Goerigk, H.G. Haubold, O. Lyon and J.P. Simon, "Anomalous small-angle X-ray scattering in materials science," J. Appl. Cryst. **36**, 425-429 (2003).

[13] L.G. Parratt, "Surface studies of solids by total reflection of X-rays," Phys. Rev. **95**, 359-369 (1954).

[14] A. Gibaud and S. Hazra, "X-ray reflectivity and diffuse scattering," Current Science **78**, 1467-1477 (2000).

[15] S.K. Sinha, E.B. Sirota, S. Garoff and H.B. Stanley, "X-Ray and neutron scattering from rough surfaces," Phys. Rev. B **38**, 2297-2311 (1988).

[16] V. Holy, J. Kubena, I. Ohlidal, K. Lischka and W. Plotz, "X-Ray reflection from rough layered systems," Phys. Rev. B **47**, 15896-15903 (1993).

[17] V. Holy and T. Baumbach, "Non-specular x-ray reflection from rough multilayers," Phys. Rev. B **49**, 10668-10676 (1994).

[18] R. Lazzari, "IsGISAXS: a program for grazing-incidence small-angle X-ray scattering analysis from supported islands," J. Appl. Cryst. **35**, 406-421 (2002).

[19] M. Tolan, X-Ray Scattering from Soft-Matter Thin Films (Springer Tracts in Modern Physics, Volume 148, Berlin, 1999).

[20] J.A. Lake, “An iterative method of slit-correcting small angle X-ray data,” Acta Cryst. **23**, 191-194 (1967).

[21] G.R. Strobl, “A new method for evaluating slit-smeared small angle X-ray scattering data,” Acta Cryst. **A26**, 367-375 (1970).

[22] O. Glatter, “A new method for the evaluation of small-angle scattering data,” J. Appl. Cryst. **10**, 415-421 (1977).

[23] D. Orthaber, A. Bergmann and O. Glatter, “SAXS experiments on absolute scale with Kratky systems using water as a secondary standard,“ J. Appl. Cryst. **33**, 218-225 (2000).

[24] H. Stabinger and O. Kratky, “A new technique for the measurement of absolute intensity of X-ray small angle scattering. The moving slit method,” Makromol. Chem. **179**, 1655-1659 (1978).

[25] ISO 20804:2022, Determination of the specific surface area of porous and particulate systems by small-angle X-ray scattering (SAXS)

[26] R.N. Bracewell, The Fourier Transform and Its Applications, (McGraw-Hill, New York, 1965).

[27] I. Pilz, chapter 8, page 248 in O. Glatter and O. Kratky (edts.), Small-Angle X-ray Scattering (Academic, London, 1982).

[28] R. Mittelbach and O. Glatter, “Direct structural analysis of small-angle scattering data from polydisperse colloidal particles,” J. Appl. Cryst. **31**, 600-608 (1998).

[29] G. Fritz and A. Bergmann, “Interpretation of small-angle scattering data of inhomogeneous ellipsoids,” J. Appl. Cryst. **37**, 815-822 (2004).

[30] O. Glatter, “Computation of distance distribution functions and scattering functions of models for small angle scattering experiments,” Acta Phys. Austriaca **52**, 243-256 (1980).

[31] D. Svergun, C. Barberato, M.H.J. Koch, "CRYSOL – a program to evaluate X-ray solution scattering of biological macromolecules from atomic coordinates," J. Appl. Cryst. **28**, 768-773 (1995).

[32] P. Chacon, F. Moran, J.F. Diaz, E. Pantos, J.M. Andreu, "Low-resolution structures of proteins in solution retrieved from X-ray scattering with a genetic algorithm," Biophys. J. **74**, 2760-2775 (1998).

[33] P. Chacon, J. F. Diaz, F. Moran, and J. M. Andreu, "Reconstruction of protein form with X-ray solution scattering and a genetic algorithm," J. Mol. Biol. **299**, 1289-1302 (2000).

[34] D. Svergun "Restoring low resolution structure of biological macromole-cules from solution scattering using simulated annealing," Biophys. J. **76**, 2879-2886 (1999), erratum in **77**, 2896-2896 (1999).

[35] ISO 17867:2020, Particle size analysis - Small-angle X-ray scattering (SAXS)

[36] A. Schavkan, et al., Number concentration of Au nanoparticles in suspension: SAXS and spICPMS as traceable methods compared to laboratory methods, Nanomat. 9, 502 (2019)

[37] G. Fritz, A. Bergmann, and O. Glatter, "Evaluation of small-angle scattering data of charged particles using the generalized indirect Fourier transformation technique," J. Chem. Phys. **113**, 9733-9740 (2000).

[38] D.K. Cinader, W.R. Burghardt, "X-ray scattering studies of orientation in channel flows of a thermotropic liquid–crystalline polymer," J. Polym. Sci.,Part B: Polym.Phys. **37**, 3411 (1999).

[39] S. Steenstrup, "A simple procedure for fitting a backgound to a certain class of measured spectra," J. Appl. Cryst. **14**, 226-229 (1981).

[40] Graewert, M.A. and D.I. Svergun, Impact and progress in small and wide angle X-ray scattering (SAXS and WAXS). Curr Opin Struct Biol, 2013. **23**(5): p. 748-54.

[41] Fang, X., et al., Small-angle X-ray scattering: a bridge between RNA secondary structures and three-dimensional topological structures. Curr Opin Struct Biol, 2015. **30**: p. 147-60.

[42] Rambo, R.P. and J.A. Tainer, Bridging the solution divide: comprehensive structural analyses of dynamic RNA, DNA, and protein assemblies by small-angle X-ray scattering. Curr Opin Struct Biol, 2010. **20**(1): p. 128-37.

[43] Trewhella, J., Small-angle scattering and 3D structure interpretation. Curr Opin Struct Biol, 2016. **40**: p. 1-7.

[44] Schneidman-Duhovny, D., S.J. Kim, and A. Sali, Integrative structural modeling with small angle X-ray scattering profiles. BMC Struct Biol, 2012. **12**: p. 17.

[45] Svergun, D.I., et al., Small-Angle X-ray and Neutron Scattering from Biologiccal Macromolecules. IUCr Texts of Crystallography. Vol. 19. 2013: Oxford University Press.

[46] Jacques, D.A. and J. Trewhella, Small-angle scattering for structural biology--expanding the frontier while avoiding the pitfalls. Protein Sci, 2010. **19(**4): p. 642-57.

[47] Mertens, H.D. and D.I. Svergun, Structural characterization of proteins and complexes using small-angle X-ray solution scattering. J Struct Biol, 2010. **172**(1): p. 128-41.

[48] Koch, M.H., P. Vachette, and D.I. Svergun, Small-angle scattering: a view on the properties, structures and structural changes of biological macromolecules in solution. Q Rev Biophys, 2003. **36**(2): p. 147-227.

[49] Jeffries, C.M., et al., Preparing monodisperse macromolecular samples for successful biological small-angle X-ray and

neutron-scattering experiments. Nat Protoc, 2016. **11**(11): p. 2122-2153.

[50] Small Angle Scattering Biological Data Bank, https://www.sasbdb.org/

[51] Bergmann, A., et al., Improvement of SAXS measurements on Kratky slit systems by Göbel mirrors and imaging-plate detectors. J. Appl. Crystallogr., 2000. **33**: p. 869-875.

[52] Hura, G.L., et al., Robust, high-throughput solution structural analyses by small angle X-ray scattering (SAXS). Nat Methods, 2009. **6**(8): p. 606-12.

[53] Meisburger, S.P., et al., Domain Movements upon Activation of Phenylalanine Hydroxylase Characterized by Crystallography and Chromatography-Coupled Small-Angle X-ray Scattering. J Am Chem Soc, 2016. **138**(20): p. 6506-16.

[54] Graewert, M.A., et al., Automated pipeline for purification, biophysical and x-ray analysis of biomacromolecular solutions. Sci Rep, 2015. **5**: p. 10734.

[55] Porod, G., Die Röntgenkleinwinkelstreung von dichtgepackten kolloidalen Systemen. Kolloid Z., 1951. **124**: p. 83-114.

[56] Rambo, R.P. and J.A. Tainer, Characterizing flexible and intrinsically unstructured biological macromolecules by SAS using the Porod-Debye law. Biopolymers, 2011. **95**(8): p. 559-71.

[57] Bujacz, A., Structures of bovine, equine and leporine serum albumin. Acta Crystallogr D Biol Crystallogr, 2012. **68**(Pt 10): p. 1278-89.

[58] Kirby, N.M., et al., A low-background-intensity focusing small-angle X-ray scattering undulator beamline. Journal of Applied Crystallography, 2013. **46**: p. 1670-1680.

[59] Skou, S., R.E. Gillilan, and N. Ando, Synchrotron-based small-angle X-ray scattering of proteins in solution. Nat Protoc, 2014. **9**(7): p. 1727-39.

[60] Jacques, D.A., et al., Publication guidelines for structural modelling of small-angle scattering data from biomolecules in solution. Acta Crystallogr D Biol Crystallogr, 2012. **68**(Pt 6): p. 620-6.

[61] Svergun, D., C. Barberato, and M.H.J. Koch, CRYSOL - A program to evaluate x-ray solution scattering of biological macromolecules from atomic coordinates. J Appl Crystallogr, 1995. **28**: p. 768-773.

[62] Schneidman-Duhovny, D., et al., Accurate SAXS profile computation and its assessment by contrast variation experiments. Biophys J, 2013. **105**(4): p. 962-74.

[63] Petoukhov, M.V., et al., New developments in the ATSAS program package for small-angle scattering data analysis. J Appl Crystallogr, 2012. **45**(Pt 2): p. 342-350.

[64] Schneidman-Duhovny, D., et al., FoXS, FoXSDock and MultiFoXS: Single-state and multi-state structural modeling of proteins and their complexes based on SAXS profiles. Nucleic Acids Res, 2016. **44**(W1): p. W424-9.

[65] Tria, G., et al., Advanced ensemble modelling of flexible macromolecules using X-ray solution scattering. IUCrJ, 2015. **2**(Pt 2): p. 207-17.

[66] Schwieters, C.D. and G.M. Clore, Using small angle solution scattering data in Xplor-NIH structure calculations. Prog Nucl Magn Reson Spectrosc, 2014. **80**: p. 1-11.

[67] Burke, J.E. and S.E. Butcher, Nucleic acid structure characterization by small angle X-ray scattering (SAXS). Curr Protoc Nucleic Acid Chem, 2012. **Chapter 7**: p. Unit7 18.

[68] Woodson, S.A., Compact intermediates in RNA folding. Annu Rev Biophys, 2010. **39**: p. 61-77.

[69] Chen, H., et al., Ionic strength-dependent persistence lengths of single-stranded RNA and DNA. Proc Natl Acad Sci U S A, 2012. **109**(3): p. 799-804.

[70] Fang, X., et al., An unusual topological structure of the HIV-1 Rev response element. Cell, 2013. **155**(3): p. 594-605.

[71] Krukenberg, K.A., et al., Multiple conformations of E. coli Hsp90 in solution: insights into the conformational dynamics of Hsp90. Structure, 2008. **16**(5): p. 755-65.

[72] Krukenberg, K.A., et al., Conformational dynamics of the molecular chaperone Hsp90. Q Rev Biophys, 2011. **44**(2): p. 229-55.

[73] Krukenberg, K.A., et al., pH-dependent conformational changes in bacterial Hsp90 reveal a Grp94-like conformation at pH 6 that is highly active in suppression of citrate synthase aggregation. J Mol Biol, 2009. **390**(2): p. 278-91.

[74] Jeffries, C.M., et al., Small-angle X-ray scattering reveals the N-terminal domain organization of cardiac myosin binding protein C. J Mol Biol, 2008. **377**(4): p. 1186-99.

[75] Nadvi, N.A., et al., Clinically Linked Mutations in the Central Domains of Cardiac Myosin-Binding Protein C with Distinct Phenotypes Show Differential Structural Effects. Structure, 2016. **24**(1): p. 105-15.

[76] Jeffries, C.M., et al., Human cardiac myosin binding protein C: structural flexibility within an extended modular architecture. J Mol Biol, 2011. **414**(5): p. 735-48.

[77] Ribeiro Ede, A., Jr., et al., The structure and regulation of human muscle alpha-actinin. Cell, 2014. **159**(6): p. 1447-60.

[78] Arias-Palomo, E., et al., The bacterial DnaC helicase loader is a DnaB ring breaker. Cell, 2013. **153**(2): p. 438-48.

[79] Lorenz, O.R., et al., Modulation of the Hsp90 chaperone cycle by a stringent client protein. Mol Cell, 2014. **53**(6): p. 941-53.

[80] Michie, K.A., et al., A Highly Conserved Yet Flexible Linker Is Part of a Polymorphic Protein-Binding Domain in Myosin-Binding Protein C. Structure, 2016. **24**(11): p. 2000-2007.

[81] Taylor, J.E., et al., Calmodulin binds a highly extended HIV-1 MA protein that refolds upon its release. Biophys J, 2012. **103**(3): p. 541-9.

[82] Zhang, Y., et al., Structure, phosphorylation and U2AF65 binding of the N-terminal domain of splicing factor 1 during 3'-splice site recognition. Nucleic Acids Res, 2013. **41**(2): p. 1343-54.

[83] Lapinaite, A., et al., The structure of the box C/D enzyme reveals regulation of RNA methylation. Nature, 2013. **502**(7472): p. 519-23.

[84] Luo, D., et al., Structural insights into RNA recognition by RIG-I. Cell, 2011. **147**(2): p. 409-22.

[85] Carlon, A., et al., Improved Accuracy from Joint X-ray and NMR Refinement of a Protein-RNA Complex Structure. J Am Chem Soc, 2016. **138**(5): p. 1601-10.

[86] Hennig, J., et al., Structural basis for the assembly of the Sxl-Unr translation regulatory complex. Nature, 2014. **515**(7526): p. 287-90.

[87] Gersch, M., et al., AAA+ chaperones and acyldepsipeptides activate the ClpP protease via conformational control. Nat Commun, 2015. **6**: p. 6320.

[88] Denisov, I.G. and S.G. Sligar, Nanodiscs for structural and functional studies of membrane proteins. Nat Struct Mol Biol, 2016. **23**(6): p. 481-6.

[89] Midtgaard, S.R., M.C. Pedersen, and L. Arleth, Small-angle scattering of the cholesterol incorporation into human ApoA1-POPC discoidal particles. Biophys J, 2015. **109**(2), 308.

[90] Li, P., et al., Phase transitions in the assembly of multivalent signalling proteins. Nature, 2012. **483**(7389): p. 336-40.

[91] von Gundlach, A.R., et al., Use of small-angle X-ray scattering to resolve intracellular structure changes of Escherichia coli cells induced by antibiotic treatment. J Appl Crystallogr, 2016. **49**(Pt 6): p. 2210-2216.

[92] Williamson, T.E., et al., Analysis of self-associating proteins by singular value decomposition of solution scattering data. Biophys J, 2008. **94**(12): p. 4906-23.

[93] Kim, S.J., C. Dumont, and M. Gruebele, Simulation-based fitting of protein-protein interaction potentials to SAXS experiments. Biophys J, 2008. **94**(12): p. 4924-31.

[94] Whitten, A.E., et al., Cardiac myosin-binding protein C decorates F-actin: implications for cardiac function. Proc Natl Acad Sci U S A, 2008. **105**(47): p. 18360-5.

[95] Karagoz, G.E., et al., Hsp90-Tau complex reveals molecular basis for specificity in chaperone action. Cell, 2014. **156**(5): p. 963-74.

[96] Haslbeck, V., et al., The activity of protein phosphatase 5 towards native clients is modulated by the middle- and C-terminal domains of Hsp90. Sci Rep, 2015. **5**: p. 17058.

[97] Zierer, B.K., et al., Importance of cycle timing for the function of the molecular chaperone Hsp90. Nat Struct Mol Biol, 2016. **23**(11): p. 1020-1028.

[98] Claridge, J.K., et al., A picornaviral loop-to-loop replication complex. J Struct Biol, 2009. **166**(3): p. 251-62.

[99] Jacques, D.A., J.M. Guss, and J. Trewhella, Reliable structural interpretation of small-angle scattering data from bio-molecules in solution--the importance of quality control and a standard reporting framework. BMC Struct Biol, 2012. **12**: p. 9.

[100] Trewhella, J., et al., Report of the wwPDB Small-Angle Scattering Task Force: data requirements for biomolecular modeling and the PDB. Structure, 2013. **21**(6): p. 875-81.

[101] Sali, A., et al., Outcome of the First wwPDB Hybrid/Integrative Methods Task Force Workshop. Structure, 2015. **23**(7): p. 1156-67.

[102] Valentini, E., et al., SASBDB, a repository for biological small-angle scattering data. Nucleic Acids Res, 2015. **43**(Database issue): p. D357-63.

[103] D.-M. Smilgies, https://www.classe.cornell.edu/~dms79/gisaxs/GISAXS.html.

[104] Center for X-ray Optics - CXRO, http://henke.lbl.gov/optical_constants/.

[105] P. Busch, D. Posselt, D.-M. Smilgies, M. Rauscher and C. M. Papadakis, “The Inner Structure of Thin Films of Lamellar Poly(Styrene-b-Butadiene) Diblock Copolymers as Revealed by Grazing-Incidence Small-Angle Scattering,” Macromolecules, vol. 40, pp. 630-640, 2007.

[106] R. Lazzari, “IsGISAXS: a program for grazing-incidence small-angle X-ray scattering analysis of supported islands,” J. Appl. Cryst. , vol. 35, pp. 406-421, 2002.

[107] P. Busch, M. Rauscher, D.-M. Smilgies, D. Posselt and C. M. Papadakis, “Grazing-incidence small-angle x-ray scattering (GISAXS) as a tool for the investigation of thin nanostructured block copolymer films - The scattering cross-section in the distorted wave Born approximation,” J. Appl. Cryst. , vol. 39, pp. 433-442, 2006.

[108] B. Lee, I. Park, J. Yoon, S. Park, J. Kim, K.-W. Kim, T. Chang and M. Ree, “Structural Analysis of Block Copolymer Thin Films with Grazing Incidence Small-Angle X-ray Scattering,” Macromolecules , vol. 38, pp. 4311-4323, 2005.

[109] J. Als-Nielsen and D. McMorrow, Elements of Modern X-ray Physics, Oxford: John Wiley & Sons, 2011.

[110] H. Kiessig, “Interferenz von Röntgenstrahlen an dünnen Schichten,” Annalen der Physik, vol. 402, pp. 769-788, 1931.

[111] J. Wang, M. J. Bedzyk and M. Caffrey, “Resonance-Enhanced X-rays in Thin Film: A Structure Probe for Membranes and Surface Layers,” Science , vol. 258, pp. 775-778, 1992.

[112] Y. P. Feng, S. K. Sinha, H. W. Deckman, J. B. Hastings and D. P. Siddons, “X-Ray Flux Enhancement in Thin-Film Waveguides Using Resonant Beam Couplers,” Phys. Rev. Lett., vol. 71, pp. 537-540, 1993.

[113] A. T. Heitsch, R. N. Patel, B. W. Goodfellow, D.-M. Smilgies and B. A. Korgel, “GISAXS Characterization of Order in Hexagonal Monolayers of FePt Nanocrystals,” J. Phys. Chem. C, vol. 114, p. 14427–14432, 2010.

[114] D.-M. Smilgies, A. T. Heitsch and B. A. Korgel, “Stacking of Hexagonal Nanocrystal Layers during Langmuir–Blodgett Deposition,” J. Phys. Chem. B, vol. 116, p. 6017–6026, 2012.

[115] Z. Jiang, D. R. Lee, S. Narayanan and J. Wang, “Waveguide-enhanced grazing-incidence small-angle x-ray scattering of buried nanostructures in thin films,” Phys. Rev. B, vol. 84, p. 075440, 2011.

[116] T. H. Metzger, I. Kegel, R. Paniago, A. Lorke, J. Peisl, J. Schulze, I. Eisele, P. Schittenhelm and G. Abstreiter, “Shape, size, strain and correlations in quantum dot systems studied by grazing incidence X-ray scattering methods,” Thin Solid Films, vol. 336, pp. 1-8, 1998.

[117] M. P. Tate, V. N. Urade, J. D. Kowalski, T.-C. Wei, B. D. Hamilton, B. W. Eggiman and H. W. Hillhouse, “Simulation and Interpretation of 2D Diffraction Patterns from Self-Assembled Nanostructured Films at Arbitrary Angles of Incidence: From Grazing Incidence (Above the Critical Angle) to Transmission Perpendicular to the Substrate,” J. Phys. Chem. B, vol. 110, pp. 9882-9892, 2006.

[118] G. E. Stein, E. J. Kramer, X. Li and J. Wang, “Layering Transitions in Thin Films of Spherical-Domain Block Copolymers,” Macromolecules , vol. 40, pp. 2453-2460, 2007.

[119] R. Lazzari, http://ln-www.insp.upmc.fr/oxydes/IsGISAXS/isgisaxs.htm.

[120] D. Babonneau, “FitGISAXS: software package for modelling and analysis of GISAXS data using IGOR Pro,” J. Appl. Cryst., vol. 43, p. 929–936, 2010.

[121] Babonneau, https://www.pprime.fr/?q=fr/nanoparticules-nanostructures.

[122] S. Chourou, A. Sarje, X. S. Li, E. Chan and A. Hexemer, "HipGISAXS: A High Performance Computing Code for Simulating Grazing Incidence X-Ray Scattering Data," J. Appl. Cryst., vol. 46, pp. 1781-1795, 2013.

[123] https://github.com/HipGISAXS/HipGISAXS, https://github.com/HipGISAXS/HipGISAXS.

[124] J. Burle, C. Durniak, J. M. Fisher, M. Ganeva, G. Pospelov, W. Van Herck and J. Wuttke , "BornAgain - Software for simulating and fitting X-ray and neutron small-angle scattering at grazing incidence," http://www.bornagainproject.org, 2016.

[125] P. Müller-Buschbaum, "A Basic Introduction to Grazing Incidence Small-Angle X-Ray Scattering," in Applications of Synchrotron Light to Scattering and Diffraction in Materials (Springer Lecture Notes in Physics 776), Heidelberg, Springer, 2009, pp. 61-89.

[126] I. Park, B. Lee, J. Ryu, K. Im, J. Yoon, M. Ree and T. Chang, "Epitaxial Phase Transition of Polystyrene-b-Polyisoprene from Hexagonally Perforated Layer to Gyroid Phase in Thin Film," Macromolecules, vol. 38, pp. 10532-10536, 2005.

[127] A. Gibaud, D. Grosso, B. Smarsly, A. Baptiste, J. F. Bardeau, F. Babonneau, D. A. Doshi, Z. Chen, C. J. Brinker and C. Sanchez, "Evaporation-Controlled Self-Assembly of Silica Surfactant Mesophases," J. Phys. Chem. B, vol. 107, pp. 6114-6118, 2003.

[128] E. Crossland, M. Kamperman, M. Nedelcu, C. Ducati, U. Wiesner, G. Toombes, M. Hillmyer, S. Ludwigs, U. Steiner, D.-M. Smilgies and H. Snaith, "A bicontinuous double gyroid hybrid solar cell," Nano Lett., vol. 9, pp. 2807-2812, 2009.

[129] M. Li, K. Douki, K. Goto, X. Li, C. Coenjarts, D.-M. Smilgies and C. K. Ober, "Spatially Controlled Fabrication of

Nanoporous Block Copolymers," Chem. Mater., vol. 16, pp. 3800-3808, 2004.

[130] P. Du, M. Li, K. Douki, X. Li, C. B. W. Garcia, A. Jain, D.-M. Smilgies, L. J. Fetters, S. M. Gruner, U. Wiesner and C. K. Ober, "Ober Additive-driven Phase Selective Chemistry in Block Copolymer Thin Films: The Convergence of Top Down and Bottoms Up Processing," Adv. Mater., vol. 16, pp. 953-957, 2004.

[131] V. Pelletier, D.-M. Smilgies and P. Chaikin, unpublished.

[132] Z. Quan and J. Fang, "Superlattices with non-spherical building blocks" Nano Today, vol. 5, p. 390—411, 2010.

[133] Y. Yu, B. Goodfellow, M. Rasch, C. Bosoy, D.-M. Smilgies and B. A. Korgel, "The Role of Halides in the Ordered Structure Transitions of Heated Gold Nanocrystal Superlattices," Langmuir, vol. 31, p. 6924–6932, 2015.

[134] G. A. McConnell, A. P. Gast, J. S. Huang and S. D. Smith, "Disorder-Order Transition in Soft Sphere Polymer Micelles," Phys. Rev. Lett., vol. 71, pp. 2102-2105, 1993.

[135] J. Zhang, Z. Luo, Z. Quan, Y. Wang, A. Kumbhar, D.-M. Smilgies and J. Fang, "Low Packing Density Self-Assembled Superstructure of Octahedral Pt3Ni Nanocrystals," Nano Lett., vol. 11, p. 2912–2918, 2011.

[136] J. J. Choi, K. Bian, W. J. Baumgartner, D.-M. Smilgies and T. Hanrath, "Interface-Induced Nucleation, Orientational Alignment and Symmetry Transformations in Nanocube Superlattices," Nano Lett., vol. 12, p. 4791–4798, 2012.

[137] D. K. Smith, B. Goodfellow, D.-M. Smilgies and B. A. Korgel, "Self-Assembled Simple Hexagonal AB2 Binary Nanocrystal Superlattices: SEM, GISAXS and Substitutional Defects," J. Am. Chem. Soc., vol. 131, p. 3281–3290, 2009.

[138] S. Disch, E. Wetterskog, R. P. Hermann, G. Salazar-Alvarez, P. Busch, T. Brückel, L. Bergström and S. Kamali, "Shape Induced Symmetry in Self-Assembled Mesocrystals of Iron Oxide Nanocubes," Nano Lett., vol. 11, p. 1651–1656, 2011.

[139] C. Ocier, D.-M. Smilgies, R. Robinson and T. Hanrath, "Reconfigurable Nanorod Films: An In-Situ Study of the Relationship Between Tunable Nanorod Orientation and the Optical Properties of their Self-Assembled Thin Films," Chem. Mater., vol. 27, p. 2659–2665, 2015.

[140] A. E. Saunders, A. Ghezelbash, D.-M. Smilgies, M. B. Sigman Jr. and B. A. Korgel, "Columnar Self-Assembly of Colloidal Nanodisks," Nano Lett., vol. 6, pp. 2959-2963, 2006.

[141] B. E. Treml, B. Lukose, P. Clancy, D.-M. Smilgies and T. Hanrath, "Connecting the Particles in the Box -Controlled Fusion of Hexamer Nanocrystal Clusters within an AB6 Binary Nanocrystal Superlattice," Sci. Rep., vol. 4, p. 6731, 2014.

[142] K. Bian, J. J. Choi, A. Kaushik, P. Clancy, D.-M. Smilgies and T. Hanrath, "Shape-anisotropy driven symmetry transformations in nanocrystal superlattice polymorphs," ACS Nano, vol. 5, p. 2815–2823, 2011.

[143] M. C. Weidman, D.-M. Smilgies and W. C. Tisdale, "Kinetics of the self-assembly of nanocrystal superlattices measured by real-time in situ X-ray scattering," Nature Materials, DOI: 10.1038/NMAT4600.

[144] A. Meyer, www.gisaxs.de.

[145] A. P. Gast and W. B. Russel, "Simple Ordering in Complex Fluids," Physics Today, vol. 51, no. 12, pp. 24-30, 1998.

[146] K. Yager, www.gisaxs.com.

[147] A. Hammersley, http://www.esrf.eu/computing/scientific/FIT2D/.

[148] U. Bonse, M. Hart, An x-ray interferometer, Applied Physics Letters 6(8) (1965) 155-156.

[149] J.S. Pedersen, Instrumentation for small-angle scattering, Modern aspects of small-angle scattering, Springer1995, pp. 57-91.

[150] J. Ilavsky, F. Zhang, R.N. Andrews, I. Kuzmenko, P.R. Jemian, L.E. Levine, A.J. Allen, Development of combined microstructure and structure characterization facility for in situ and operando studies at the advanced photon source, Journal of applied crystallography 51(3) (2018) 867-882.

[151] M. Sztucki, T. Narayanan, Development of an ultra-small-angle x-ray scattering instrument for probing the microstructure and the dynamics of soft matter, Journal of Applied Crystallography 40(s1) (2007) s459-s462.

[152] B.R. Pauw, A.J. Smith, T. Snow, O. Shebanova, J.P. Sutter, J. Ilavsky, D. Hermida-Merino, G.J. Smales, N.J. Terrill, A.F. Thünemann, Extending synchrotron saxs instrument ranges through addition of a portable, inexpensive usaxs module with vertical rotation axes, Journal of Synchrotron Radiation 28(3) (2021) 824-833.

[153] O. Diat, P. Bösecke, C. Ferrero, A. Freund, J. Lambard, R. Heintzmann, Ultra-small-angle x-ray scattering with a bonse-hart camera on the high brilliance beamline at the esrf, Nuclear Instruments and Methods in Physics Research Section A: Accelerators, Spectrometers, Detectors and Associated Equipment 356(2-3) (1995) 566-572.

[154] T. Narayanan, O. Diat, P. Bösecke, Saxs and usaxs on the high brilliance beamline at the esrf, Nuclear Instruments and Methods in Physics Research Section A: Accelerators, Spectrometers, Detectors and Associated Equipment 467 (2001) 1005-1009.

[155] J. Ilavsky, A.J. Allen, G.G. Long, P. Jemian, Effective pinhole-collimated ultrasmall-angle x-ray scattering instrument for measuring anisotropic microstructures, Review of Scientific Instruments 73(3) (200 2) 1660-1662.

[156] J. Ilavsky, P.R. Jemian, A.J. Allen, F. Zhang, L.E. Levine, G.G. Long, Ultra-small-angle x-ray scattering at the advanced photon source, Journal of Applied Crystallography 42(3) (2009) 469-479.

[157] F. Zhang, G.G. Long, L.E. Levine, J. Ilavsky, P. Jemian, Quantitative characterization of the contrast mechanisms of ultra-small-angle x-ray scattering imaging, Journal of Applied Crystallography 41(2) (2008) 416-427.

[158] L.E. Levine, G.G. Long, X-ray imaging with ultra-small-angle x-ray scattering as a contrast mechanism, Journal of Applied Crystallography 37(5) (2004) 757-765.

[159] U. Bonse, M. Hart, Tailless x-ray single-crystal reflection curves obtained by multiple reflection, Applied Physics Letters 7(9) (1965) 238-240.

[160] P. Nadazdy, J. Hagara, P. Mikulik, Z. Zaprazny, D. Korytar, E. Majkova, M. Jergel, P. Siffalovic, A high-throughput assembly of beam-shaping channel-cut monochromators for laboratory high-resolution x-ray diffraction and small-angle x-ray scattering experiments, Journal of Applied Crystallography 54(3) (2021) 730-738.

[161] P. Fratzl, R. Weinkamer, Nature's hierarchical materials, Progress in materials Science 52(8) (2007) 1263-1334.

[162] Y. Liu, D. Luo, T. Wang, Hierarchical structures of bone and bioinspired bone tissue engineering, Small 12(34) (2016) 4611-4632.

[163] P. Akcora, H. Liu, S.K. Kumar, J. Moll, Y. Li, B.C. Benicewicz, L.S. Schadler, D. Acehan, A.Z. Panagiotopoulos, V. Pryamitsyn, Anisotropic self-assembly of spherical polymer-grafted nanoparticles, Nature materials 8(4) (2009) 354-359.

[164] U.G. Wegst, H. Bai, E. Saiz, A.P. Tomsia, R.O. Ritchie, Bioinspired structural materials, Nature materials 14(1) (2015) 23.

[165] D.W. Schaefer, R.S. Justice, How nano are nanocomposites?, Macromolecules 40(24) (2007) 8501-8517.

[166] W.B. Russel, W. Russel, D.A. Saville, W.R. Schowalter, Colloidal dispersions, Cambridge university press1991.

[167] R. Costi, A.E. Saunders, U. Banin, Colloidal hybrid nanostructures: A new type of functional materials, Angewandte Chemie International Edition 49(29) (2010) 4878-4897.

[168] M. Üner, Preparation, characterization and physico-chemical properties of solid lipid nanoparticles (sln) and nanostructured lipid carriers (nlc): Their benefits as colloidal drug carrier systems, Die Pharmazie - an international journal of pharmaceutical sciences 61(5) (2006) 375-386.

[169] Y. Xi, F. Zhang, Y. Ma, V.M. Prabhu, Y. Liu, Finely tunable dynamical coloration using bicontinuous micrometer-domains, Nature communications 13(1) (2022) 1-7.

[170] F. Zhang, A.J. Allen, L.E. Levine, J. Ilavsky, G.G. Long, A. Sandy, Development of ultra-small-angle x-ray scattering–x-ray photon correlation spectroscopy, Journal of Applied Crystallography 44(1) (2011) 200-212.

[171] T. Zinn, A. Homs, L. Sharpnack, G. Tinti, E. Fröjdh, P.-A. Douissard, M. Kocsis, J. Möller, Y. Chushkin, T. Narayanan, Ultra-small-angle X-ray photon correlation spectroscopy using the EIGER detector, Journal of Synchrotron Radiation 25(6) (2018) 1753-1759.

[172] V. Tohver, J.E. Smay, A. Braem, P.V. Braun, J.A. Lewis, Nanoparticle halos: A new colloid stabilization mechanism, Proceedings of the National Academy of Sciences 98(16) (2001) 8950-8954.

[173] S. Karanikas, A. Louis, Dynamic colloidal stabilization by nanoparticle halos, Physical review letters 93(24) (2004) 248303.

[174] J. Liu, E. Luijten, Stabilization of colloidal suspensions by means of highly charged nanoparticles, Physical Review Letters 93(24) (2004) 247802.

[175] F. Zhang, G.G. Long, P.R. Jemian, J. Ilavsky, V.T. Milam, J.A. Lewis, Quantitative measurement of nanoparticle halo formation around colloidal microspheres in binary mixtures, Langmuir 24(13) (2008) 6504-6508.

[176] X. Hong, G.A. Willing, Transition force measurement between two negligibly charged surfaces: A new perspective on nanoparticle halos, Langmuir 25(9) (2009) 4929-4933.

[177] F. Zhang, J. Ilavsky, Ultra-small-angle x-ray scattering of polymers, Journal of Macromolecular Science®, Part C: Polymer Reviews 50(1) (2010) 59-90.

[178] A. Guinier, Structure of age-hardened aluminium-copper alloys, Nature 142(3595) (1938) 569-570.

[179] A.A. Kulkarni, A. Goland, H. Herman, A.J. Allen, J. Ilavsky, G.G. Long, C.A. Johnson, J.A. Ruud, Microstructure–property correlations in industrial thermal barrier coatings, Journal of the American Ceramic Society 87(7) (2004) 1294-1300.

[180] A.J. Allen, J.J. Thomas, H.M. Jennings, Composition and density of nanoscale calcium–silicate–hydrate in cement, Nature materials 6(4) (2007) 311-316.

[181] Q. Jia, F. Zhang, P. Rometsch, J. Li, J. Mata, M. Weyland, L. Bourgeois, M. Sui, X. Wu, Precipitation kinetics, microstructure evolution and mechanical behavior of a developed al–mn–sc alloy fabricated by selective laser melting, Acta materialia 193 (2020) 239-251.

[182] F. Zhang, L.E. Levine, A.J. Allen, M.R. Stoudt, G. Lindwall, E.A. Lass, M.E. Williams, Y. Idell, C.E. Campbell, Effect of heat treatment on the microstructural evolution of a nickel-based superalloy additive-manufactured by laser powder bed fusion, Acta materialia 152 (2018) 200-214.

[183] S. Lee, T.B. Fischer, M.R. Stokes, R.J. Klingler, J. Ilavsky, D.K. McCarty, M.O. Wigand, A. Derkowski, R.E. Winans, Dehydration effect on the pore size, porosity, and fractal parameters of shale rocks: Ultrasmall-angle x-ray scattering study, Energy & fuels 28(11) (2014) 6772-6779.

[184] G. Gadikota, F. Zhang, A.J. Allen, Towards understanding the microstructural and structural changes in natural hierarchical materials for energy recovery: In-operando multi-scale x-ray scattering characterization of na-and ca-montmorillonite on heating to 1150 c, Fuel 196 (2017) 195-209.

[185] J.A. Hammons, S.J. Tumey, S. Aubry, R.E. Rudd, Y. Idell, N. Bertin, J. Ilavsky, I. Kuzmenko, J.R. Jeffries, H.E. Lorenzana, Processes controlling helium bubble dynamics at varying temperatures in simulated radioactive materials, Materialia (2022) 101529.

[186] F. Zhang, L.E. Levine, A.J. Allen, C.E. Campbell, A.A. Creuziger, N. Kazantseva, J. Ilavsky, In situ structural characterization of ageing kinetics in aluminum alloy 2024 across angstrom-to-micrometer length scales, Acta materialia 111 (2016) 385-398.

[187] S. Kim, G. Jin, M. Lim, “Structural dynamics of myoglobin probed by femtosecond infrared spectroscopy of the amide

band," Bull. Korean Chem. Soc. **24**, 1470-1474 (2003).

[188] M. Wulff, A. Plech, L. Eybert, R. Randler, F. Schotte, P. Anfinrud, "The realization of sub-nanosecond pump and probe experiments at the ESRF," Faraday Discussions **122**, 13-26 (2003).

[189] F. Schotte, M.H. Lim, T.A. Jackson, A.V. Smirnov, J. Soman, J.S. Olson, G.N. Phillips, M. Wulff, P.A. Anfinrud, "Watching a protein as it functions with 150-ps time-resolved X-ray crystallography," Science **300**, 1944-1947 (2003).

[190] S. Techert, F. Schotte, M. Wulff, "Picosecond X-ray diffraction probed transient structural changes in organic solids," Phys. Rev. Lett. **86**, 2030-2033 (2001).

[191] S. Bratos, F. Mirloup, R. Vuilleumier, M. Wulff, "Time-resolved X-ray diffraction: Statistical theory and its application to the photo-physics of molecular iodine," J. Chem. Phys. **116**, 10615-10625 (2002).

[192] M. Muthukumar, C.K. Ober, E.L. Thomas, "Competing interactions and levels of ordering in self-organizing polymeric materials," Science **277**, 1225-1232 (1997).

[193] J. Trewhella and J.K. Krueger, "Small-angle solution scattering reveals information on conformational dynamics in calcium-binding proteins and in their interactions with regulatory targets," Methods Mol. Biol. **173**, 137–159 (2002).

[194] G.M. Whitesides, J.P. Mathias, C.T. Seto, "Molecular self-assembly and nanochemistry: A chemical strategy for the synthesis of nanostructures," Science **254**, 1312-1319 (1991).

[195] G.M. Whitesides, B. Crzybowski, "Self-assembly at all stages," Science **295**, 2418-2421 (2002).

[196] P.J. Collings, Liquid Crystals (Adam Hilger, Bristol, 1990).

[197] K. S. W. Sing, D. H. Everett, R. A. W. Haul, L. Moscou, R. A. Pierotti, J. Rouquerol, T. Siemieniewska, Pure Appl Chem 57, 603–619 (1985).

[198] J. Narayanan and X.Y. Liu, "Protein interactions in undersaturated and supersaturated solutions: A study using light and X-ray scattering," Biophys. J. **84**, 523-532 (2003)

[199] H.B. Brewer Jr., R.E. Gregg, J.M. Hoeg, "Apolipoproteins, lipoproteins, and atherosclerosis," in E. Braunwald (edt.) Heart Disease: A Textbook of Cardiovascular Medicine, p.121-144 (WB Saunders, New York, 1989).

[200] Y.P. Nikitin, F.V. Tuzikov, N.A. Tuzikova, Y. Ragino, "Application of the small-angle X-ray scattering technique for estimation structural change of lipoprotein fractions of blood," Abstracts of 71st European Atherosclerosis Society **73**, 26-29 (1999).

[201] F.V. Tuzikov, L.E. Panin, N.A. Tuzikova, L.M. Poljakov, "Application of the small-angle X-ray scattering technique for estimating structural changes at high density lipoproteins," Membr. Cell Biol. **10**, 75-82 (1996).

[202] R.A. Lewis, K.D. Rogers, C.J. Hall, E. Towns-Andrews, S. Slawson, A. Evans, S.E. Pinder, I.O. Ellis, C.R.M. Boggis, A.P. Hufton and D.R. Dance, "Breast cancer diagnosis using scattered X-rays," J. Synchrotron Rad. **7**, 348–352 (2000).

[203] M. Fernández, J. Keyriläinen, R. Serimaa, M. Torkkeli, M-L. Karjalainen-Lindsberg, M. Tenhunen, W. Thomlinson, V. Urban and P. Suortti, "Small-angle X-ray scattering studies of human breast tissue samples," Phys. Med. Biol. **47**, 577-592 (2002).

[204] S. Pikus, "Small-angle X-ray scattering (SAXS) studies of the structure of starch and starch products," Fibres and Textiles in

Eastern Europe **13**, 82-86 (2005).

[205] P.A. Perry, T.A. Waigh, A.M. Donald, "The effect of changing solvents on the kinetics and micromechanics of starch freezing," Annual Report of the Synchrotron Radiation Department of the CLRC Daresbury Laboratory, p.110-111 (1997-1998).

[206] J.J. Thomas, H.M. Jennings and A.J. Allen, "The surface area of cement paste as measured by neutron scattering - Evidence for two C-S-H morphologies," Cement and Concrete Research **28**, 897–905 (1998).

[207] J.J. Thomas, H.M. Jennings and A.J. Allen, "The surface area of hardened cement paste as measured by various techniques," Concrete Science and Engineering **1**, 45-64 (1999).

[208] S. Shaw, L.G. Benning, N.J. Terrill, C.M.B. Henderson and J.A. Warner, "In Situ SAXS/WAXS Studies of the Precipitation, Crystallization and High Temperature Phase Transitions of Minerals," 30th Annual report of the Stanford Synchrotron Radiation Laboratory, (2003).

ISBN 18012013

This guide will give you an insight into the world of small-angle X-ray scattering.

The content spans from scattering basics, SAXS instrumentation, data analysis and interpretation to applications in the field of nanostructure analysis. Special contributions provide a thorough overview on selected disciplines such as BioSAXS, GISAXS and USAXS. The SAXS Guide is intended to help people new to the SAXS field as well as more advanced readers to get a comprehensive overview of the method. The document is not explicitly dedicated to one specific SAXS instrument or one particular application area, but aims to give an overview of the basics, instrumentation and applications.

Anton Paar

Anton Paar® GmbH
A-8054 Graz - Austria - Europe
Anton-Paar-Str. 20
Tel.: +43 (0)316 257-0
info@anton-paar.com
www.anton-paar.com